The Implications of Coarctation and Indentation of the Aorta on Blood Flow Characteristics in Pediatric Patients

by

Yuxi Jia

A thesis submitted in partial fulfillment of the requirements for the degree of

Master of Science

Department of Mechanical Engineering
University of Alberta

Abstract

Aorta coarctation is one of the most common geometrical anomalies observed in children that requires intervention in an early stage. Another equally important, but less common, anomaly of the aorta involves the indentation of the aortic arc. This study examines the blood flow characteristics in the presence of these geometrical anomalies by comparing the flow to a normal aorta model. The primary research objective of this thesis is to model the discrepancies between the blood flow characteristics of a normal and abnormal aorta, then conduct preliminary modifications to resolve key abnormal flow patterns using flow manipulators, e.g. vortex generators. Using two sets of patient-specific boundary conditions with the normal aorta model, the simulation setup was validated using experimental measurements, which only showed inaccuracies up to 5%. An abnormal aorta with a bicuspid aortic valve, aortic coarctation, and arch narrowing due to an indentation in the inferior aspect of the mid aortic arch was modeled using Direct Numerical Simulations and Fluid Structure Interaction. Moreover, the effect of boundary condition on blood flow in a normal and abnormal aorta were evaluated using a combination of Neumann and Dirichlet (patient specific) boundary conditions. Using the most optimum model setup, key regions of flow disturbance due to the geometrical anomalies of the abnormal aorta were found in the inferior aspect of the mid aortic arch and in the coarctation. These regions showed increased vorticity, large pressure drops, and high peak wall shear stress, suggesting the presence of recirculation zones. By implementing flow manipulators prior to the onset of these flow discrepancies, the optimum location of which was determined empirically, the size of the recirculation region decreased, and peak wall shear stresses declined up to 70%. The peak wall shear stress in the abnormal aorta is significantly greater than the magnitudes of wall shear stress in the normal aorta. This acts as a possible explanation for the decreased flow rate through the abnormal aorta. A decreased flow rate thereby decreases wall shear stress, and it could proactively prevent high stresses in the aorta, and lower the risk of rupture. With a decreased peak wall shear stress with the implementation of flow manipulators, the blood flow shows recovery towards normal flow rates. The coarctation also resulted in a larger

pressure drop of 19 mmHg compared to the same segment in the normal aorta. The lower flow rate leads to pressure adjustments that increases the risk of low blood pressure in the lower body of patients with such anomalies. This pressure drop is remedied slightly by the installation of flow manipulators, which help to alleviate potential problems associated with low blood pressure. Thus, the implementation of flow manipulators in the abnormal aorta did alleviate undesirable blood flow characteristics towards those of a normal aorta. This serves as a proof of concept for such an approach in the development of better treatment techniques to replace surgical reconstruction of the aorta geometry.

Preface

The results from Chapter 4 are submitted for publication and they are under-review in the Journal of Theoretical and Computational Fluid Dynamics as:

Jia, Y., Punithakumar, K., Noga, M., Hemmati, A. (2020) The implications of outlet boundary conditions on blood flow simulations in healthy aorta of pediatric subjects. *Theor. and Comp. Fluid Dynamics*, under-review.

The results from Chapters 5 and 6 are submitted for publication and they are under-review in the Journal of Applied Mechanics as:

Jia, Y., Punithakumar, K., Noga, M., Hemmati, A. (2020) Blood flow manipulation in the aorta with coarctation and arch narrowing for pediatric subjects. *J. of Applied Mechanics*, under-review.

The simulations of blood flow are completed using the resources of Compute Canada. The experiments were performed based on ethics approval granted by the Health Research Ethics Board at the University of Alberta Hospital. All of the simulations, data analysis and interpretation of results of this thesis were performed by Yuxi Jia under supervision of Dr. Arman Hemmati. Drs. Michelle Noga and Kumaradevan Punithakumar provided the experimental data and assisted in medical interpretation of the results.

Acknowledgements

I would like the thank the following people for their help with this research project: Dr. Hemmati - for providing me with guidance and feedback throughout my project. Dr. Kumar - for his help in MRI segmentation and obtaining patient boundary conditions. Dr. Noga - for her expertise on the medical aspects of the project. Chris - for his work on segmentation. And my friends and family - for all of their support.

Contents

List of Figures

List of Tables

Nomenclature

NN	Case of normal geometry with normal-patient Dirichlet boundary conditions
NNeu	Case of normal geometry with normal-patient Neumann boundary conditions
NFR	Case of normal geometry with normal-patient Dirichlet flow rate boundary conditions
AA	Case of abnormal geometry with abnormal-patient Dirichlet boundary conditions
AN	Case of abnormal geometry with normal-patient Dirichlet boundary conditions
ANeu	Case of abnormal geometry with abnormal-patient Neumann boundary conditions
AFM	Case of abnormal geometry with abnormal-patient Dirichlet boundary conditions after addition of flow manipulators
BC	Boundary Condition
MRI	Magnetic Resonance Imaging
CFD	Computational Fluid Dynamics
FSI	Fluid-Structure Interaction
WSS	Wall Shear Stress
d^*	Radial distance along the main aorta pathway measured from inlet
D	Distance Measurement - Diameter of the inlet of the corresponding model
$\varnothing^*$	Tangential distance along the aorta at a constant d^*. Normalized by D
r^*	Radius normalized by inlet radius of corresponding model
u^*	Velocity magnitude normalized by the corresponding average inlet velocity
u^+	Velocity vector normalized by the corresponding maximum inlet velocity
U_z	Phase averaged velocity vector in z-direction [cm/s]
ω	Phase averaged vorticity magnitude
P	Phase averaged pressure [mmHg]
τ_z	Phase averaged wall shear stress vector component in $z-$direction [Pa]
q^*	Flow rate normaled by inlet flow rate
$(u'u')$	Normal Reynolds stress normalized by normal stresses at d^*=0
p^*	Blood pressure normalized by inlet pressure

Chapter 1

Introduction

This work studies the blood flow in normal and abnormal aorta geometries to first establish the disturbances to the blood flow patters due to geometrical anomalies. The aorta disorders studied here are the coarctation of the descending aorta and the narrowing of the aortic arch due to an indentation. This is followed by a feasibility study on using flow manipulators to divert the blood flow in critical regions of the aorta with the aforementioned anomalies. This study uses Computational Fluid Dynamics (CFD) along with different types of boundary conditions based on patient specific data obtained experimentally through for example Magnetic Resonance Imaging (MRI).

1.1 Motivation

Cardiovascular diseases are the leading cause of death in the developed world (Benjamin *et al.*, 2019) with many disorders arising due to the poor performance of large artery reconstruction in children. Currently, the procedure for aorta reconstruction surgery is a trial and error process, where generic physical alterations are made to the aorta of the patient through surgery, and the performance is gauged to determine if further intervention is required at a later date. This procedure tends to be inconsistent, with a third of patients requiring follow up corrections due to the continuation of cardiovascular problems (Cohen *et al.*, 2019).

This thesis acts as the foundation for a larger, overarching project that aims to create patient specific solutions for children requiring aorta reconstruction surgery. Obtaining patient specific aorta geometry and blood flow data can be used in conjunction with a validated computational fluid dynamics model to accurately simulate 4D blood flow patterns in patients. With these simulation results as a guideline, major regions showing abnormal flow characteristics can be identified, and unique patient specific corrections can be suggested

to address the underlying medical concerns in patients. The patient specific solutions are expected to require less physical correction than the general surgical approaches currently used in practice. This in turn will result in a lower risk of future complications.

1.2 Research Objectives

The primary research objective of the work in this thesis is to the model the differences in blood flow characteristics between a normal and abnormal aorta, then conduct preliminary modifications to resolve key abnormal flow patterns. The work conducted for this thesis represents the initial work in the procedure to develop patient specific solutions for children requiring aorta reconstruction surgery.

CFD simulations are conducted using patient specific model templates obtained from patients at the University of Alberta Hospital as a means to create a simulation setup that is capable of accurately simulating physical blood flow in patients. A normal patient aorta model with patient specific flow data, forming unique numerical boundary conditions, is used to ensure the accuracy of the simulations. The accuracy of the simulations is determined in comparison to measured experimental velocity and pressure data from patients.

After having obtained a simulation setup of sufficient accuracy, this procedure is utilized to conduct simulations for both a normal and abnormal aorta model. The comparison of the findings from these two studies leads to an understanding of blood flow disturbance due to the geometrical anomalies. This knowledge provides an explanation, and thus allows seeking a solution, for the deviation of blood flow from normal characteristics and patterns. By characterizing key flow discrepancies between the two models, there is an opportunity to resolve abnormal flow features through modification of the aorta geometry by surgery or manipulation of the flow. In hopes of decreasing the surgical complexity of aorta corrective procedures, this work focuses on the installation of flow manipulators, rather than the modification of the aorta wall geometry.

1.3 The Aorta

The aorta is the largest artery in the body, and receives blood directly from the left ventricle of the heart. For the purposes of this thesis, the primary regions of interest are labeled in Figure 1.1. The ascending aorta is the region where the blood first enters from the heart. In this study, the aorta model is obtained from an 11 year old female patient (Subject 1) using 3D MRI. This patient received an aorta scan for detection of possible aortic disease,

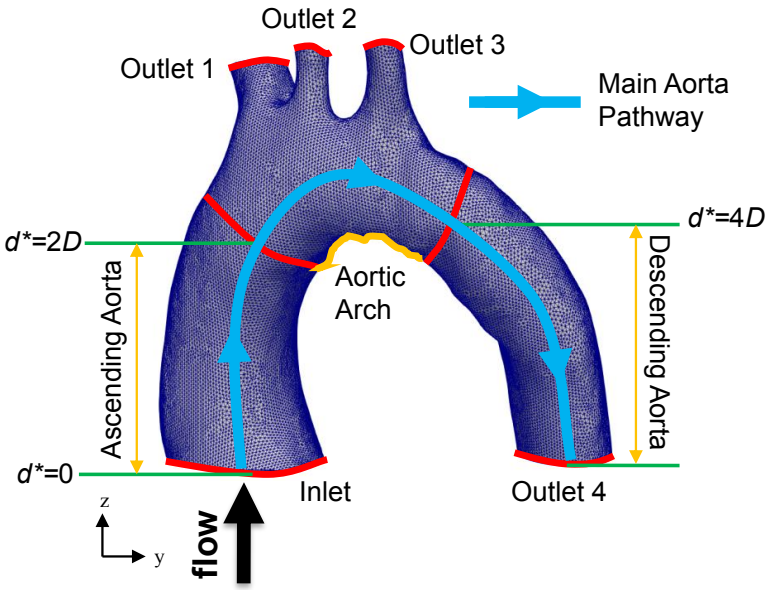

Figure 1.1: The model and mesh of the normal aorta with key regions identified and labeled. Here, d^* is the distance from the *Inlet* normalized by the *Inlet* diameter of the aorta, D.

but no disorder was diagnosed. For this aorta model, the ascending aorta was cropped at a high location, and the coronary arteries, the first branches off of the aorta, are not part of the simulation domain. The aorta models are also cropped rather high up along the descending aorta, resulting in a main aorta pathway length of approximately 6 times the *Inlet* diameter (D). *Outlet 1*, *Outlet 2*, and *Outlet 3* represent the first three pathways branching off of the aorta after the coronary arteries that lead to the left and right common carotid arteries and subclavian arteries. These arteries are responsible for delivering blood to the upper half of the body including the brain. *Outlet 4* represents the remaining blood flow that continues along the descending aorta to be distributed to the bottom half of the body.

1.4 The Abnormal Aorta

The mesh of the abnormal aorta used in these simulations can be seen in Figure 1.2. This aorta model is obtained from a 14 years old patient (Subject 2), who has received coarctation repairment treatment, and was scanned for possible recurrent coarctation. This abnormal aorta model represents the most common abnormalities found in the aorta of children, consisting of both a bicuspid aortic valve and a coarctation of the aorta. A bicuspid aortic valve can lead to many complications later in life, including aortic stenosis due to calcium buildup around the aortic valve. This stenosis would then require an increase in pressure

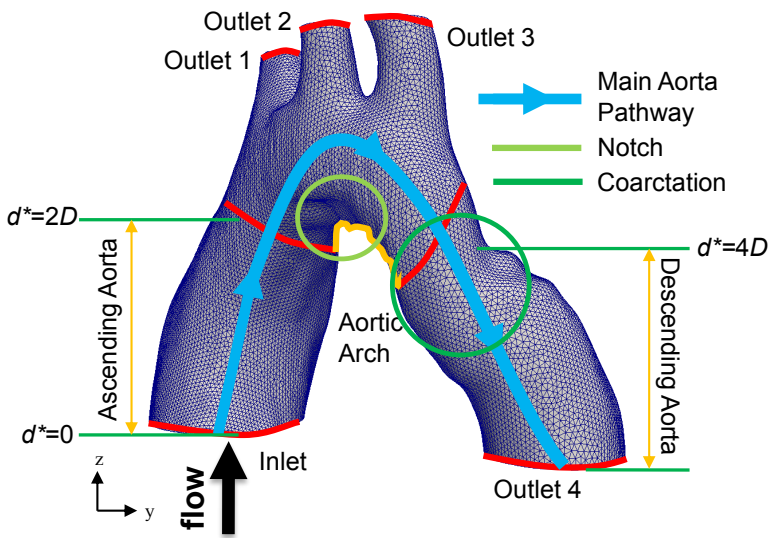

Figure 1.2: The model and mesh of the abnormal aorta with key regions identified and labeled.

to maintain healthy blood flow rate, requiring more force from the heart, increasing heart strain. Bicuspid valves are also at a greater risk of failing to close completely, which can result in allowing back-flow into the heart during the diastolic cycle. This back-flow results in regurgitation, or aortic valve insufficiency, and requires a greater flow rate during systole to mitigate the loss of blood flow during diastole. As with the aortic stenosis, the increase in flow rate would require a greater pressure output from the heart, and increases the strain on the heart to maintain healthy blood flow. The effects of the bicuspid aortic valve are not directly seen in the current study since the models do not extend to the right ventricle of the heart. However, the bicuspid aortic valve significantly influences the velocity at the *Inlet*, particularly with regards to the systolic cycle. The cardiac cycle and the definitions for systolic and diastolic cycles are discussed later in Section 1.5.

Aortic coarctation is the narrowing of the aorta - and in the unhealthy patient model considered, the narrowing occurs in the descending aorta shortly after the aortic arch. Aorta coarctation is generally a congenital disease, and it often occurs alongside other heart defects (Rao, 2005). The condition can result in mild or severe symptoms, and it may be undetected until adulthood depending on the severity of the coarctation. In cases of severe aorta coarctation, symptoms may be visible shortly after birth and include difficulty breathing and even heart failure (Fyler *et al.*, 1980). Older patients with aorta coarctation generally show milder symptoms as their aorta narrowing will be less severe. In older patients, general symptoms include elevated blood pressure in the arms and a

lower blood pressure in the legs (Gross, 1953). The narrowing of the aorta requires a higher velocity in order to maintain healthy blood flow rate to the body, and thus, it will require a higher blood pressure to be pumped from the heart (Gross, 1953). In the region of the aorta coarctation, blood flow velocity is expected to increase by continuity since the cross-sectional area of the artery is reduced and the flow rate is still maintained by the heart to ensure adequate blood circulation to the posterior regions of the body. This local increase in velocity causes a corresponding pressure drop along the coarctation (Rao, 2005), and an increase in wall shear stress, both of which are generally undesirable. Low blood pressure leads to the possibility of blood clot formation, and a consistently increased region of wall shear stress can lead to further complications including induced endothelial injury and increased permeability to lipids that favour antherogenesis (Roux *et al.*, 1992). Despite an established understanding of the common flow anomalies associated with aorta coarctation, the severity of each of these symptoms will differentiate between cases. The severity of each anomaly will have implications on optimal flow manipulator setups required for the resolution of unhealthy flow characteristics. Thus, it is essential to understand key flow characteristics on a patient-specific basis in order to optimize treatment solutions.

The abnormal aorta model used also consists of a third anomaly, known as arch narrowing. For this particular patient, arch narrowing occurs due to a slight indentation near the inferior aspect of the mid aortic arch. Due to the relatively small geometrical change, this anomaly was considered a variant of little clinical importance in early stages, rather than a disease requiring immediate surgical intervention. However, simulation results in Chapter 5 identify that the indentation results in significant deviations from normal flow characteristics despite the negligible geometrical discrepancy. This result can largely be attributed to the indentation occurring in a region of high importance in the normal aorta. Due to the large disturbances in the flow, the inferior aspect of the mid aortic arch was selected as the other primary region of interest in this study.

1.5 The Cardiac Cycle

Blood flow is pumped following a transient periodic cycle known as the cardiac cycle with a normal cardiac rate of approximately 80 beats per minute. The cardiac cycle for both the normal and abnormal aorta can be seen in Figure 1.3. Here, the systolic cycle represents the period between 0.15s and 0.4s, while the diastolic cycle represents the time between 0.4s of the current period and 0.15s of the next period. The systolic cycle of the heart occurs when the heart is stressed and compresses, pumping blood out through the right ventricle

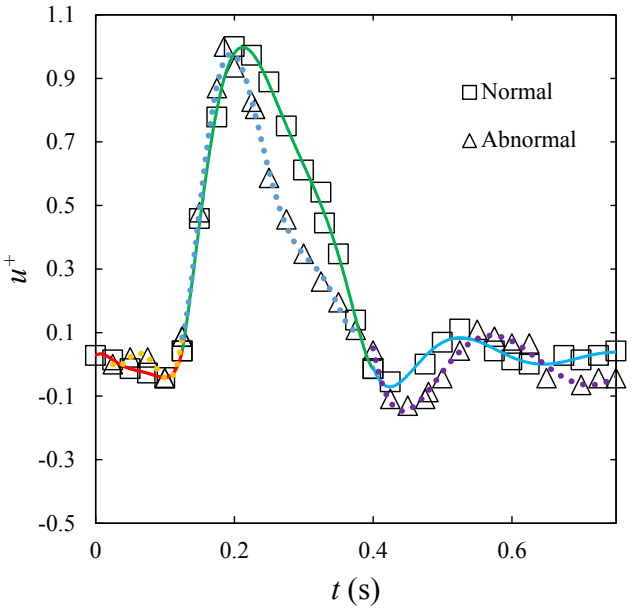

Figure 1.3: The transient blood flow waveform in the normal and abnormal aorta. Here, u^+ is the velocity normalized by the maximum inlet velocity of the corresponding aorta.

into the ascending aorta. The diastolic cycle occurs when the heart is allowed to relax and expand, and blood flow is expected to drop to negligible amounts in normal cases, and the tricuspid aorta valve is closed to prevent back-flow. Both simulations follow a cardiac cycle of 0.75s, and it is evident the systolic and diastolic phases comprise a similar proportion of the cardiac cycle for both models. It is evident that there exist some discrepancies between the cardiac waveform between the two models, the most notable of which are the narrowed systolic peak and the increased back-flow during the diastolic cycle in the abnormal aorta. These two discrepancies show that the abnormal aorta will require a higher maximum inlet velocity to maintain the blood circulation levels in the body.

1.6 Current Treatment

There are several surgical techniques to correct an aortic coarctation, including: the resection of the narrowed segment followed by end-to-end anastomosis, artoplasty using either a synthetic patch or a segmented portion of the patients subclavian flap, or bypassing the coarctation by inserting a graft formed with non-reactive material (Rao, 2005). A non-surgical procedure may also be used, with balloon angioplasty and stenting (Cheatham, 2001). During this procedure, a catheter is inserted into an artery through the groin and threaded to the heart using X-ray imaging. An uninflated balloon is inflated at the opening

of the narrowed aorta, and a stent is inserted into the coarctation to keep the segment inflated. Treatment for aorta coarctation is generally fairly effective. However, there are well-established complications with stents (Cheatham, 2001, Vitanova *et al.*, 2017), which increases the risk of clot formation and blockage, requiring new surgeries to replace them. Thus, this treatment requires lifelong monitoring to ensure future complications do not arise (Cohen *et al.*, 2019). After surgical intervention, patients still tend to have higher blood pressure than normal, and medication is regularly prescribed to patients after successful surgery or stenting to control blood pressure (Salazar *et al.*, 2002). The surgically corrected regions of the aorta tend to lose some of their elastic properties (Robinson *et al.*, 2017), and in some cases the corrected sections of the aorta may enlarge and proudce an aortic anuerysm (Cohen *et al.*, 2019). It is also possible for the coarctation to recur after treatment. In these cases, it is necessary to reperform surgery or other repair procedures to correct these complications (Cohen *et al.*, 2019). Due to the complexity of current procedures and high likelihood of disease recurrence, the usage of flow manipulators to resolve this anomaly has the potential to decrease both the complexity and risk of complications compared to current surgical methods.

The aortic arch narrowing observed in Subject 1 is regarded as a variant anatomy that may not necessarily require immediate surgical intervention at early stages. However, it will eventually require treatment if it becomes more severe, or as the disorder persists over time. Congenital aortic arch anomalies are a rare spectrum of cardiovascular diseases, and medical imaging is required to elucidate the complex geometrical anomalies. Using computed tomography or MRI imaging techniques, the effects of unique aortic arch anomalies on cardiac and non-cardiac pathologies can be interpreted (Priya *et al.*, 2018). As previous clinical solutions for similar anomalies in the aortic arch already require patient imaging and understanding of patient-specific characteristics, this anomaly leads itself perfectly to the use of patient-specific treatments, including aorta reconstruction templates or flow manipulation. The effects of the indentation on the blood flow through the aorta have not been determined experimentally. This hints at a major knowledge gap that can best be addressed numerically using a combination of MRI scan generated models and patient-specific conditions.

The treatment of the bicuspid aortic valve will not be discussed in this thesis, because it is difficult to determine a mechanism for resolving the flow abnormalities arising from this anomaly using the current simulations. The aim of this study is to alleviate the abnormal flow characteristics in the aorta with geometrical anomalies towards a healthy and normal

blood flow using alternative techniques to aorta reconstruction surgery. The secondary consequence of this aim is alleviation of the undesirable effects caused by the bicuspid valve without specific surgeries to address this disorder.

1.7 Simulation Setup

A significant proprotion of prior CFD studies involving diseases in the aorta has focused on the presence of an aorta anuerysm (Khan *et al.*, 2017, Kelly and O'Rourke, 2012, Sherifova and Holzapfel, 2019). While these studies have emphasized different physical conditions compared to the one considered in this thesis, the results and their implications remain fairly consistent. Namely, pressure, velocity, and wall shear stresses played a dominant role in quantifying the flow field. Thus, models, assumptions, and conclusions of past studies may be relevant to the methodology for obtaining accurate simulations, and interpretation of their results. The exponential improvement to computational resources in recent years allows for highly accurate and efficient simulations that were not feasible in the past.

There has been an expansive research effort exploring many variables used in blood flow simulations, which includes different fluid models, constitutive models, boundary conditions, and physical properties. In order to appreciate the previous work in the field and utilize their findings, a comprehensive literature review of previous works was necessary prior to the setup of the simulation. A detailed literature review follows in Section 2, and establishes the foundation behind selected simulation parameters.

1.8 Novelty

Unique characteristics of this study compared to previous numerical studies of blood flow are due to the combination of simulation setup parameters, incorporation of two aorta anomalies simultaneously, and using flow manipulators to resolve abnormal flow charateristics. This study combines three characteristics of previous individual numerical studies to improve simulation accuracy by: (1) accounting for the fluid-structure interaction between blood flow and aorta walls using compliable walls, (2) using patient- specific boundary conditions including a fully spatially developed velocity profile over an entire cardiac cycle, and (3) using DNS to fully capture flow field effects. This study is also unique in looking at how the combination of aorta coarctation anomaly and narrowing of the aortic arch due to an indentation affect blood flow. The utilization of flow manipulators to resolve absnormal flow characteristics is also a largely unexplored field in the study of hemodynamics, and it

is a novel medical treatment for arch narrowing and aorta coarctation.

1.9 Structure of the thesis

This thesis begins with a detailed background study in Chapter 2, which establishes the current state of blood flow simulation, and its relevant parameters in literature. It also provides a benchmark on known medical conditions and implications related to abnormal aorta geometry and its treatment.

In Chapter 3, the methodology of this study is discussed as it relates to CFD simulations. This includes description of the simulation setup, mesh generation and quality, boundary conditions, periodicity, and fluid-structure-interaction. This is followed by characterization of blood flow in a normal aorta geometry in Chapter 4. As part of this chapter, the numerical results are verified with respect to grid quality, boundary conditions and numerical setup. These results also enable validation of numerical simulations in comparison to experimental results.

Blood flow disturbances due to the geometrical anomalies are examined in Chapter 5. This includes a detailed comparison of abnormal aorta flow conditions with those of a normal aorta in terms of various flow field data, such as pressure, velocity, vorticity and stresses. Finally, the feasibility and implications of incorporating flow manipulators in different regions of the abnormal aorta is discussed in Chapter 6. This includes the changes in blood flow patterns to mitigate the disturbances and recover normal blood flow in critical regions of the aorta. The main conclusions and recommended path to expand this work are discussed in Chapter 7.

–

Chapter 2

Background

There exists a rich foundation of knowledge involving many aspects of both CFD and hemodynamics in the study of aorta (Long *et al.*, 2005, Gallo *et al.*, 2012, Rison *et al.*, 2012, Verman and Siu, 2014). The research in this thesis builds on their findings to explore and study other aspects of blood flow in the aorta with geometrical anomalies. In previous numerical and experimental studies, the desired outcomes of research dictated variations in experimental conditions. Using the past work of experts in the field as a guideline, simulation parameters must carefully be selected, such as: Newtonian or non-Newtonian fluid models, steady or pulsatile flow, turbulence models, rigid or deformable walls, and boundary conditions. The selection of each of these parameters may greatly affect the accuracy of the numerical results.

2.1 Fluid Model

A key consideration with significant effects on simulation accuracy are the fluid constitutive equations used to model blood. The non-Newtonian characterstics of blood have been shown to be negligible if the considered artery diameter is greater than 2mm (Doost *etal.*, 2016). In larger arteries, flow features dominate non-Newtonian effects on shear flow developments, and Newtonian models succeed in capturing main flow characteristics (Wu *et al.*, 2014). Wu *et al.*, 2014, considered blood as a two-component system using the mixture theory: modeling whole blood as the combination of red blood cells (considering hematocrit and influence of shear rate on viscosity, as a non-Newtonian fluid), and plasma (as a linear viscous, Newtonian fluid). Similarly to the results of Doost *et al.*, 2016, Wu *et al.*, 2014, concluded that whole blood behaves as a Newtonian fluid in large vessels with a diameter greater than 0.5 mm. In relation to these results, the aorta is the largest blood vessel in the body. Both the normal and abnormal models used here have a diameter greater than

2mm at all locations, and thus, a Newtonian fluid model should be accurate in simulating the main, coherent flow features.

Previous studies investigating hemodynamics in the coronary arteries by Johnston *et al.*, 2004 also supported using a Newtonian fluid model to simulate blood flow in the aorta. Johnston *et al.*, 2004 modeled blood using five non-Newtonian models and a Newtonian model to measure wall shear stress in a steady-state simulation. These results signify that for mid-range velocities greater than 0.2 m/s, model results are virtually indistinguishable. For the purpose of the boundary conditions used in this thesis, both the normal and abnormal models have an average inlet velocity greater than 0.2 m/s. More specifically, there is a particular interest in characterizing the blood flow during the instant of peak systole, in which velocities are expected to be above 0.2 m/s throughout the majority of the main aortic pathway. Thus, a Newtonian model is evidently appropriate in providing accurate results.

The effects of the rhelogical models are shown to be minimal on both time-averaged and unsteady wall shear stress distributions (Khan *et al.*, 2017), and the effects of the solution strategy are believed to be far more impactful. Johnston *et al.*, 2006 also confirmed similar results, in that the use of a Newtonian blood model is a reasonably good approximation in transient arterial flow when studying wall shear stress distribution. Non-Newtonian models were shown to achieve more accurate wall shear stress distributions during the middle of the diastolic cycle, when the velocities in the arteries trend towards zero (Johnston *et al.*, 2006). These effects are largely negligible because: (1) the aorta is a blood vessel larger than 2 mm, in which non-Newtonian effects should be negligble, unlike the right coronary arteries studied by Johnston *et al.*, 2006; (2) the wall shear stress during the diastolic cycle is largely irrelevant in flow characterization between the normal and abnormal aorta. The latter case is due to the very low magnitudes of stress observed during the diastolic cycle compared to the systolic cycle and peak systole. From the studies presented, it is apparent that the Newtonian fluid model presents results to reasonable accuracy for simulating flow in the aorta.

2.2 Periodicity

The periodic nature of blood has been shown to significantly impact instantaneous velocity and pressure throughout the cardiac cycle (Armstrong *et al.*, 2018). Although Benim *et al.*, 2011, showed that using pulsatile and steady-state solutions result in nearly identical time-averaged solutions, mean field results fail to portray key results that are of clinical

significance. When using a transient unsteady simulation setup, the periodic blood pressure profile can be obtained over a full cardiac cycle with high accuracy (Olufsen *et al.*, 2000). Such pressure profiles provide information that is critical in interpreting patient-specific systolic and diastolic pressure (Olufsen *et al.*, 2000), which would be unobtainable from steady-state or time-averaged results. These two results represent crucial data in the diagnosis of cardiovascular diseases, and act as an indicator for severity of high or low blood pressure. For medical applications, two instants of clinical importance are during the systolic peak and during diastasis, where blood flow rate is essentially zero (Klein *et al.*, 2017). These two instants represent the two of the extremities of the cardiac cycle, representing peak velocity and near minimum velocity. Similarly, steady state simulations fail to represent these critical periods in pressure profiles since time-averaged data provides no information for specific instants within the cardiac cycle.

In characterizing blood flow in abnormal aorta geometry, the systolic peak is the instant of interest due to the largest disturbances expected from the large magnitudes of velocity. Using the phase-averaged results would dilute the disturbances in blood flow during systole since discrepancies will be negligible during the diastolic cycle with velocity approaching zero. As such, it is important to use a transient, periodic simulation setup for boundary conditions including velocity and pressure (Armstrong *et al.*, 2018). The work of Liu *et al.*, 2011, shows the significance of the effect of pulsatile flow on the physiological functions of blood flow, and affects the transport of both low-density lipoproteins and oxygen distribution through the aorta. When considering the medically significant flow characteristics between abnormal and normal aorta, distribution of nutrients and oxygen distribution effects will be important. In such cases, steady state simulations show poor accuracy (Liu *et al.*, 2011).

Similar to the work of Armstrong *et al.*, 2018, Vignon-Clementel *et al.*, 2010, deduced that the flow rate and pressure both vary strongly with naturally varying heart rate. It was concluded that when a time-varying inflow is present, there is very little aperiodicity in the solutions for both pressure and flow rate (Vignon-Clementel *et al.*, 2010). In particular, pulsatile effects are shown to previal close to the arterial walls, and stenosed sections produced flow alterations that cannot be modeled accurately using steady state simulations, including the alterations of both size and location of flow recirculation areas throughout the cardiac cycle (Marques *et al.*, 2003). Recirculation is undersirable in the aorta, and the presence of recirculation zones can represent the deviation from healthy flow characteristics (Lizuka *et al.*, 2018). In order to accurately identify discrepancies in recirculation zones

and correct them using the installation of flow manipulators, periodic transient boundary conditions must be used.

2.3 Turbulence Modeling

The transition of blood flow to turbulence occurs naturally and is biologically relevant due to its contribution to blood clot formation. However, in standard operations, transition to turbulence is undesirable, and clot formation can lead to arterial narrowing and decreased blood flow. In hemodynamics, the aorta is at elevated risk of transitions to turbulence due to the high velocities and its large diameter relative to other arteries. Turbulence is not commonly observed in the aorta, but anomalies in the flow may lead to small eddy formations and flow perturbations that act similarly to turbulent effects (Soudah *et al.*, 2016). These transitional characteristics can be observed in normal aorta in exceptional cases, without the presence of an identifiable cardiovascular disorder (Soudah *et al.*, 2016). In contrast to Soudah *et al.*, 2016, suggesting turbulence is an uncommon phenomena, Ha *et al.*, 2018, performed a study involving 42 patients, all of which showed development of turbulence in the aorta. Keshavarz-Motamed *et al.*, 2014, showed that turbulence kinetic energy was significantly elevated in the coarctation of the aorta compared to a normal aorta, regardless of whether the coarctation was studied in isolation or within the aorta model. In contrast to a normal aorta model, where no regions showed elevated turbulence kinetic energy at any instant in the cardiac cycle, aortic coarctation produces a region of maximum turbulence inside an eccentric jet downstream of the coarctation (Keshavarz-Motamed *et al.*, 2014). Due to the elevated risk of transition to turbulence in the aorta and the presence of a coarctation further elevating turbulence kinetic energy, transitional effects may be present, and a laminar model will be insufficient to capture key flow characteristics (Lui *et al.*, 2012).

Many studies have used simple turbulence models, including Reynolds Averaged Navier-Stokes (RANS) k-ϵ and k-ω. Song *et al.*, 2003, showed that k-ω models generally outperform k-ϵ models, particularly in near-wall regions in the prism layer. Ultimately, the performance of many of these models have been poor, despite showing greater accuracy than laminar models (Zhang *et al.*, 2013). Lui *et al.*, 2012, further highlights the problems associated with classic RANS models, recommending the superior transitional RANS models that provide results closer to Direct Numerical Simulations (DNS). Lui *et al.*, 2012, highlighted that DNS succeeds in simulating locally transitional or weakly turbulent blood flow, and its associated velocity and pressure fluctuations, when the flow remains laminar during diastole. However, transitional RANS models still fail to resolve this state of blood flow. The accuracy of DNS

and its ability to show flow characteristics that cannot be analyzed even experimentally has provided great insight into the physics of turbulence (Lui *et al.*, 2012). However, the high computational cost makes DNS more viable as a tool in research than as a brute-force solver in engineering applications. Due to the complex geometry of the biological models that are used, and the relatively high velocity found in the aorta, transition to turbulence is expected. Turbulence models, however, may be unable to accurately capture small scale turbulence effects. Ultimately, due to the poor performance of simple turbulence models, and the inability of the laminar model to convey key flow characteristics in the presence of small eddy formations and turbulent flow structures, a direct approach is recommended (Lui *et al.*, 2012).

2.4 Aorta Walls

When simulating blood flow through the aorta, the Fluid Structure Interactions (FSI) beteween the walls of the aorta and blood has significant effects on the distribution of velocity, pressure and wall shear stress. The use of rigid arterial walls overestimates the wall shear stress, with differences up to 35% during peak systole (Kelly and O'Rourke, 2012). Using rigid arterial walls also effects both the distribution and magnitude of pressure and velocity throughout the simulation domain (Maivè *et al.*, 2019). Lantz *et al.*, 2011, showed that the time-averaged wall shear stress is not significantly impacted by the use of rigid walls, but discrepancies between instantaneous wall shear stresses are not negligible. Because this study aims to obtain results from medically significant instants in the cardiac cycle, the time-averaged solution is inadequate. Furthermore, rigid wall assumptions have also been shown to have shortcomings in predicting essential blood flow characteristics including wave pressure propagation (Crosetto *et al.*, 2011). As velocity, pressure, and wall shear stress are considered parameters of interest in this study, it is evident that the use of rigid arterial walls will result in a solution that is not of suitable accuracy for clinical applications. Thus, compliable aorta walls should be implemented to ensure solution accuracy.

The arterial wall is modeled as a single layer material with an elastic modulus of 840 kPa following the work of Riley *et al.*, 1992. Physically, arterial walls are composed of three layers of material with varying material properties, including elastic modulus. The initima and adventitia layers have an elastic modulus of $\approx$ 400 kPa, while the media layer has an elastic modulus of $\approx$ 1200 kPa (Gao *etal.*, 2006). Due to the relative thicknesses between the three layers, a one layer approximation with an elastic modulus of 840 kPa provides similar structural integrity when averaged across the full thickness of the arterial wall. The single

layer model fails to accurately portray the location of stress concentration, as it is largely concentrated in the media layer instead of equally throughout the thickness of the wall. Similarly, it fails to accurately predict tears and other structural failures due to extensive wall stresses (Gao *et al.*, 2006). Nevertheless, a single layer model can consistently predict similar changes in caliber and wall thickness. It also reacts consistently to small-scale fluid structure interactions compared to the three layered model (Karsaj *et al.*, 2012). Moreover, multi-layered models provide additional insight into metrics that are fundamental to arterial homeostasis and responses to injury, including axial pre-stress. However, aorta wall failure is not expected to occur in either the normal or abnormal patient (Sherifova and Holzapfel, 2019). Thus, the single layer model provides sufficient accuracy for wall shear stress results to understand key flow characteristics and identify flow disturbances that require correction.

The aorta wall for both the normal and abnormal aorta was modeled with a uniform thickness of 1.3 mm based on experimental measurements performed by Tran *et al.*, 2019. Tran *et al.*, 2019, measured the aorta wall thickness of 33 patients with an average age of 14.6 years at the ascending, proximal descending, and diaphragmatic aorta, and determined an average aorta wall radius of 1.30 ± 0.02 mm for the normal aorta. Due to the very small age difference between the abnormal patient and the average patient measured by Tran *et al.*, 2019 (14 years compared to 14.6 years), the wall thickness of 1.30 mm was applied directly. However, the age of the normal patient was lower than the patients in the experiments of Tran *et al.*, 2019 (11 years compared to 14.6 years), and the thickness of the aorta wall increases with age (Zanardo *et al.*, 2017). The work of Liu *et al.*, 2016, showed that the rate of aorta wall thickness expansion is relatively minimal after a postnatal age of 18 months (Zanardo *et al.*, 2017), up until an age in the mid 40's. These works suggested that the aorta wall thickness experiences negligible change in thickness between the ages of 11 and 14. Thus, the aorta wall thickness of 1.30 mm can be applied to the normal aorta model.

Chapter 3

Methodology

The numerical setup and details of the model, boundary conditions, grid quality, and discritization techniques are discussed in this chapter. Since experimental data are provided by collaborators from the University of Alberta Hospital, and the method in obtaining them falls outside the scope of this thesis, this chapter only focuses on CFD simulations.

3.1 Numerical Setup

The CAD model for both normal and abnormal aorta geometries were created based on patient-specific 3D MRI scans. The 3D MRI scans were obtained retroactively, and are used with the consent of the University of Alberta Research Ethics Board. The normal aorta model was obtained from an 11 year old patient (Subject 1) receiving an aorta scan for possible aortic disease, while the abnormal aorta model was obtained from a 14 year old patient (Subject 2) scanning for possible recurrent coarctation. The original 3D MRI scans consisted of the patients' entire upper chest region, and Simpleware ScanIP was used to segment the sections of the aorta that were of clinical significance. When segmenting out the necessary sections of the aorta, the ascending and descending aorta were cropped to coincide with the locations of patient-specific velocity measurements. For the three outlets at the top of the aortic arch, the model was segmented to ensure there was sufficient distance for the flow to return to normal pipe flow characteristics. It was not necessary to create a larger model for the normal or abnormal aorta, as the key regions of interest in the abnormal aorta are captured in both the normal and abnormal simulation to allow for adequate comparison. In this abnormal aorta model (Figure 1.2), the primary region of interest was the aorta coarctation at the top of the descending aorta. The secondary region of interest was the narrowing of the aortic arch leading to an indentation (a small notch) at the bottom of the aortic arch. The solid models that were obtained from the segmentation

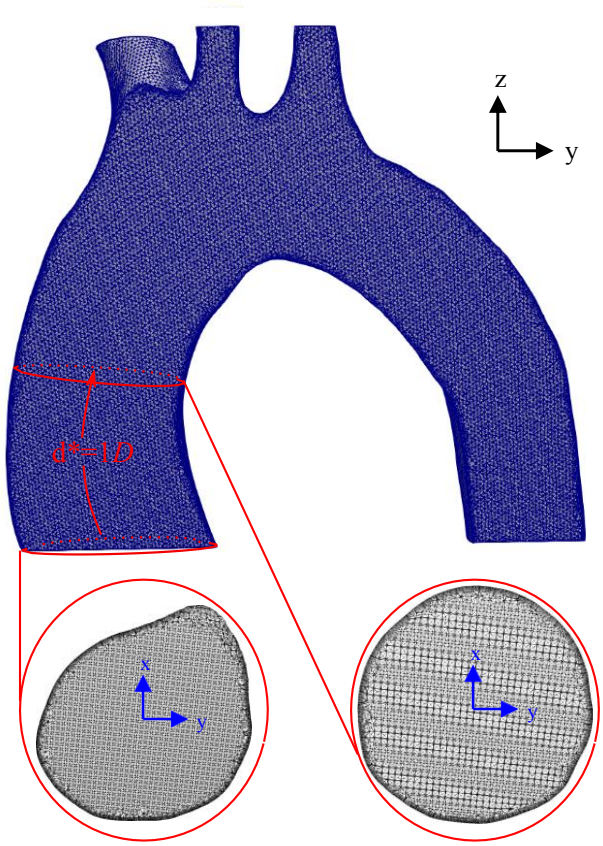

Figure 3.1: The cross-sectional mesh of the modeled normal aorta based on MRI scan results of a pediatric patient with detail view.

in Simpleware ScanIP act as the fluid medium for the simulations.

Using the models from MRI segmentation as a basis for the fluid medium, a thin wall was created to encompass each of the fluid models, representing the solid model acting as the aorta walls. After the creation of both the solid and fluid mediums, the models were imported into Ansys ICEM to generate high quality meshes for CFD analysis. A fine prism layer with 20 layers, an initial thickness of 0.01 mm and an expansion factor of 1.01 was generated around the walls of the fluid domain in order to adequately resolve the boundary layer effects (see Figure 3.1). The volume mesh was then generated using tetrahedral elements with the maximum length of 0.3 mm, resulting in a fluid mesh of 2.9×10^6 elements and 3.4×10^6 elements for the normal and abnormal aorta models, respectively. A grid independence analysis was conducted to ensure that the mesh was of adequate size and quality, details of which are discussed in Section 4.2. The solid domain for the normal and abnormal aorta was generated using 8.8×10^4 and 10.1×10^4 hexahedral elements, respectively. The solid wall had a uniform thickness of 1.3 mm, with a maximum

hexahedral length of 0.3 mm. A prism layer with 15 layers, an initial thickness of 0.03 mm, and an expansion factor of 1.1 was generated along the inside edge of the solid mesh bordering the fluid domain in order to simulate fluid-structure interactions accurately.

3.2 Simulation Parameters

The three-dimensional Navier-Stokes (Eq. 3.1) (Ershkov, 2015) and Continuity (Eq. 3.2) (Pedlosky, 1987) equations were solved directly without employing any turbulence models:

$$\rho \frac{D\vec{V}}{Dt} = -\nabla P + \rho \vec{g} + \mu \nabla^2 \vec{V} \tag{3.1}$$

$$\rho \nabla \cdot \vec{V} = 0. \tag{3.2}$$

Here, ρ is the density of blood, D represents the total derivative , $\vec{V}$ is the velocity vector with 3 components, t is time, $\vec{g}$ represents the vector of external forces, and μ is the dynamic viscosity of blood. The second order accurate central difference method (Eq. 3.3) and the backward Euler method (Eq. 3.4) were used for spatial and temporal discretization of the flow, respectively:

$$\phi_i = \frac{\phi_{i+1} - 2\phi_i + \phi_{i-1}}{dt^2} \tag{3.3}$$

$$\phi_i = \phi_{i-1} + hf(t_i, \phi_i), \tag{3.4}$$

where ϕ_i is the discretized variable at the current timestep, ϕ_{i+1} is the variable at the next timestep, ϕ_{i-1} is the variable at the previous timestep, dt is the timestep, h is the step size, and f is a function of variables ϕ_i and the current simulation time (t_i).

The velocity-pressure coupling is based on a combination of the Pressure-Implicit-with-Splitting-of-Operators (PISO) and the Semi-Implicit-Method-for-Pressure-Linked-Equations (SIMPLE) algorithms in pimpleFoam (Holzmann, 2020):

$$\nabla \cdot \left[\left(\frac{1}{A} \right)_f \nabla P \right] = \nabla \cdot \left(\frac{H}{A} \right)_f, \tag{3.5}$$

where A represents the diagonal contribution of the matrix M decomposition, such that $M[u] = Au - H$ (matrix $M[u] = -\nabla P$ is obtained by discretizing the momentum equation), subscript f denotes the face area, P represents pressure, and H is the off-diagonal contributions of the matrix M decomposition. The solution algorithm for pimpleFoam is outlined in Figure 3.2 (Versteed and Malalasekera, 2007). The convergence criteria was set on the Root-Mean-Square of the residual for 10^{-6}, which included the velocity and pressure components of the momentum equations. The normalized timestep size was $dt^* = 10^{-5}$,

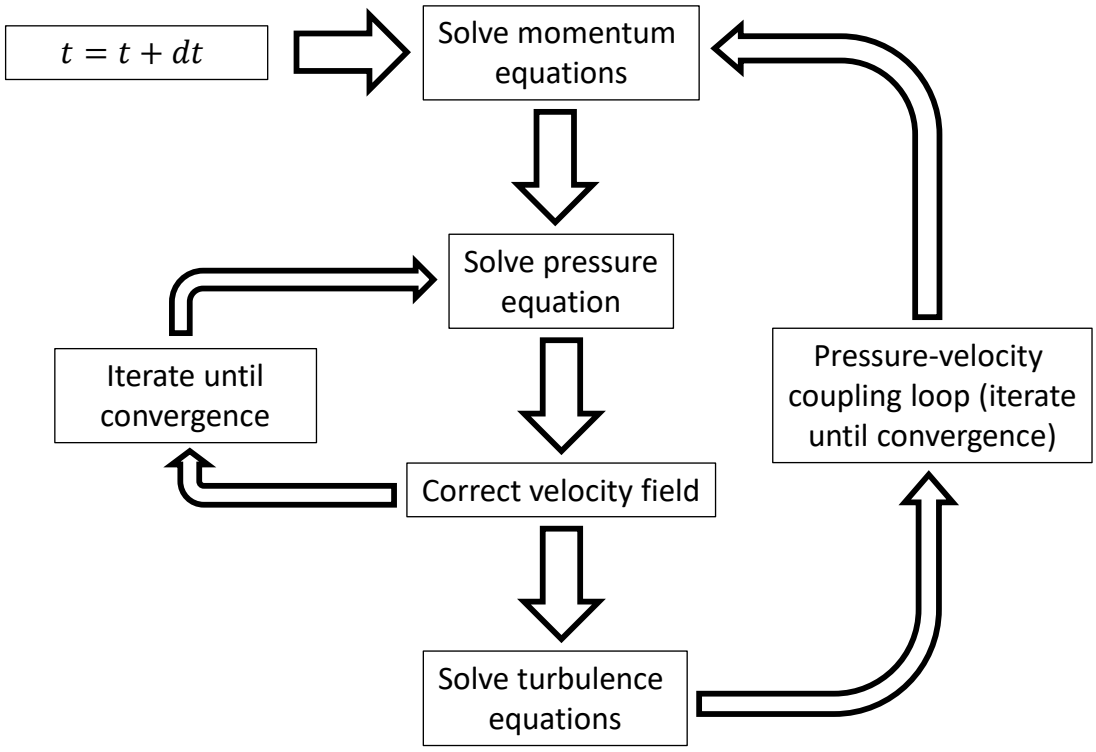

Figure 3.2: Solution algorithm for pimpleFoam function.

such that the maximum Courant–Friedrichs–Lewy number (Courant *et al.*, 1967), defined as:

$$C_{dt} = \delta x U_{in}/dt \tag{3.6}$$

remains below 0.75 in the entire aorta pathway. Here, δx is the smallest grid length and dt is the timestep.

The patient-specific velocity data was captured along the model *Inlet* using phase-contrast velocity MRI at various instants during the cardiac cycle. These velocity profiles are used as the patient-specific velocity *Inlet* condition with a spatially uniform pressure profile that varies over time following the waveform and distribution used by Alastruey *et al.*, 2016. Both the velocity and pressure *Inlet* conditions fluctuate periodically following the systolic and diastolic cycles of the heart. The Reynolds number, defined as

$$Re = \frac{DU_{in}}{\nu} \tag{3.7}$$

was approximately 1100 based on the flow rate data of Subject 1 belonging to the normal aorta. The abnormal flow Reynolds number based on the flow rate data from Subject 2

was approximately 500. Here, D is the aorta diameter, U_{in} is the inlet velocity, and ν is the kinematic viscosity of blood. The walls of the aorta were assigned the no slip boundary condition, and simulations were conducted with varying boundary conditions, details of which are discussed in Section 3.2.1.

Blood was modeled as a Newtonian fluid, with a kinematic viscosity of $3.02 \times 10^{-6}\,\mathrm{m}^2/\mathrm{s}$ and a density of $1060\,\mathrm{kg/m}^3$ (Olufsen *et al.*, 2000). As discussed earlier, blood is modeled in this study as a Newtonian fluid since its non-Newtonian characteristics, such as shear thinning properties, do not dominate macro-scale flow features in the main aorta pathway (Olufsen *et al.*, 2000). According to Olufsen *et al.*, 2000, this is mainly due to the sufficiently low shear rate of blood flow near the aorta wall boundaries. The arterial wall was modeled as a single layer material with an elastic modulus of 840 kPa (Riley *et al.*, 1992), a kinematic viscosity of $2.1\,\mathrm{Pa}\cdot\mathrm{s}$ (Boutouyrie *et al.*, 1998) and a density of $1095\,\mathrm{kg/m}^3$ (Yokawa *et al.*, 2017).

The pulsatile nature of blood was modeled based on the patient's average heart rate of 80 beats per minute, which is consistent with Vitanova *et al.*, 2017. An averaged cardiac rate of 80 beats per minute is adequate for obtaining accurate patient-specific results, and is well within the healthy range for a patient within the age of 11 to 14 (Fleming *et al.*, 2011). Moreover, small fluctuations in heart rate occur naturally due to factors such as stress and other internal and external factors. An averaged heart rate is optimal, since it can deviate significantly based on physical activity. The heart rate is set to be identical for both models, similar to a control parameter. The systolic and diastolic cycles of velocity were based on patient specific data measured over a full cardiac cycle, idealized using piece-wise polynomial functions following common practices in literature (Vita *et al.*, 2015). As stated before, the experimental measurements consisted of a fully developed flow profile taken at 28 different instants within one cardiac cycle - each instant of velocity measurement during the cardiac cycle is shown as a point in Figure 1.3. The simulations were completed over 33 cardiac cycles, which provided sufficient time to achieve statistical convergence. The initial experimental validation focused on the implications of changing simulation boundary conditions regarding the velocity and pressure profiles at 0.75s and 0.25s in the cardiac cycle. These instants are of great importance in medical applications. The former represents the time of zero inlet velocity during the middle of the diastolic cycle, while the later reflects the instant immediately following peak systole, which coincides with mid-point of the systolic cycle. To compare flow characteristics between the normal and abnormal aortas, the focus of this investigation is on flow disturbances during peak systole, which is of interest in

Table 3.1: The details of boundary conditions for cases considered in this study. Here, 'N' indicates "normal" conditions from Subject 1, 'A' indicates "abnormal" conditions from Subject 2, while 'BC' implies "Boundary Condition".

Case	**Aorta Shape**	**BC**	***Inlet***	***Outlet 1***	***Outlet 2***	***Outlet 3***	***Outlet 4***
NN	Normal	u	Dirichlet (N)	Neumann	Neumann	Neumann	Dirichlet (N)
		p	Dirichlet (N)	Dirichlet (N)	Dirichlet (N)	Dirichlet (N)	Dirichlet (N)
NNeu	Normal	u	Dirichlet (N)	Neumann	Neumann	Neumann	Neumann
		p	Dirichlet (N)	Neumann	Neumann	Neumann	Neumann
NFR	Normal	u	Dirichlet (N)	Dirichlet (N)	Dirichlet (N)	Dirichlet (N)	Dirichlet (N)
		p	Dirichlet (N)	Neumann	Neumann	Neumann	Dirichlet (N)
AA	Abnormal	u	Dirichlet (A)	Neumann	Neumann	Neumann	Dirichlet (A)
		p	Dirichlet (A)	Dirichlet (A)	Dirichlet (A)	Dirichlet (A)	Dirichlet (A)
AN	Abnormal	u	Dirichlet (N)	Neumann	Neumann	Neumann	Dirichlet (N)
		p	Dirichlet (N)	Dirichlet (N)	Dirichlet (N)	Dirichlet (N)	Dirichlet (N)
ANeu	Abnormal	u	Dirichlet (A)	Neumann	Neumann	Neumann	Neumann
		p	Dirichlet (A)	Neumann	Neumann	Neumann	Neumann
AFM	Abnormal	u	Dirichlet (N)	Neumann	Neumann	Neumann	Neumann
		p	Dirichlet (N)	Neumann	Neumann	Neumann	Neumann

medical applications. All results have been phase-averaged over 28 cardiac cycles after the simulation has reached statistical convergence.

3.2.1 Boundary Conditions

Patient-specific boundary conditions were used in order to ensure accurate, patient-specific results. Seven simulations are completed to understand the differences in blood flow characteristics between the normal and abnormal aorta models using different boundary conditions. A summary of the setups is provided in Table 3.1. At the *Inlet*, a patient specific velocity profile was imposed using a spatially distributed temporal waveform. The velocity profile was distributed spatially using velocity vector measurements mapped to coordinates from phase-contrast velocity MRI scans, and interpolated to each element in the fine mesh. The boundary conditions at the *Inlet* and *Outlet 4* are consistent inclusively within all the normal aorta simulations, and within the abnormal aorta simulations with the exception of NNeu, NFR, AN and ANeu. The boundary conditions imposed are based on patient-specific velocity boundary conditions and the Neumann zero gradient pressure boundary condition. The numerical simulations are designed such that only the boundary conditions of *Outlet 1*, *Outlet 2* and *Outlet 3* differ amongst corresponding models (excluding AN, NNeu, and AAneu).

The average normalized velocity over the *Inlet* for the normal and abnormal aorta models are shown in Figure 3.3 over five instants in the cardiac cycle. Inherently, both velocity profiles clearly depict a fully developed flow profile, which includes the slowing at

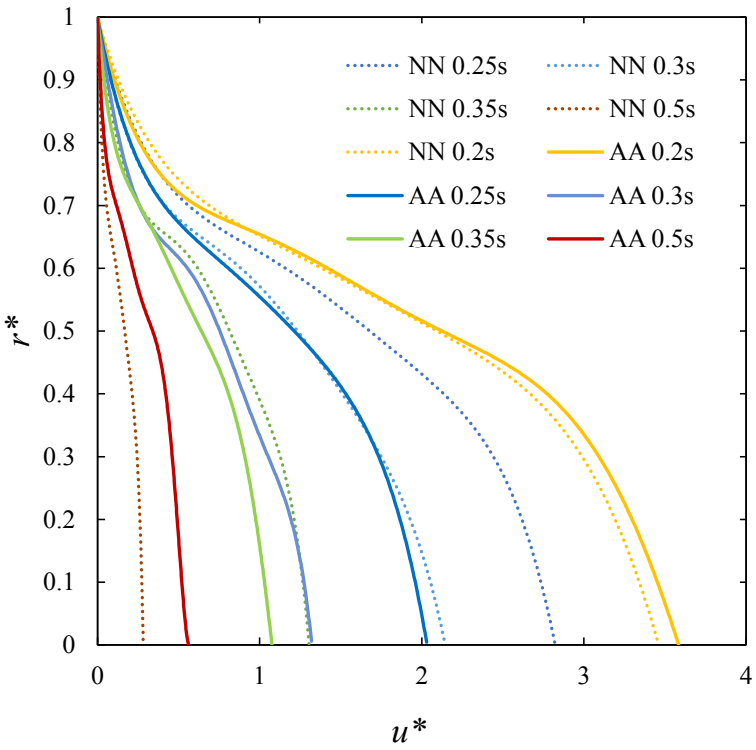

Figure 3.3: The inlet velocity profile at 5 instants for normal and abnormal models. Here, r^* is radius normalized by corresponding *Inlet* radius, and u^* is the velocity magnitude normalized by corresponding average inlet velocity of the aorta.

the wall due to the viscosity effects in the boundary layer. The temporal waveform was approximated using velocity measurements at 28 instants during the cardiac cycle. These constitute the patient-specific boundary conditions for velocity imposed in the simulations. Three piecewise polynomial functions were fit to the 28 instants as per common practice (Vita *et al.*, 2015), with polynomial one fitting the measurements prior to systole, the second polynomial denoting the systolic cycle, and the third polynomial fit to the period the remainder of the diastolic cycle (see Figure 1.3 for details). A velocity boundary condition is imposed at *Outlet 4* using a waveform over time, with a spatially developed flow field based on patient-specific velocity data similar to the *Inlet*. The walls of the fluid model are given a no-slip boundary condition for velocity. The other condition includes patient-obtained spatially uniform pressure profiles that vary over time based on the waveform and distribution that has been validated previously by Alastruey *et al.*, 2016. The initial velocity in the fluid domain was uniform at 0, and the initial pressure was uniform at 101 mmHg.

We considered the importance of the outlet boundary conditions by comparing simulations using different combinations of Dirichlet and Neumann boundary conditions for *Outlet*

1, *Outlet 2* and *Outlet 3*. First, we used the Dirichlet pressure condition and the Neumann velocity condition on the three outlet boundaries. The pressure was applied uniformly across each of the three outlets using an idealized waveform following the common practice in literature (Kim *et al.*, 2009). The pressure magnitudes were based on patient-specific systolic and diastolic pressure using standard pressure distributions in the aorta (Kim *et al.*, 2009). This simulation is denoted by "NN" to represent normal aorta simulations based on normal boundary conditions obtained from Subject 1. The second simulation also used the normal aorta model using the Neumann boundary condition for both velocity and pressure at *Outlet 1*, *Outlet 2* and *Outlet 3*. This simulation is denoted by "NNeu" to represent normal aorta simulations using Neumann boundary conditions.

Similar to the normal aorta simulations, we investigated three different boundary conditions for the abnormal aorta. The first abnormal aorta simulation used the Dirichlet boundary condition at *Outlet 1*, *Outlet 2* and *Outlet 3* based on the magnitudes obtained experimentally from Subject 2 with the abnormal aorta. This simulation is denoted as "AA" to represent abnormal aorta simulations using abnormal boundary conditions. The abnormal aorta model was then used in conjunction with the boundary conditions of the normal aorta from Subject 1 for the *Inlet* and all the outlets to better identify the blood flow variations due to the cardiovascular disorders. The boundary conditions imposed in this simulation were adapted such that they ensure an identical flow rate compared to the normal aorta at the *Inlet* and *Outlet 4*. Indeed, the velocity magnitudes varied compared to the normal aorta due to differences in diameters of the two aorta models. The pressure applied at the boundaries were identical to the ones used in NN. This simulation is denoted as "AN" to represent abnormal aorta simulations using normal boundary conditions from Subject 1. The final simulation used the abnormal aorta model with the Neumann boundary condition at *Outlet 1*, *Outlet 2* and *Outlet 3*. This simulation is denoted by "ANeu".

The pressure outlet boundary condition was assigned a quasi-patient-specific spatially-uniform pressure of varying magnitudes at each outlet following a transient waveform (Vignon-Clementel *et al.*, 2006). In NN and AN, the peak boundary pressure at the *Inlet* was 112 mmHg, and it changed for each outlet to 121 mmHg, 123 mmHg, 116 mmHg, and 95 mmHg, for outlets 1 through 4, respectively, based on experimentally obtained patient data. In AA and AFM, these values were modified to 122 mmHg, 130 mmHg, 132 mmHg, 128 mmHg, and 79 mmHg at the *Inlet*, *Outlet 1*, *Outlet 2*, *Outlet 3*, and *Outlet 4*, respectively. Note that the pressure variations followed a waveform in time, and the outlets corresponded to the outlets as labeled in Figures 1.1 and 1.2. The same peak patient-specific pressure

data was used for the *Inlet* in NFR, but this simulation used outlet boundary conditions specified by flow rate rather than the pressure. The flow rate boundary condition was assigned at each outlet based on patient-specific relative flow rate magnitudes. The average flow rate at *Outlet 4* was the largest at 3.39 L/min, which decreases to 0.95 L/min, 0.25 L/min, and 0.31 L/min in *Outlet 1*, *Outlet 2*, and *Outlet 3*, respectively. The flow rate boundary condition imposed at these outlets follow an identical periodic waveform to the velocity at the outlet (Figure 1.3).

We focus on NN and AA simulations for characterizing the change in blood flow due to the the indentation and coarcation anomalies of the aorta. This is because these two simulations are the only ones that most accurately denote patient-specific physical flow conditions. The results of other simulations (AN, NNeu and ANeu) are only discussed if they provide meaningful insight into the physical conditions or clarify an observation at all regions of interest.

3.2.2 Fluid-Structure Interaction

The FSI algorithm is implemented using the fsiFoam solver in OpenFOAM (within FOAM-Ext-4.0). Model geometry are created for both the solid and fluid components, and their computations are linked using a serial coupling function. The FSI algorithm is outlined in the flow chart of Figure 3.4. The pressure, viscous forces, displacement increment, and velocity are the data transferred between the solid and fluid components of the solution to calculate the relevant residual. The iterations continue until the residual has met the specified tolerance, after which the simulation proceeds to the next time interval and the FSI solution algorithm repeats itself. The fsiFoam solver has been utilized in previous CFD studies and it is verified to provide accurate results that are consistent with experimental measurements (Al-Manthari and Maimouna, 2018).

The aorta wall simulation is solved using linear elastic constitutive equations (Nicosia *et al.*, 2002), with the density of the aorta wall set to be $1.095\,\mathrm{g/cm^3}$, following experimental measurements from X-ray phase-contrast tomography (Yokawa *et al.*, 2017). An aorta wall viscosity of $2.1\,\mathrm{Pa\cdot s}$ is used (Boutouyrie *et al.*, 1998). The Young's modulus of elasticity for the aorta wall is assumed to be 840 kPa - using the average value of 3,321 human arteries measured experimentally by Riley *et al.*, 1992, using noninvasive ultrasound techniques. Although the model used was selected from an 11 year old pediatric patient, studies have revealed that the Young's modulus from adult measurements may be used for pediatric patients since it remains consistent regardless of age in healthy patients (Isnard *et al.*,

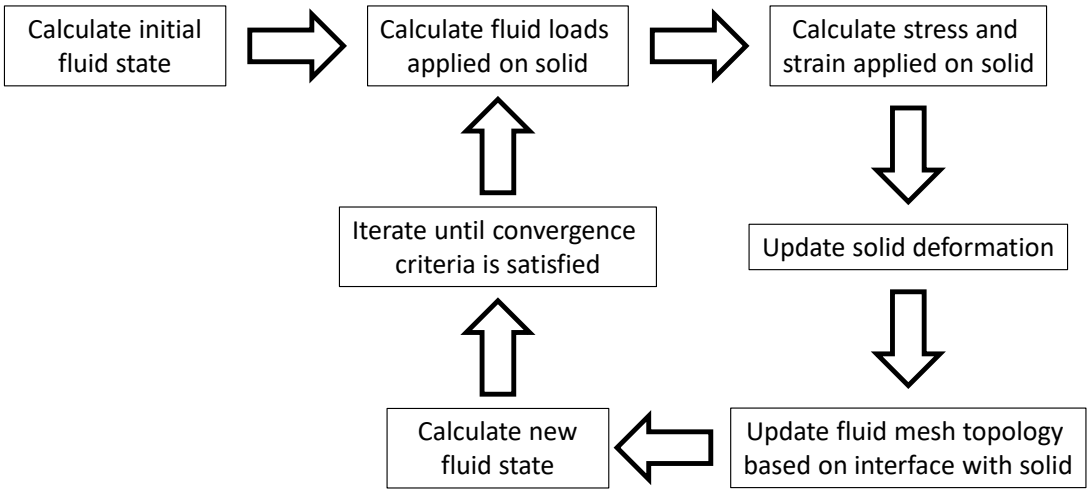

Figure 3.4: The iterative solution algorithm of fsiFoam solver for one timestep.

1989). The initial state of the wall shear stress was a fully relaxed state exhibiting zero shear stress at all locations, which is consistent with the fairly low stresses of the aorta walls at low flow velocity in the mid-point of the diastolic cycle, when the simulations begin. The simulation proceed for 33 cardiac cycles, allowing sufficient time to reach convergence towards a physical solution.

The total Lagrangian stress model is used for the solid domain, with a convergence tolerance of 1×10^{-7} and a relative convergence tolerance of 1×10^{-3}. The mesh for the solid domain can deform. A linear interpolation scheme was used for μ, and density was kept constant. The displacement in the solid domain is linked to the imposed traction (tractionDisplacement in openFoam), representing the combination of normal and shear stress components. The initial pressure, traction, and dispacement of the walls are set to zero to represent the low pressure and stress condition present during diastole at the start of the simulation. By running the simulation for 33 full cardiac cycles, the displacements, pressure and traction are all given sufficient time to converge to physical values. In this simulation, there are no solid patches with fixed displacement, as all sections of the aorta wall are expected to deform during the cardiac cycle.

A more comprehensive overview of the fsiFoam solution algorithm for one timestep is outlined in Figure 3.4 (Li, 2017). The fsiFoam solver utilizes the fluid solver (fluidSolvers), solid solver (solidSolvers) and FSI (fluidSolidInterface) classes within the extend-foam-4.0 $fluidSolidInteraction$ library. Within the FSI class, openFoam function dynamicFvMesh.H is enabled to allow for the use of a dynamic mesh. The constructed object "fsi" in the FSI

library is the basis for the majority of the functional code, and it is used in discribing the intialization, calculation, and convergence of the problem. The fsiFoam code begins initialization by calling member functions of the FSI library. After initialization, the solver proceeds to the first timestep. A prediction is made for initial forces for both the fluid and solid components. Then, the fluid state is solved using the fluid solver. Using the updated forces imposed on the solid, the stress, strain and displacement of the solid can be updated. The difference between the fluid-interface and solid-interface mesh displacement is then calculated. This parameter represents the convergence residual, and it is set to keep the fluid and solid mesh interfaces coupled. After calculating the residual, the displacement of the solid and fluid domains are updated. If the residual does not satisfy the convegence criteria, the iterative process repeats, and the fluid state is solved for again. This process is repeated until the residual falls below the specified convergence critera. Once the residual is sufficiently low, the simulation proceeds to the next timestep following the update of solid and fluid meshes.

Chapter 4

Normal Aorta Geometry [1]

4.1 Introduction

This chapter characterizes the blood flow in a normal aorta geometry based on patient-specific boundary conditions obtained from Subject 1. Moreover, this study identifies and characterizes the differences in simulation results based on different types of outlet boundary conditions. Thus, we compare the implications of separately specifying the velocity or pressure at the outlet. Since patient-specific parameters are a critical component of this study, it is important to recognize discrepancies between the use of two commonly employed outlet boundary conditions in situations where only one of the measurements are available. The results from this chapter are then used to identify flow disturbances due to aorta geometrical anomalies. This chapter begins with a mesh verification of the simulations in Section 4.2, which is followed by discussions on implications of outlet boundary conditions in Section 4.3 along with validation in comparison to experiments. The characterization of the normal blood flow is discussed in Section 4.4. A summary of the main conclusions are presented in Section 4.5.

4.2 Simulation Verification

Grid quality and independence is one of the critical aspects of numerical analysis. Thus, a grid independence study was conducted to ensure that the selected spatial grid was adequate, and that results were converged within the asymptotic range. Three grids were evaluated for this analysis based on the normal aorta model and the boundary conditions for simulation NN. Details on the grid elements can be seen in Table 4.1. The measurements

[1] The results in this chapter are part of a publication currently under review in the Journal of Theoretical and Computational Fluid Dynamics: Jia, Y., Punithakumar, K., Noga, M., Hemmati, A. (2020) The implications of outlet boundary conditions on blood flow simulations in healthy aorta of pediatric subjects. *Theor. and Comp. Fluid Dynamics.*

Table 4.1: The variation of grid resolution ($\Delta x/\eta$) and grid-wall distant (y^+) for the three grids along the blood flow path in the aorta, where d^* is the distance from the aorta *Inlet*.

Cases	Num. Elements	$d^* =$	1	2	4
Coarse Grid	9.0×10^5	$\Delta x/\eta =$	3.4	2.7	3.9
Medium Grid	2.9×10^6	$\Delta x/\eta =$	2.3	1.7	2.7
Fine Grid	9.8×10^6	$\Delta x/\eta =$	1.5	1.1	1.9
Coarse Grid	9.0×10^5	$y^+ =$	2.9	3.6	2.1
Medium Grid	2.9×10^6	$y^+ =$	1.9	2.4	1.4
Fine Grid	9.8×10^6	$y^+ =$	1.4	1.7	0.9

of flow rate at various regions along the main aorta pathway for the three grids are shown in Figures 4.1 and 4.3, respectively. The flow rate results are more consistent amongst the 3 grids compared to the pressure results. However, both parameters differed by less than 5% between the finest and coarsest mesh. Thus, both the flow rate and pressure measurements are expected to fall along the asymptotic range, and the medium mesh will be sufficient for capturing the integral and large-scale flow features.

The Kolmogorov length scale (η) is commonly used to determine the applicability of DNS studies. The ratio of grid element length to Kolmogorov length scale ($\Delta x/\eta$) at different locations in the flow along the aorta pathway are presented in Table 4.1. These ratios remain below 5 at all the critical flow regions, which indicates that the grid is sufficient to solve the unsteady flow features using DNS based on the recommendations of Moin and Mahesh, 1998, that $\Delta x/\eta \leq 10$. The first grid wall distance is also shown in Table 4.1 in terms of y^+, which has a maximum value of 3.6 at $d^* = 2$. Since the maximum y^+ remains below 5, this further verifies that the grid quality is sufficient for capturing the wall boundary layer.

The impact of mesh refinement on simulation results can be further quantified by analyzing the flow rate at different stages of the aorta more closely in Figure. 4.1. The normalized flow rate remained consistent at a magnitude of 1.0 from the *Inlet* of the aorta to a downstream distance of $2.0D$. At this distance, the blood is still in the ascending aorta and it has not yet approached the first outlet, and all flow remains in the main aorta pathway. At a distance of $d^* > 2D$, the flow nears *Outlet 1* and a portion of the flow begins to separate. At $d^* = 2.4D$, a portion of the flow has passed towards *Outlet 1*, and the flow rate through the main aorta pathway has decreased. The flow rate through the main aorta pathway continues to decrease until a distance of $d^* = 3.6D$ as the blood flow further diverges into the three outlets of the aortic arch. At $d^* \geq 3.8D$, the flow rate again becomes constant at approximately $q^* = 0.75$ since blood has passed the aortic arch, and there are no further outlets prior to *Outlet 4* at the end of the descending aorta. In the aortic arch, the

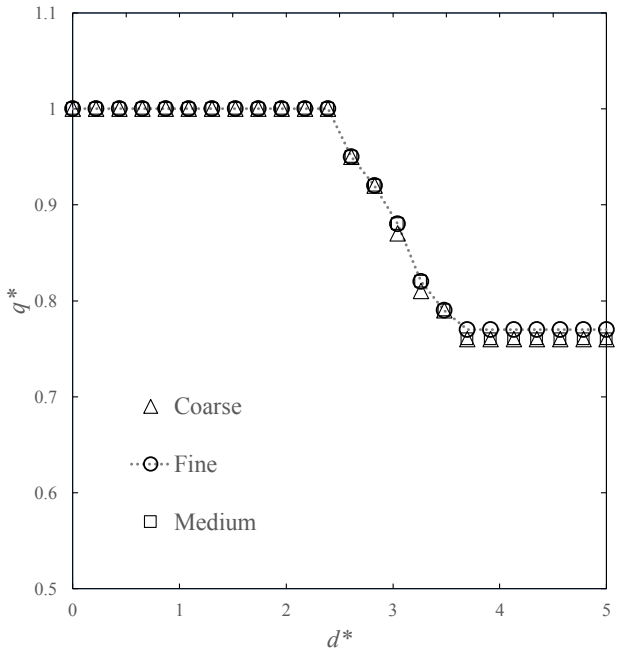

Figure 4.1: The blood flow rate at 0.25s for three spatial grids using simulation NN. Here, q^* is flow rate normalized by the *Inlet* flow rate.

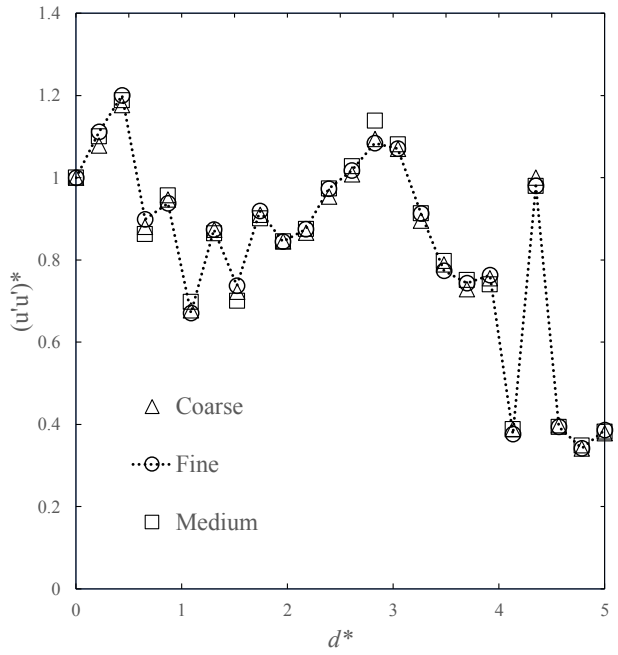

Figure 4.2: The normal Reynolds stress at 0.25s for three spatial grids using simulation NN. Here, $u'u'$ is the normal Reynolds stress , which is normalized by the normal stresses at $d^* = 0$.

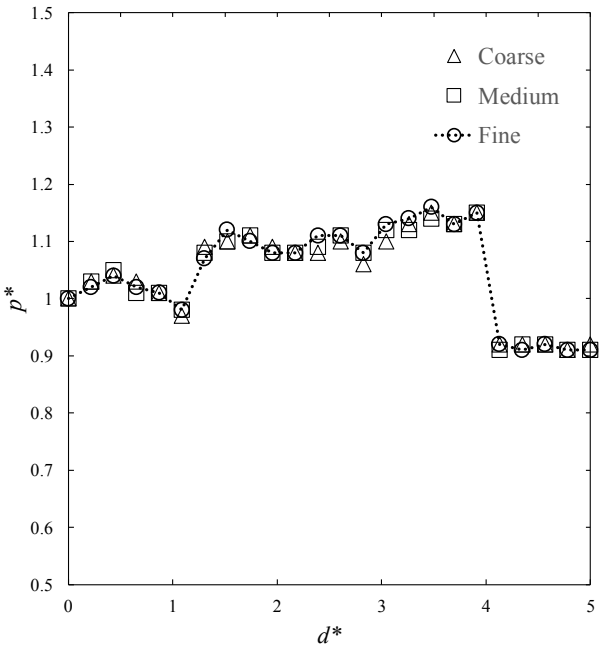

Figure 4.3: The blood pressure at 0.25s for three spatial grids using simulation NN. Here, p^* is the blood pressure normalized by the *Inlet* pressure.

decrease in flow rate is approximately linear, at a similar rate for all three meshes. The coarse mesh shows a decreased flow rate near the end of the aortic arch, but it also shows a higher flow rate in the descending aorta compared to the medium mesh. In the descending aorta, the medium mesh depicts a lower flow rate than the fine and coarse meshes, but the discrepancy is within a reasonable range of 1%. Thus, the simulations have reached grid independence with the medium mesh, and results compare closely with previous studies including Kim *et al.*, 2009. The grid-independence in unsteady flow behavior (turbulence) is also observed by comparing the normal Reynolds stresses ($\overline{u'u'}$) along the main aorta pathway in Figure 4.2. The Reynolds stress also collapse between the three meshes with a maximum discrepancy of less than 5%.

Similarly, the effects of grid refinement on pressure variations can be further quantified by analyzing the results in Figure 4.3. The pressure fluctuations in the main aorta pathway are more pronounced than the fluctuations in flow rate. There are also more discrepancies between the meshes in capturing the pressure fluctuations. However, the pressure magnitudes remain consistent between meshes, with the maximum discrepancy between the coarse mesh and the fine mesh less than 4%. The pressure at the start of the ascending aorta near the *Inlet* fluctuates around $C_p = 1.0$, but the pressure increases significantly at

a distance of $d^* = 1D$. Unlike the flow rate, the pressure in the main aorta pathway is affected by the first three outlets prior to entering the aortic arch. At $1.0D \geq d^* \geq 3.0D$, C_p increases to 1.1 with small fluctuations in magnitude. After passing the first 3 outlets, the pressure in the aortic arch increases to $C_p = 1.16$, which is held fairly consistent until a distance of $d^* = 4D$. This coincides with the end of the aortic arch. In the descending aorta, pressure decreases rapidly to approximately $C_p = 0.9$, where it continues to decrease slowly until blood flow reaches *Outlet 4*. The pressure obtained by the Medium Grid at various regions in the aorta agrees with previous pressure measurements obtained from the experiments of Kim *et al.*, 2009. This provides further evidence that the Medium Grid is sufficient to provide accurate unsteady results.

4.3 Implications of Outlet Boundary Conditions

Outlet boundary conditions are crucial in accurately modeling blood flow in the aorta. The velocity contours shown in Figure. 4.4 highlight the regions of interest in the aorta that are relevant in medical applications and diagnosis. These regions are located prior to each of the 4 outlets (B, C, D and E in Figure 4.4) and prior to the branching of *Outlet 1* from the main aorta pathway (outlet A in Figure 4.4). The velocities found at regions B, C, D, and E show similar trends for both the NN and NFR simulations at $t = 0.75$s and 0.25s. The velocities in region A exhibit slight discrepancies between the two simulations, where the flow rate boundary condition (NFR) resulted in an overestimation of velocity near the bottom sections of the cross-section during the diastole cycle. These same areas in Region A also underestimate the velocities during systole in NFR compared to NN. In regions C and D, the velocity throughout the entire slice is relatively uniform, while in region B, the velocity is largest near the top of the cross-section and it linearly decreases towards the bottom of the cross-section. In region E, the velocity decreases significantly as it approaches the side proximal to the aortic arch. Out of the regions of interest, the highest velocity is observed in region E. Region A, and the distal parts of region E, show some of the highest velocities in the aorta outside of the aortic arch. The highest velocity during diastole occurs in region E, while the highest velocity during systole occurs in region A. These results coincide with the velocity obtained by Soudah *et al.*, 2016. The cross-sectional velocity results in region E show a discrepancy between NN and NFR boundary conditions that we could best visualize using the velocity contours (our efforts showed that using streamline or the velocity profile data did not correctly show these differences). Despite having a higher overall flow rate, region E in NFR has a larger region of low velocity compared to NN, which is compensated

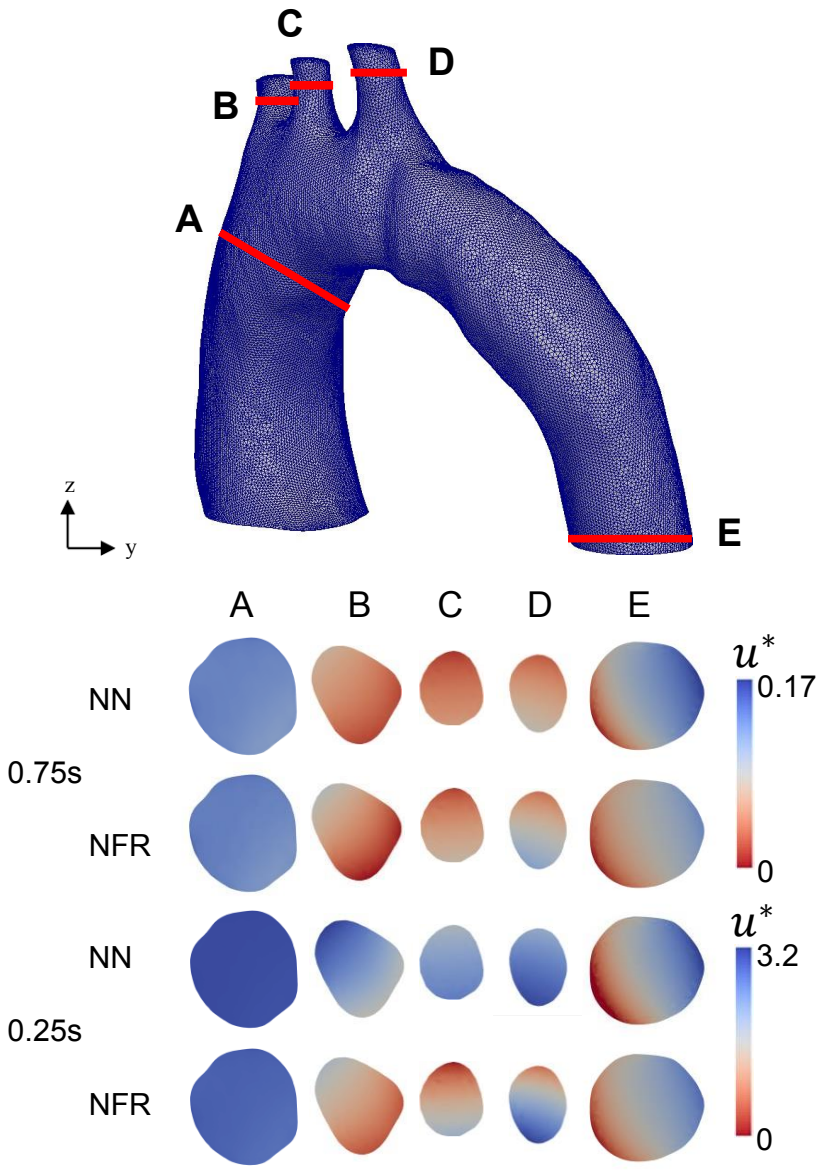

Figure 4.4: The cross-sectional contours of phase-averaged streamwise velocity of blood at systole and diastole in the normal aorta.

by a higher velocity in the remaining parts of the aorta. The areas of low and high velocity remain consistent between the two simulations, with the region proximal to the aortic arch showing very low velocities (approaching zero). Although there is a relatively good agreement between NN and NFR at $t = 0.75$s for regions B, C and D, they start showing discrepancies at $t = 0.25$s. The results in NN systematically overestimated the blood flow velocity compared to NFR, where we used patient-specific flow rate boundary conditions.

The velocity streamlines in Figure 4.5 are obtained by tracing the streamlines through

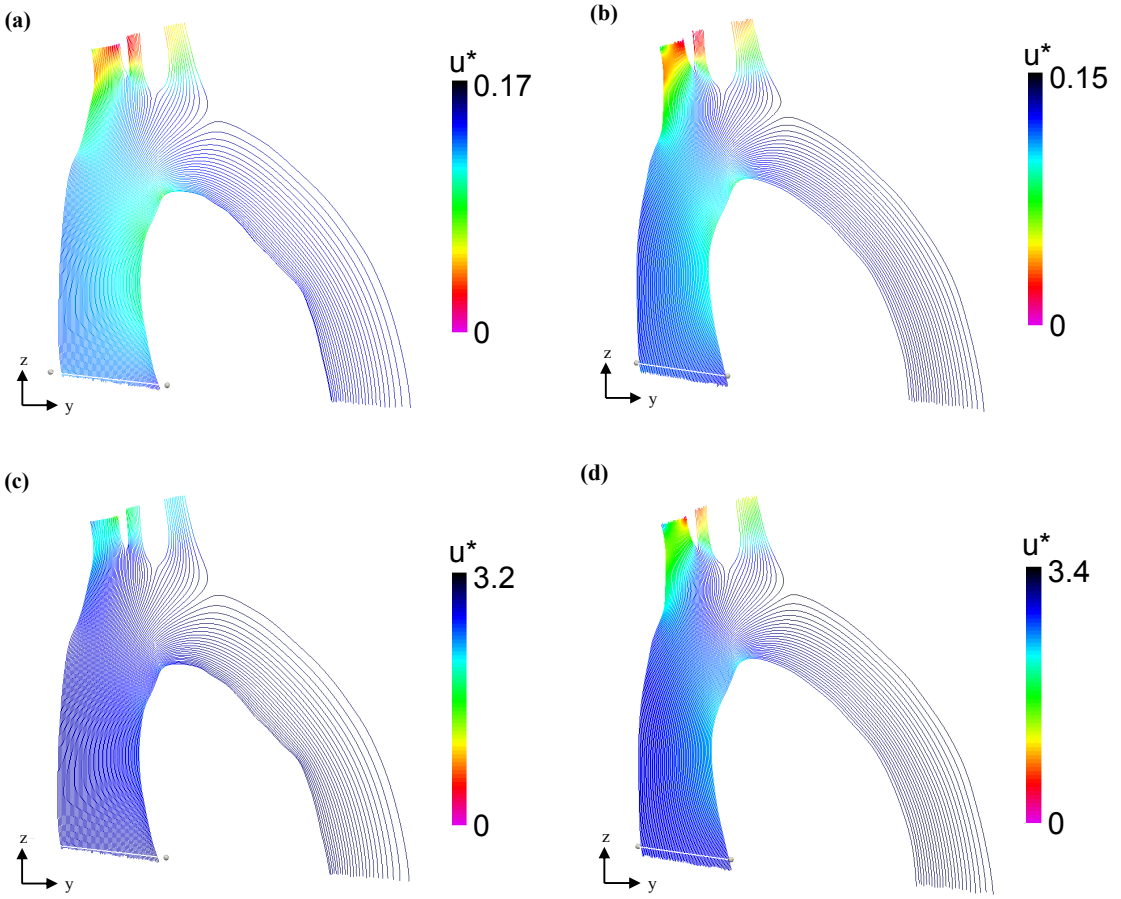

Figure 4.5: The phase-averaged velocity streamlines for NN at (a) 0.75s and (c) 0.25s, and NFR at (b) 0.75s, and (d) 0.25s.

the mid-plane of the aorta *Inlet* for both NN and NFR boundary conditions. These results show that the highest velocity in NFR is greater than that of NN. The flow patterns are similar for both cases with the maximum velocities generally appearing in the ascending aorta, aortic arch, and descending aorta regions. In both simulations, the lowest velocities are found within the first three outlets in the aortic arch. The streamlines coincide closely with the velocity contours in Figure 4.4, showing that the velocities at $t = 0.25$s are considerably larger than velocities at $t = 0.75$s, particularly through the first three outlets. The relative velocity magnitudes throughout the two simulations are generally consistent. However, the velocity through the first three outlets and first half of the main aorta pathway show some discrepancies between simulations NN and NFR, particularly during diastole and peak systole. During diastole, NFR boundary conditions slightly underestimate the flow

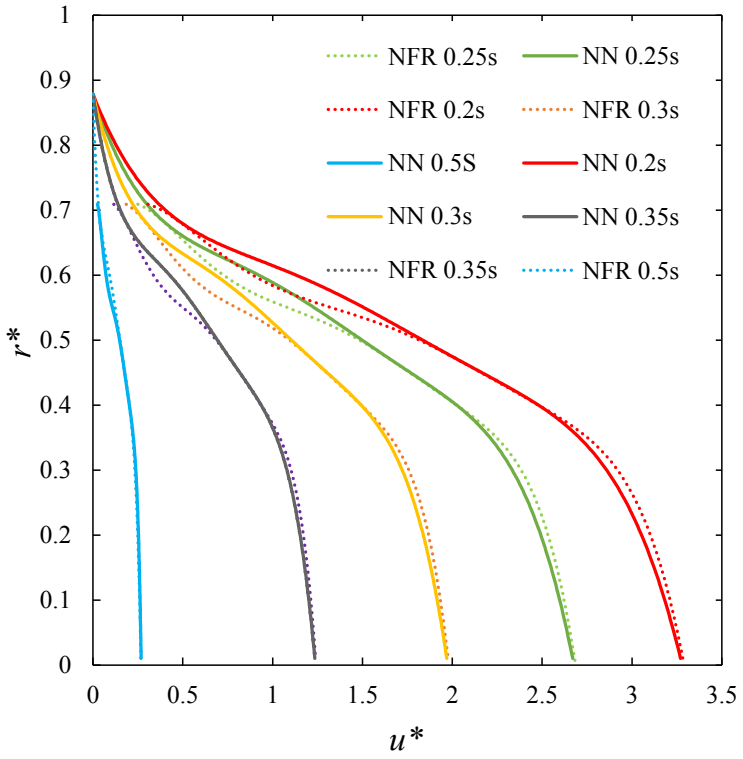

Figure 4.6: The phase-averaged streamwise velocity (u^*) profiles at 5 instants at $d^* = 2D$. Here, r^* is radius normalized by *Inlet* radius.

rate through *Outlet 3* and overestimates the velocity in regions near the ascending aorta proximal to the aortic arch, and near the bottom of the start of the aortic arch. During peak systole, NFR underestimates the velocity through the first three outlets by $\leq 40\%$. It also underestimates the velocity by the wall of the ascending aorta proximal to the aortic arch, and the bottom wall at the beginning of the aortic arch. The streamline and velocity contours from both simulations agree in principle with the results of Soudah *et al.*, 2016. However, NN results align more closely with their simulations, where the velocity at the aortic arch outlets reach a velocity similar to the maximum velocity during peak systole. Figure 6.1 of Soudah *et al.*, 2016, shows similar streamline results to the current study with the highest velocity in the ascending aorta and small sections of the descending aorta.

The velocity profiles were obtained at two cross-sections along the main aorta pathway at 5 instants throughout the cardiac cycle for both the NN and NFR boundary simulations. The plots in Figures 4.6 and 4.7 display the average normalized velocity along the radius of the aorta. The two cross-sectional areas are selected according to their radial distance along the main aorta pathway from the *Inlet*. Using the normal aorta modell, the cross-section at $d^* = 2D$ coincides with the start of the aortic arch region, and $d^* = 4D$ is at

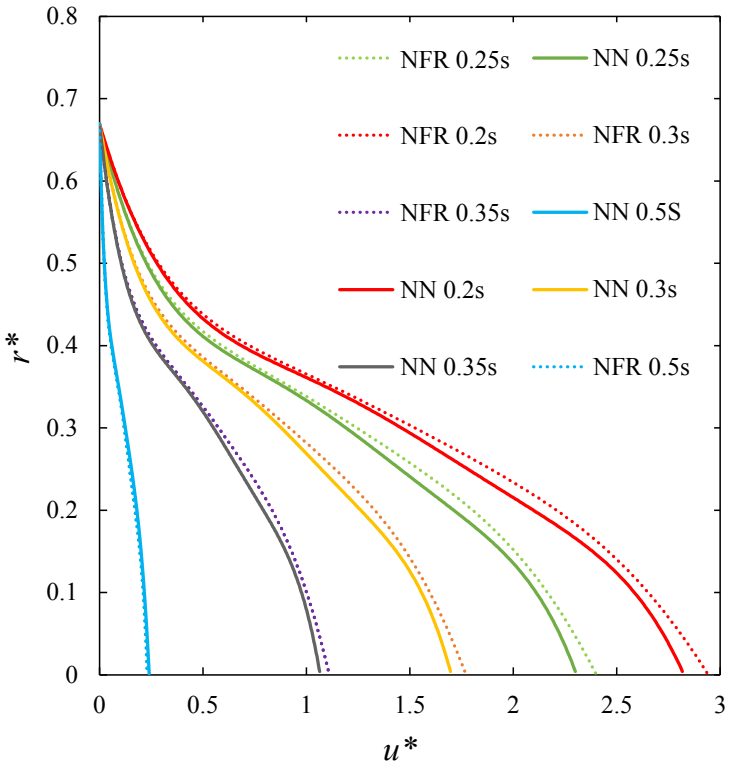

Figure 4.7: The phase-averaged streamwise velocity (u^*) profiles at 5 instants at $d^* = 4D$.

the start of the descending aorta. Figure 4.6 and 4.7 show that velocity profiles at the two cross-sections have the same trend regardless of the boundary conditions used. This can be explained physically as a fully developed flow profile that is affected by viscosity near the boundary layer. The normalized radius of the healthy aorta decreases from the *Inlet* to the aortic arch, and it continues to decrease at the descending aorta. For both simulations, the normalized velocity values show that the maximum velocity decreases slightly in the aortic arch compared to the *Inlet*. The maximum velocity decreases further as the flow travels through the descending aorta. Despite the cross-sectional averaged velocity decreasing as the blood moves into the descending aorta, it is evident that the velocity in NFR is greater than those in the NN simulation by $\approx 4\%$. The maximum velocity in the descending aorta is greater when using the flow rate outflow condition in NFR, while the velocity decreases at a similar rate relative to the maximum velocity as the blood moves further from the center of the main aorta pathway. This shows the same process as discussed with the previous streamline and velocity profiles since the velocity in the descending aorta must be increased in order to maintain the higher flow rate in the descending aorta. This is compensating for the decreased flow in the first three outlets when using flow rate boundary condition

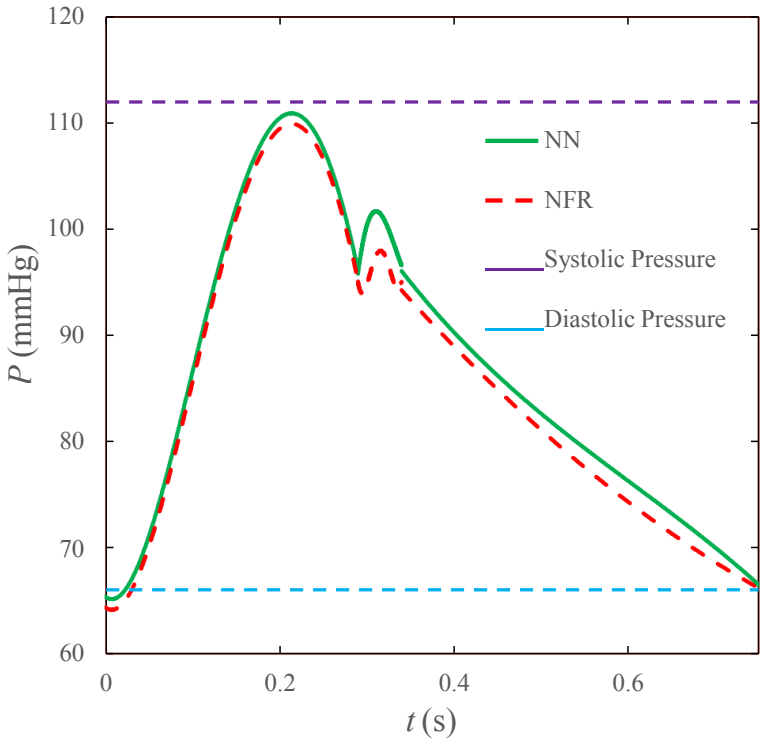

Figure 4.8: The phased-averaged blood pressure profile at aortic arch at 0.1s into the cardiac cycle for one period.

in NFR. The velocity profiles are similar to the previous results from Razavi *et al.*, 2011. The profiles at $d^* = 2D$ and $d^* = 4D$ clearly show similar trends to the velocity profiles in Figure 7 ($t = 0.1$s) of Razavi *et al.*, 2011. There are some differences between the two studies, which is mainly due to the different simulation setups. Particularly, Razavi *et al.*, 2011, imposed a fully developed velocity profile at the *Inlet* with no viscous effects, which is a common practice. However, patient-specific data suggests that the effects of blood viscosity is already present in the flow entering the aorta given that the blood flow has already gone through the heart and the capillaries prior to reaching the aorta. Thus, the *Inlet* flow profile with apparent viscous effects are imposed in the current study based on patient-specific measurements.

The velocity (Figures 4.6 and 4.7) and pressure (Figure 4.8) results from NN and NFC boundary conditions coincide consistently. The results in the main aorta pathway are very similar with a maximum difference of <5% in the estimation of blood flow velocity, and <4% in the prediction of blood pressure. Although the discrepancies between velocity profiles in regions of the main aorta pathway have been noted, the overall flow rate through each section of the main aorta pathway are very similar. The difference in results in each region

is generally within 5% amongst NN and NFR. Despite moderate discrepancies between the flow rates of each of the first three outlets, their relatively small proportion of outflow ensures that the main pathway flow rate remains consistent. Likewise, the pressure found in the main aorta pathway (Figure 4.8) remains consistent, and the small discrepancies in systolic and diastolic pressures are relatively negligible. Particularly, a difference of 4 mmHg does not greatly affect patient health evaluations. Intuitively, as the velocity through the first three outlets is influenced moderately by the choice of boundary condition, pressure and velocity parameters obtained in these regions are relatively inconsistent. From these results, it appears that pressure and flow rate outlet boundary conditions are essentially interchangeable if the results from the first three outlets are negligible, and the primary area of interest is in the main aorta pathway. If the results from the first three outlets are critical in medical analysis of a patient, the results obtained using the pressure outlet boundary condition (NN) agrees more closely with the experimental results of Olufsen *et al.*, 2000 and our patient-specific lab measurements that are used to validate these simulations later in Section 4.4.

Since the diameter is the largest in the aortic arch region near the first two outlets, and this region also corresponds to a region of high velocity, the peak local Reynold's number is expected to occur in this area. The overestimation of velocity by NFR boundary conditions in the region near the first three outlets causes peak local Reynolds number to be overestimated as well. During the diastolic cycle at 0.75s, the peak local Re occurs in the ascending aorta, where $Re_{u-max} = 430$ and 419 in NN and NFR, rsepectively. NN produces a larger peak Re during diastole, but this Re corresponds to a flow well within the laminar regime, and transition to turbulence is not expected. During the systolic cycle at 0.25s, the peak Re increases to 8169 in NN and 9764 in NFR, reaching the regime where transition to turbulence may occur. Furthermore, $Re_{u-max} = 8000$ is not unusual during systole in healthy patients, but $Re > 9000$ is uncommon in patients with average cardiac output (Stein and Sabbah, 1976). This may lead to a non-physical prediction of transition to turbulence. Since transition to turbulence is undesirable in the aorta, this occurrence may predict unhealthy behaviour when no significant activity is physically present. Due to this shortcoming, pressure boundary conditions (as in NN) are preferred if transition to turbulence is a key concern.

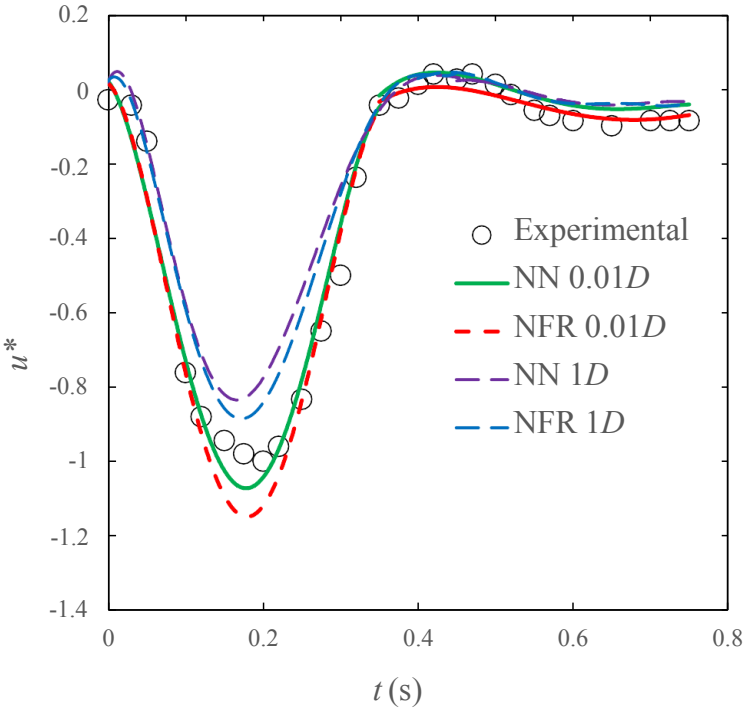

Figure 4.9: The phase-averaged streamwise velocity $0.01D$ and $1D$ from *Outlet 4* of the normal aorta.

4.4 Experimental Validation

Velocity measurements are used to validate the simulation results against experiments at a distance from *Outlet 4* to avoid numerical interference from the boundary condition. Moreover, pressure profiles are obtained from the aortic arch to compare systolic and diastolic pressure to patient-specific measurements. The numerically obtained velocity results are validated in comparison to experimentally obtained velocity data in the descending aorta. This provides both a mechanism to validate the main blood flow results, and demonstrate how the changes in outlet boundary condition can impact the accuracy of simulation results compared to real world velocity data in the descending aorta. Patient-specific velocity data collected at *Outlet 4* for an entire cardiac cycle is compared to simulation results for the NN and NFR cases proximal to Outlet 4 in Figures 4.9, 4.10, and 4.11.

By measuring simulation results at $1D$, $0.5D$, $0.1D$ and $0.01D$ away from the outlet, the velocity measurements in the nearby region can be compared to experimental measurements for validation. The experimental measurements consist of a fully developed flow profile collected at 28 instants during a single cardiac cycle, which was cycle-averaged and connected point by point. In contrast, both the NN and NFR simulation results are represented by

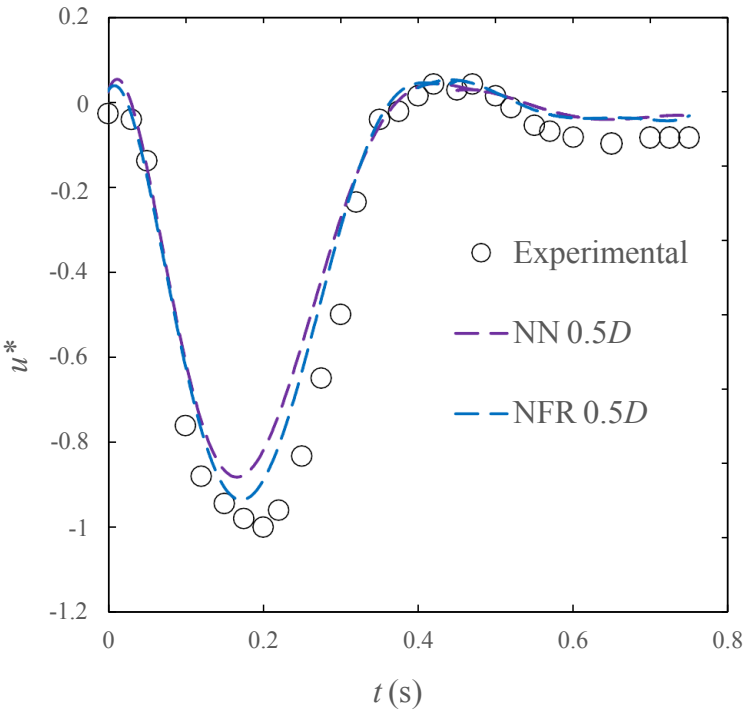

Figure 4.10: The phase-averaged streamwise velocity $0.5D$ from *Outlet 4* of the normal aorta.

piecewise polynomial functions in Figures 4.9, 4.10, and 4.11 to remain consistent with the idealized *Inlet* flow waveform (Crosetto *et al.*, 2011). It is evident that the simulation results depict the same trend during both systole and diastole, with magnitudes that are relatively consistent apart from peak systole at each of the regions used for measurement. The average velocity profile at each of the four considered distances show a similar trend, with discrepancies in magnitude of velocity and time of peak systole. As the distance from *Outlet 4* is increased, the velocity magnitude at peak systole decreases. This is because the aorta radius increases while flow rate remains constant. The velocity during the diastolic cycle is also decreased as the distance to *Outlet 4* is increased. Compared to experimental measurements, the idealized polynomial functions at $0.1D$ and $0.01D$ from *Outlet 4* in Figures 4.9 and 4.11 provide a fairly accurate solution, but overestimates the velocity during peak systole. From experimental measurements, the maximum velocity magnitude is 1.02, or 2% higher than the maximum inlet velocity during peak systole. At a distance of $0.01D$ away from *Outlet 4* in Figure 4.9, the idealized flow waveform in NN results in a maximum velocity of 1.08, while NFR boundary conditions result in a maximum velocity of 1.15. To compensate for this increase in maximum velocity, the idealized flow profile has a shorter systolic cycle, and the total flow rate over a cardiac cycle is fairly consistent between sim-

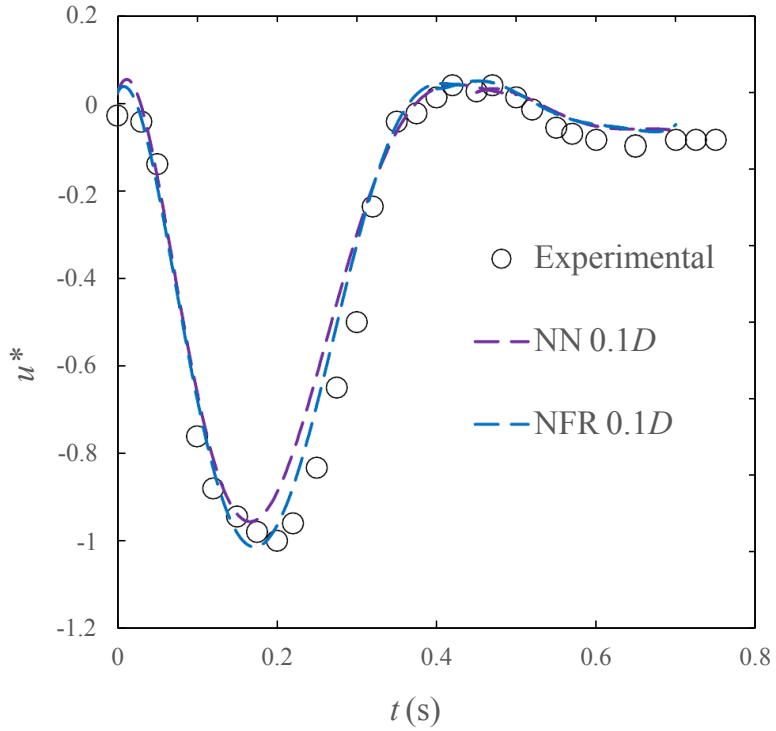

Figure 4.11: The phase-averaged streamwise velocity $0.1D$ from *Outlet 4* of the normal aorta.

ulation NN and experimental measurements with less than 2% discrepancy. As expected from previous velocity and pressure results, the velocity in NFR is overestimated compared to both NN and experimental measurements. When using the idealized flow waveform at $0.01D$ to estimate the total flow rate per cardiac cycle, NFR boundary conditions overestimate the flow rate through *Outlet 4* by approximately 5% compared to experimental measurements.

The pressure profile can be validated in a similar manner, by comparing patient-specific systolic and diastolic pressure measurements to the pressure profile that can be obtained numerically for an entire cardiac cycle. The pressure profile was obtained by phase-averaging the pressure at a cross-section in the middle of the aortic arch over 28 full cardiac cycles starting at 0.1s into the cardiac cycle, which coincides with the beginning of the systolic cycle. This procedure is consistent with previous experiments by Olufsen *et al.*, 2000, in which they showed that the pressure profile at various locations throughout the main aorta pathway remains consistent. The pressure profiles in Figure 4.8 appear similar to the experimental measurements obtained from Olufsen *et al.*, 2000. However, the simulation pressure profiles are smoother and show less complexity than their experimental measurements. This

is attributed to the idealization of the inlet velocity periodic flow waveform, and the use of smooth piecewise parabolic functions to model trends from discrete measurement points. The phase-averaging of results also contributes to the smoothing of the pressure profile. The pressure profiles from the NN and NFR simulations are similar, with pressure profiles from NN having a greater maximum and minimum pressure values. The pressure profile reacts to the effects of periodic flow inlet velocity at the same rate during both simulations, and any possible shifts in reaction time are negligible. The maximum pressure during the systolic phase represents the systolic pressure in patients, and the minimum pressure occurs during the diastolic phase, which is known as the diastolic pressure. From the NN simulation results, the systolic pressure is 111 mmHg, while the diastolic pressure is 66 mmHg. For the NFR simulation results, the systolic and diastolic pressures are both lower than those of NN, at 108 mmHg and 64 mmHg, respectively. The current results coincide closely with the patient pressure lab measurements of 112 mmHg and 66 mmHg for systole and diastole, respectively. The pressure in the middle of the aortic arch region was expected to be lower when using flow rate boundary conditions (NFR), as the velocity in the proximal region of the aortic arch and descending aorta are higher than those in their respective regions in NN. As the flow rate through the first three outlets is lower, NFR boundary conditions would require a higher flow rate in the descending aorta to ensure a steady state solution, which is required to conform to physical expectations. As the flow rates are specified, in order to increase the flow rate in the descending aorta, the pressure must decrease and the relative pressure in the first three outlets must increase.

The results from NN and NFR simulations both show great consistency with experimental measurements. Velocity profiles from both numerical simulations show accuracy within 5% of experimental measurements, and clearly display a similar trend throughout the cardiac cycle. Systolic and diastolic pressure magnitudes were also relatively consistent between numerical results and experimental measurements, with a deviation within 5%. Having validated the accuracy of the simulation setup with 2 different types of boundary conditions, we are able to conduct simulations using both the normal and abnormal aorta and expect results with similar accuracy.

4.4.1 Effects of Elastic Modulus

The modulus of elasticity was used as a control variable, which was kept the same for both subjects. Previous studies had shown that the aorta wall displacements are small relative to the aorta diameter, so small changes in elasticity are expected to not significantly alter the

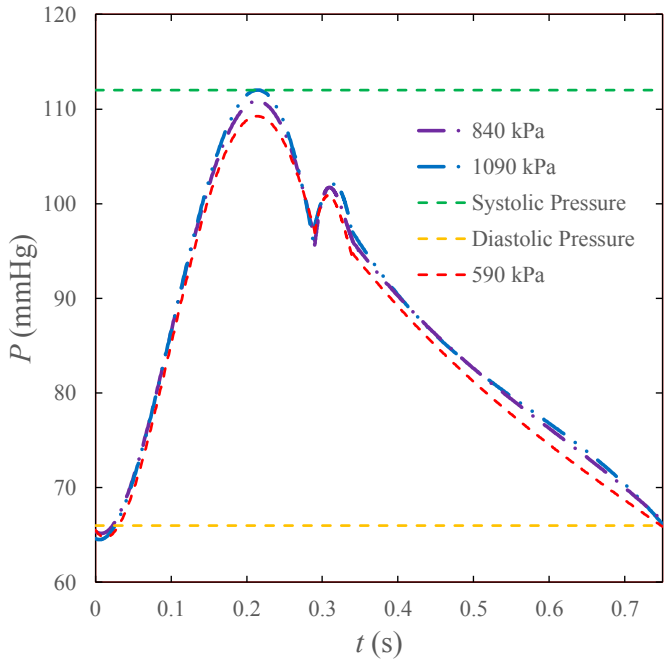

Figure 4.12: Pressure profile at mid aortic arch ($3D$) using 3 different elasticity values.

flow pattern (Danpinid *et al.*, 2010). We further verified this assumption by repeating the NN simulations for three elasticity values: 590 kPa, 840 kPa, and 1090 kPa, representing the selected elastic modulus value used in the current study, and one standard deviation above and below it (Khamdaeng *et al.*, 2012). This parametric study identified no major changes to the flow pattern. Changes in pressure were negligible, within <3% (Figure 4.12), while velocity magnitudes varied up to 10% with very similar trends (Figure 4.13).

4.5 Summary

We examined the implications of using either pressure or flow rate outlet boundary conditions on simulating the blood flow in a normal aorta based on patient-specific data. The velocity profiles show similar trends along the aorta between both the NN and NFR simulations using the outlet flow rate and outlet pressure boundary conditions. Past the midpoint of the aortic arch, the effects of the first three outlets on velocity become negligible and velocity streamlines and profiles become nearly identical between the two simulations. There are slight discrepancies in velocity in the ascending aorta and beginning of the aortic arch between the two simulations, where the flow rate boundary condition leads to an overestimation of the velocity in the region near the bottom of the aorta during diastole. This coincides with an underestimation of the velocity in the same region during peak systole in

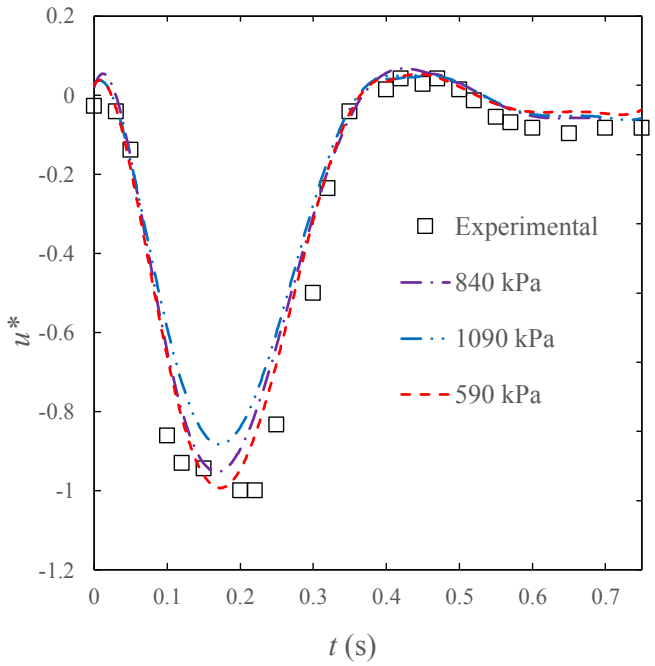

Figure 4.13: Velocity profile at $0.1D$ from *Outlet 4* using 3 different elasticity values.

the flow rate simulation. The largest discrepancy is in the velocity through the outlets of the aortic arch during peak systole, which is underestimated using the flow rate boundary condition at the outlets. As the model and *Inlet* conditions remain identical in both simulations, the decreased velocity results in an underestimation of the flow rate through the first three outlets. This is compensated by an increased flow rate through *Outlet 4* in the the descending aorta. From the results of the velocity profiles in the region proximal to the descending aorta outlet, it is evident that the flow rate boundary condition leads to an overestimation of flow rate through the fourth outlet compared to experimental measurements, and subsequently an underestimation of flow rate through the first three outlets.

The pressure profiles in both simulations show similar trends, although the systolic and diastolic pressures in the aortic arch are higher using the pressure outlet condition. The systolic and diastolic pressures were 111 mmHg and 66 mmHg, respectively. However, the systolic and diastolic pressures were 108 mmHg and 64 mmHg, respectively with the flow rate condition imposed at the outlets. This decrease in pressure in the aortic arch results in an increased relative pressure in the first three outlets, which can be attributed to the greater flow rate through the aortic arch into the descending aorta leading to higher velocity.

The results from these simulations show that the general trends found in pressure and velocity results are similar regardless of the imposed outlet boundary conditions. With

this information, alongside the understanding of slight discrepancies that occur in the main aorta pathway and the outlets at the aortic arch, patient-specific simulation templates can be obtained within reasonable consistency using either patient pressure or flow rate data at the outlets. This signifies a notable contribution for the overarching research by ensuring that simulations can be compensated to reach adequate accuracy regardless of the outlet parameters available from the patient based on available equipment and technology at the medical facility. However, pressure boundary conditions are preferred when transition to turbulence is a key consideration since the flow rate boundary conditions overestimate peak local Reynolds numbers.

Chapter 5

Abnormal Aorta Geometry [2]

5.1 Introduction

This chapter looks at the flow disturbances in the abnormal aorta due to geometrical anomalies, mainly the aorta coarctation and narrowing of the aortic arch due to an indentation. Details on the anomalies and the numerical setup can be found in Section 1.4 and Chapter 3, receptively. Based on the validated results obtained from the normal aorta simulations in Chapter 4, the same numerical setup is employed for the abnormal aorta model. Both the model geometry and boundary conditions are modified for the abnormal aorta.

5.2 Velocity and Vorticity

Blood flow can be characterized using pressure, velocity and vorticity fields. Here, the general blood flow pattern inside the main aorta pathway is examined using velocity and vorticity fields for the normal and abnormal aorta models. The trends in the normalized velocity and vorticity contours are relatively consistent between the NN and AA simulations along the majority of the main aorta pathway. The areas of significant deviation occur in the two regions of interest that correspond to the indentation in the aortic arch, and the aorta coarcation. The contour of velocity during peak systole in Figures 5.1 and 5.2 show similar blood flow in the ascending aorta for both cases, which quickly deviates from normal behavior when blood approaches the aortic arch. Moreover, it is evident from the magnitude of velocities in Figures 5.1 and 5.2 that the flow rate in the normal aorta is greater than that of the abnormal aorta. This is mainly due to the increased aorta radius and the higher inlet velocity obtained from Subject 1 with the normal aorta. Moreover, it is evident

[2]The results in this chapter are part of a publication currently under review in the Journal of Applied Mechanics: Jia, Y., Punithakumar, K., Noga, M., Hemmati, A. (2020) Blood flow manipulation in the aorta with coarctation and arch narrowing for pediatric subjects. *J. of Applied Mechanics*.

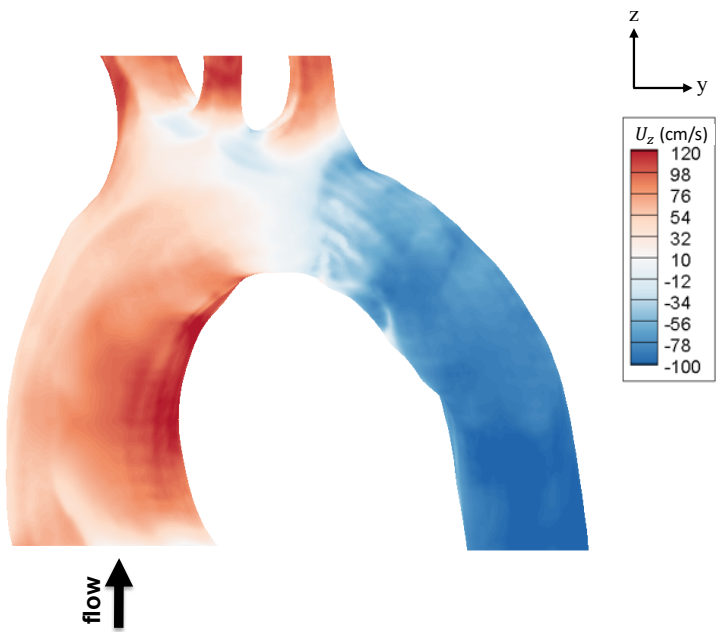

Figure 5.1: Velocity Z-Component contour in NN simulation during peak systole.

that a slightly higher velocity through *Outlet 1*, *Outlet 2* and *Outlet 3* of the abnormal aorta attributes to a slightly elevated blood flow rate compared to a normal aorta. In the ascending aorta, the regions of high velocity generally occur near the top and bottom of the aorta with the regions of high velocity varying throughout the cardiac cycle.

The geometrical anomaly in the narrowed aortic arch, referred to here as the indentation, causes a large discrepancy in blood flow relative to the normal aorta. The indentation is located at the inferior aspect of the mid aortic arch. Along the leading edge of the indentation, there is a region of high velocity (see Figure 5.2) that redirects the flow upwards towards the middle of the main aorta pathway. On the trailing edge of the indentation, there is a region of low velocity that attributes to the decrease in blood flow because of the flow deflections at the leading edge. This geometrical anomaly contributes to the increase in flow rate through the first three outlets, which is disproportional to the change of flow rate at *Outlet 1* of the abnormal aorta. The redirecting of the flow stream at the bottom of the aortic arch displaces the flow towards *Outlet 2* and *Outlet 3* in the middle of the main aortic arch in the upward direction. In the normal aorta, the region at the bottom of the aortic arch has the highest flow velocity in the aorta (see Figure 5.1). This hints that a flow manipulator could be used close to the indentation to deflect the flow such that it reverts the effect of the indentation. With such flow manipulation, there will not be a need for correcting the aorta geometrical shape through reconstruction surgeries.

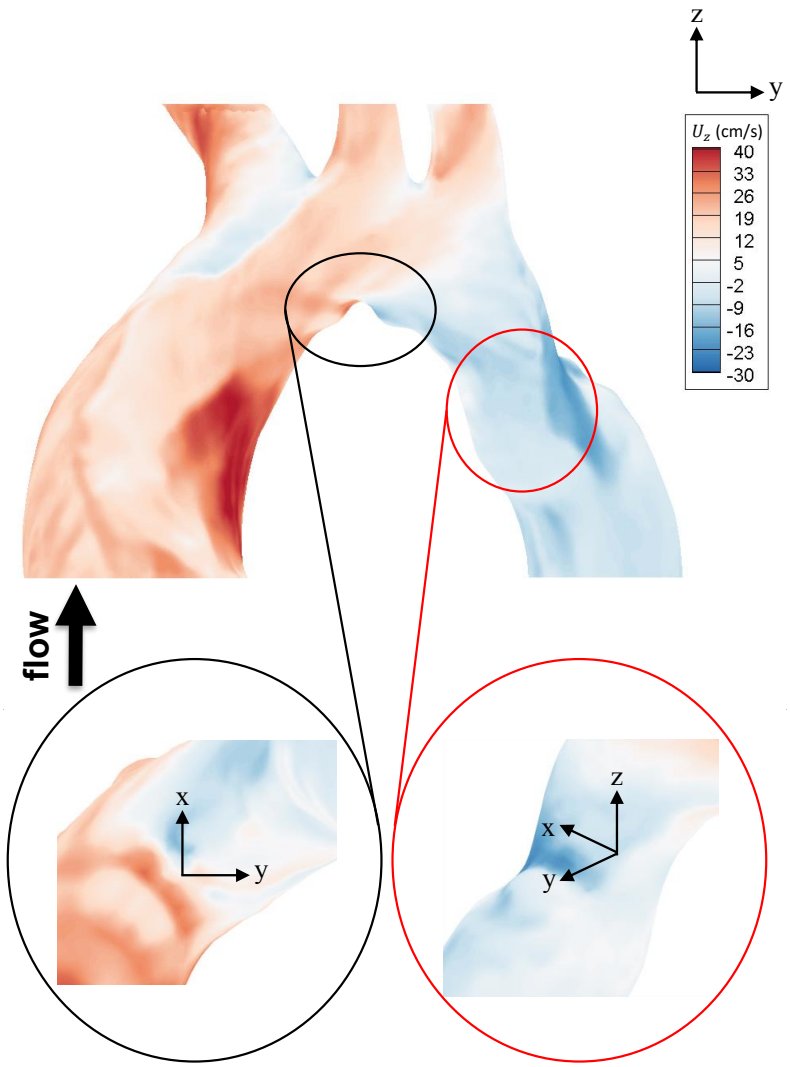

Figure 5.2: Velocity Z-Component contour in AA simulation during peak systole with detailed view of regions of interest.

Now we switch our attention to the vorticity field in the aorta. There are small regions of low vorticity identified during the diastolic cycle in both cases. However, there appears to be an increase in vorticity during the systolic cycle mainly in the region near the top of the ascending aorta. Looking at the vorticity contours of Figures 5.3 and 5.4 during the systolic peak, there are regions of significant vorticity generation with a higher concentration of rotational flow at *Outlet 1*. This behavior is similar for both normal and abnormal aortas in the ascending aorta regions. However, there is an apparent difference between the two cases beyond the first outlet of the aorta, where there exists a indentation in the abnormal aorta.

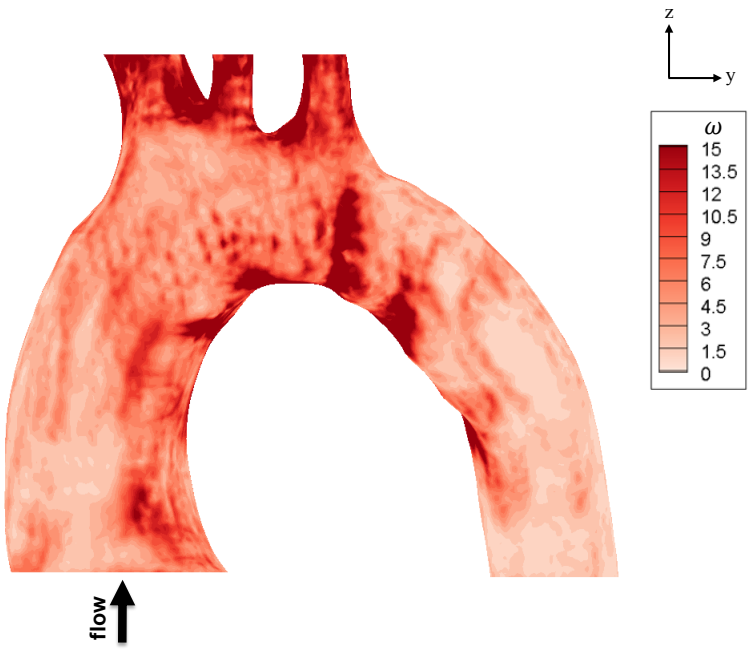

Figure 5.3: Vorticity magnitude contour in NN simulation during peak systole.

The vorticity trends seen in the region near the bottom of the ascending aorta continue throughout the aortic arch and descending aorta of the normal model following the systolic peak. The region of peak velocity in Figure 5.1 at the bottom of the aortic arch shows low magnitudes of vorticity even during peak systole (Figure 5.3). In contrast, the indentation in the abnormal aorta creates a region of high vorticity at the bottom of the aortic arch (Figure 5.4). The voriticity near the bottom of the aorta show similar trends during systolic cycle for both models until the indentation. At the indentation, this vorticity is redirected upwards, towards the middle of the main aorta pathway, which is consistent with the redirection of the flow previously identified for the abnormal aorta. Shortly following the indentation, there is a region of high vorticity along the bottom of the aortic arch that is not seen in the normal aorta. This is mainly attributed to the flow separation at the indentation, which leads to recirculatory flow immediately after the indentation. This flow feature is naturally accompanied by a rise in vorticity and reduced pressure. This region of high vorticity and low velocity has physical and medical implications since it increases the risk of blood clot formation. Once again, these conditions are classically addressed in fluid engineering, e.g., pipeflow, using flow manipulators to suppress the formation of recirculatory regions and generation of vorticty by redirecting and controlling the flow separation.

The aortic coarctation also causes a significant discrepancy in the velocities (Figures 5.1 and 5.2) between the two models and a slight deviation in vorticity (Figures 5.3 and

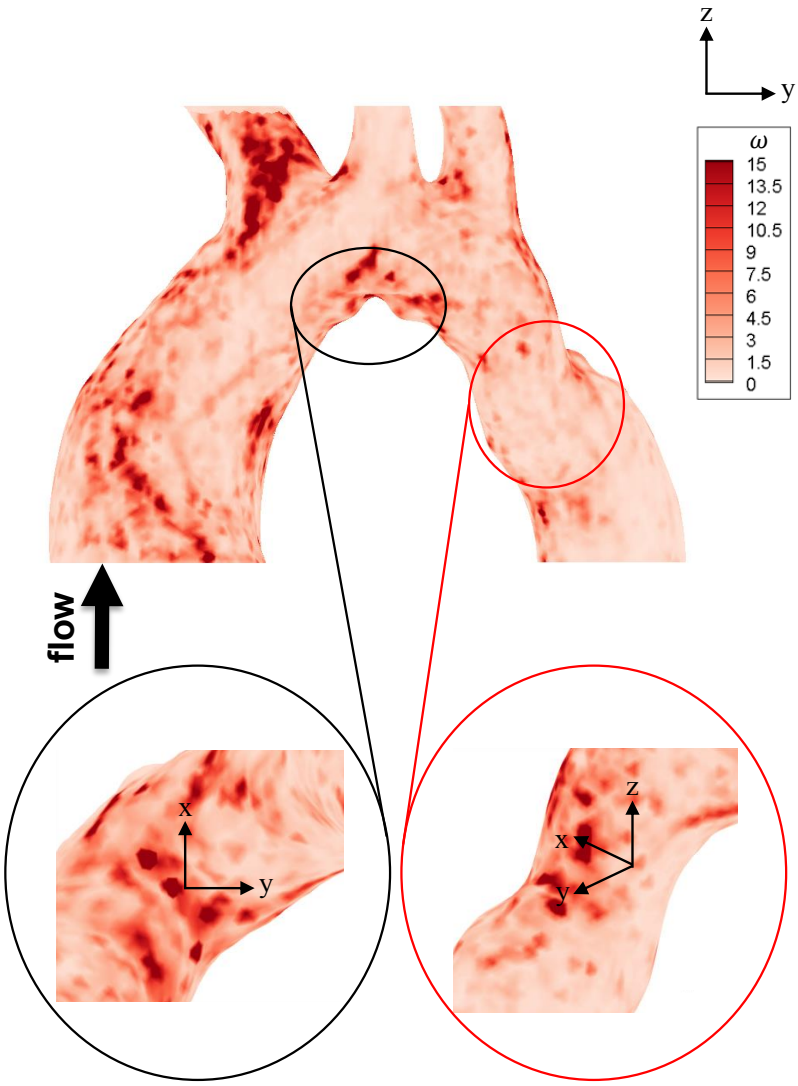

Figure 5.4: Vorticity magnitude contour in AA simulation during peak systole with detailed view of regions of interest.

5.4). At the coarctation, the flow velocity in Figure 5.2 is elevated compared to the rest of the descending aorta. In particular, there is an area of high velocity near the top of the coarctation, which further elevates shortly after exiting the coarctation. There are also two regions of low velocity, one near the bottom of the aorta at the beginning of the coarctation and one at the top end of the aorta shortly after the end of the coarctation. These regions of high and low velocities are not observed for the normal aorta case in Figure 5.1, which can be attributed to the modified geometry of the abnormal aorta. The regions of low velocity in Figure 5.2 occur because the geometry of the coarctation causes flow to be redirected

away from these regions, while the regions of high velocity occur due to the narrowing of the aorta. This redirects blood flow into a smaller cross-section, relative to the larger opening of the normal aorta. At $0.5D$ after the end of the coarctation, the region of high flow velocity fully disperses into the greater cross-sectional area, and the low velocity region is also resolved. Thus, the velocity profile of the normal model is recovered, albeit with a lower velocity magnitude due to the decreased flow rate in the abnormal aorta at *Outlet 4*. It is evident that the presence of the geometrical anomalies in the aorta lead to a slower blood delivery to the lower body through *Outlet 4*. This also has implications on blood pressure, which is discussed later in this section.

The abnormal aorta simulation using patient-specific boundary conditions obtained from Subject 1 with the normal aorta (AN simulations) was meant to provide insight into the mechanism the body adapts to address the flow deflections caused by the geometrical anomalies. However, comparing the results of AN and AA simulations show very similar trends in velocity and vorticity distributions, which does not provide an explanation for the deviation of flow velocity in the abnormal aorta. In the AN simulation, the vorticity (Figure 5.5) is slightly elevated in regions of high vorticity, particularly near the *Inlet*, *Outlet 1*, the inferior aspect of the mid aortic arch, and the coarctation. However, this can be explained by the increase in absolute (not normalized) velocity throughout the aorta.

The Neumann boundary condition at the outlets, in place of patient-specific data, increases velocity slightly through *Outlet 1*, *Outlet 2* and *Outlet 3*. There also exists a slightly lower velocity through the descending aorta, as shown in Figure 5.6, which is attributed to the numerical feature of the Neumann boundary condition at the three top outlets. However, since the flow rate through *Outlet 1*, *Outlet 2* and *Outlet 3* is higher than past experimental measurements, one can argue that the Dirichlet patient-specific boundary condition is a better option in obtaining physical simulation results. This inaccuracy can be alleviated by cropping the aorta models further up, which allows the flow characteristics in the three outlets to further develop. Regardless, the velocity trends show good consistency using both Dirichlet and Neumann boundary conditions. Similarly, the vorticity behavior is fairly similar amongst corresponding simulations (NN-NNeu and AA-ANeu).

5.3 Pressure

The pressure trends remain relatively consistent between the NN and AA simulations along the ascending aorta pathway (for example, see Figures 5.7 and 5.9). The pressure waveform varies between each simulation, as the changing boundary conditions have non-negligible

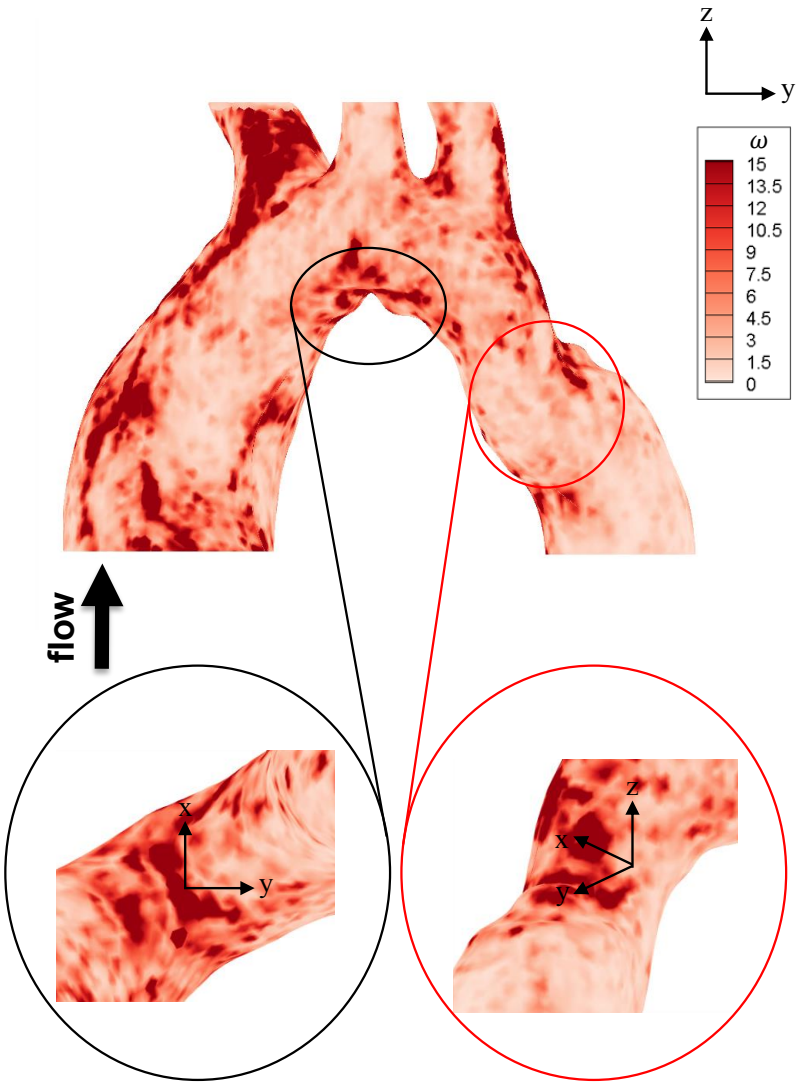

Figure 5.5: Vorticity magnitude contour in AN simulation during peak systole with detailed view of regions of interest.

effects on pressure throughout the cardiac cycle. There are also slight discrepancies in the aortic arch between simulations using the Dirichlet boundary condition and their corresponding cases with the Neumann boundary condition. This is mainly due to the increased flow rate through the first three aorta outlets when using Neumann boundary conditions. In comparison, NNeu and ANeu simulations overestimated the pressure at *Outlet 1*, *Outlet 2* and *Outlet 3*, while underestimating the pressure at approximately $3D$ downstream. There also appears to be a continuously lower pressure throughout the descending aorta in Figure 5.8 and 5.10. However, the phase average results of NN simulations are consistent with

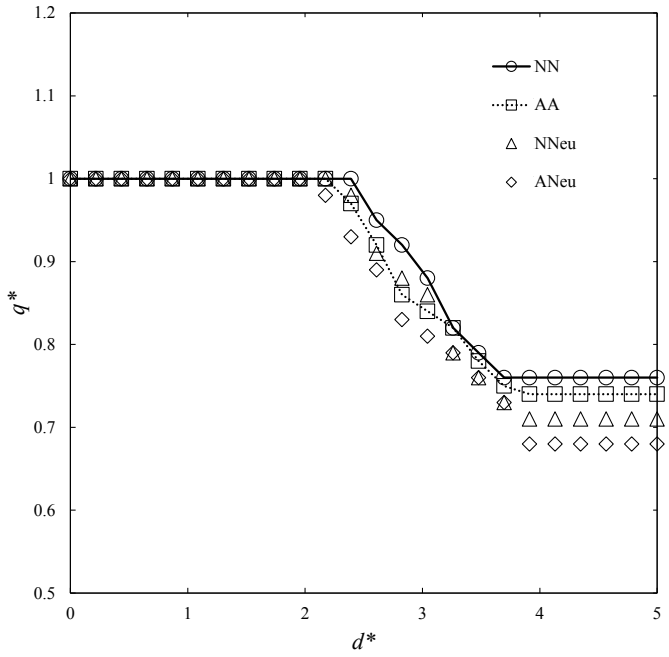

Figure 5.6: Blood flow rate through the main aorta pathway.

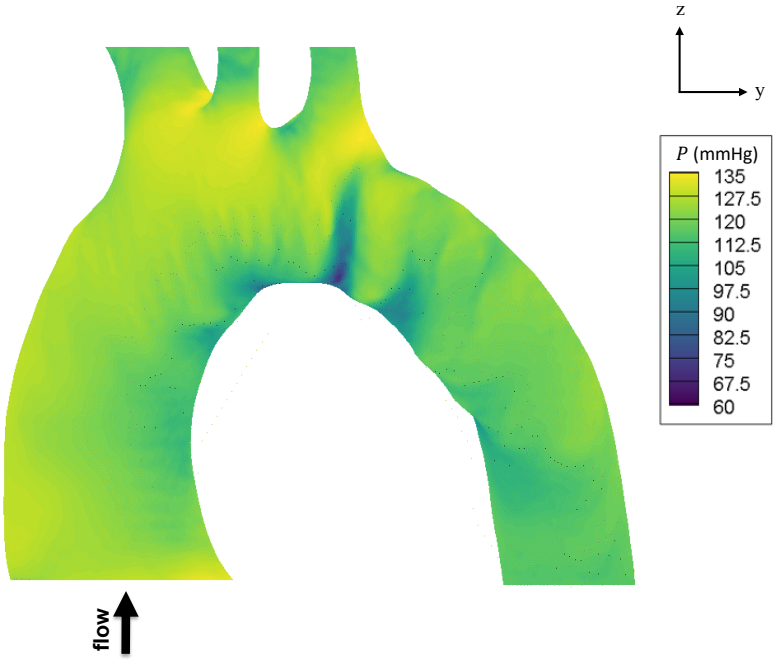

Figure 5.7: Pressure contour in NN simulation during peak systole.

experimental measurements. Overall, the trends between all corresponding simulations are moderately consistent. In all the simulations (e.g., Figures 5.7 and 5.9), the ascending aorta and *Outlet 1* experience the highest overall pressure, while the pressure drops as the flow

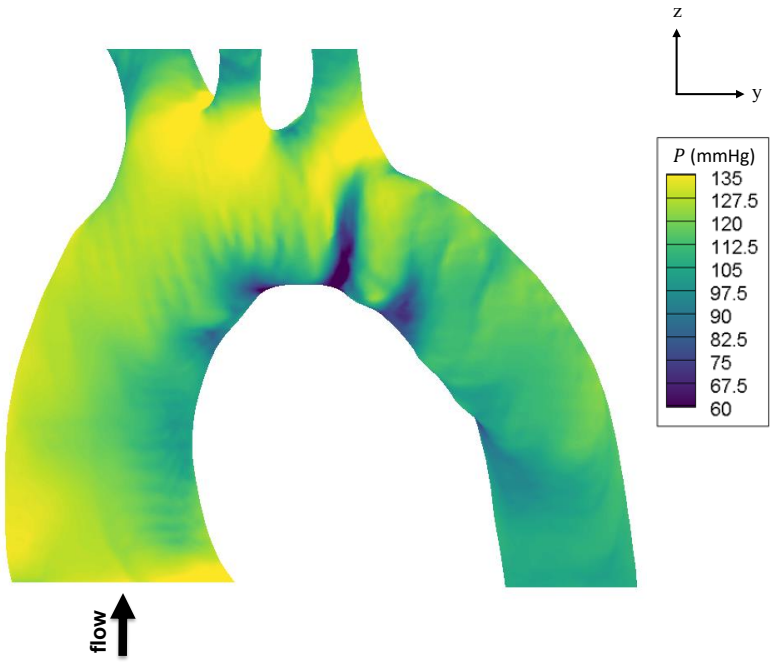

Figure 5.8: Pressure contour in NNeu simulation during peak systole.

continues to travel into remaining parts of the aorta. During the systolic cycle, there are small regions of lower pressure near the bottom of the aorta, which move with the primary flow. There are also some regions of lower pressure near the branching of *Outlet 1*, *Outlet 2* and *Outlet 3* from the aortic arch.

The area around the indentation in the abnormal aorta in Figure 5.9 shows a significant pressure drop that does not coincide with the trend of pressure in the corresponding region in Figure 5.7 for the normal aorta. Although a pressure drop at the bottom of the aortic arch is expected even in normal patients, the size and magnitude of the pressure drop are far more severe for the abnormal case. On the leading edge of the indentation, there is a region of lower pressure that extends halfway to the top of the aortic arch with a more concentrated pressure drop closer to the bottom of the aortic arch. There is also a small region on the leading edge that does not show a lower pressure, which has the characteristics of a recirculation zone. Above the middle of the indentation, however, there is no evidence of a low pressure region. On the trailing edge of the aortic arch, there is another region of low pressure that propagates to roughly halfway to the top of the aorta. The maximum pressure drop in this region is less pronounced since the low pressure regions still exhibit values of pressure higher than those at the indentation leading edge despite a lower pressure in the main aorta pathway. This low pressure flow in the bottom half of the aorta propagates

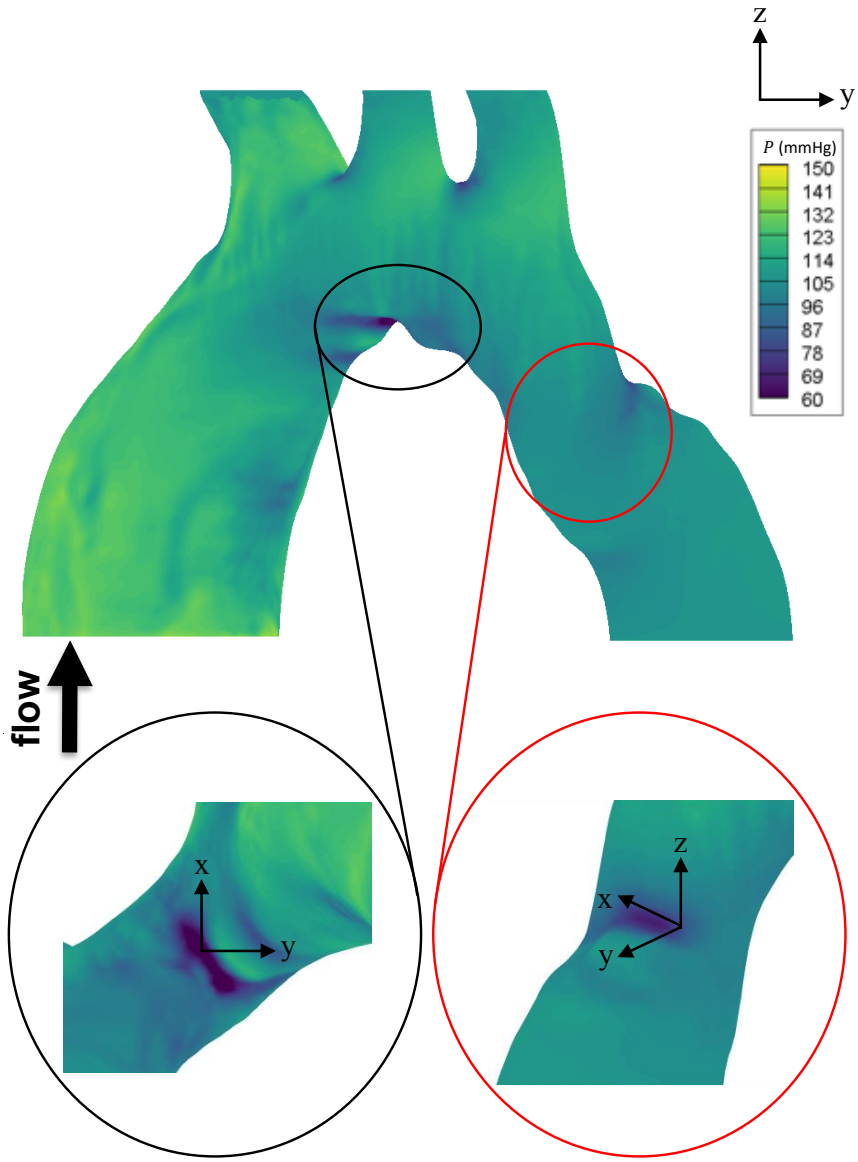

Figure 5.9: Pressure contour in AA simulation during peak systole with detailed view of regions of interest.

to the descending aorta and the start of the coarctation.

The abnormal aorta simulations depict a clear pressure drop in the aortic coarctation in Figure 5.9 compared to their corresponding normal models (Figure 5.7), which does not fully recover past the coarctation. The pressure drop between the aortic arch and $d^* = 5.3D$ (approximately $0.5D$ after the end of the coarctation) is clearly identifiable in Figure 5.11. At the beginning of the coarctation, there is a low pressure region near the bottom of the descending aorta, which propagated from the trailing edge of the indentation. In the

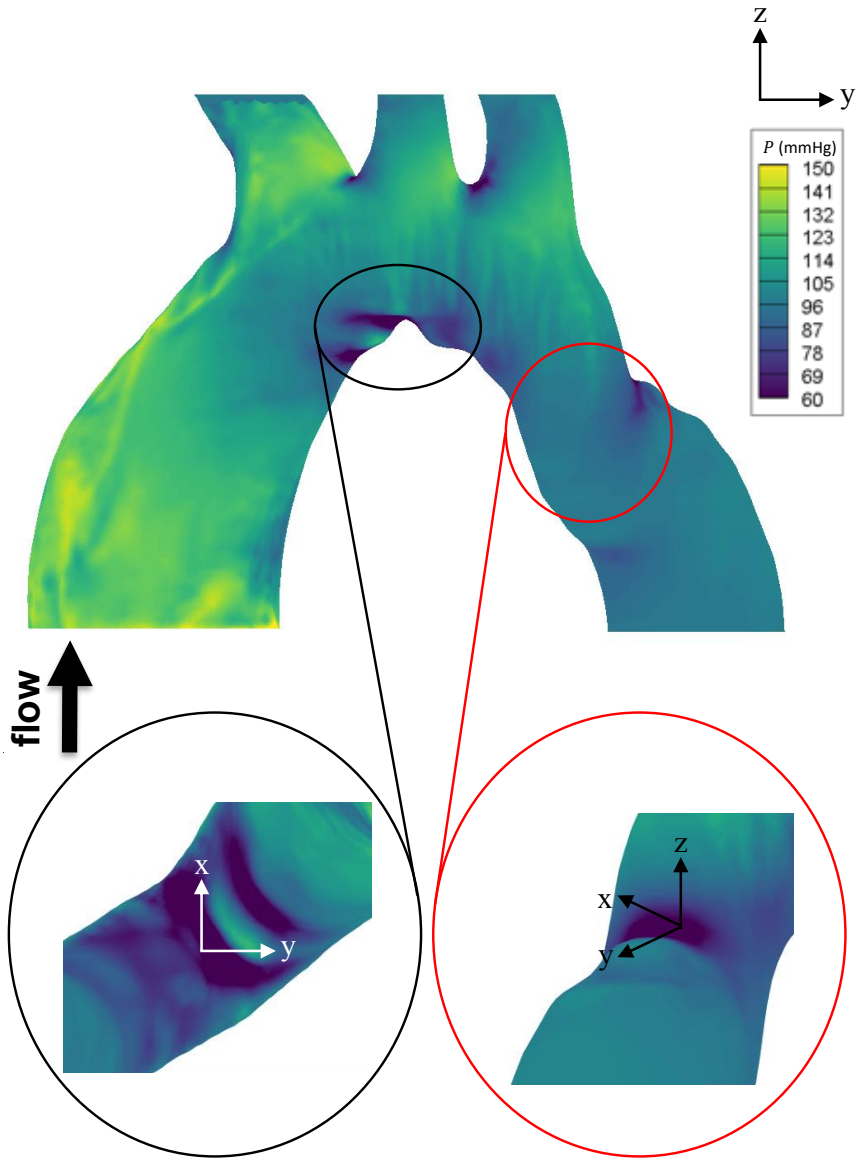

Figure 5.10: Pressure contour in ANeu simulation during peak systole with detailed view of regions of interest.

coarctation, the pressure recovers slightly at the lower wall of the aorta, but it decreases significantly towards the upper wall. The majority of the main aorta pathway experiences a considerable pressure drop of 21 mmHg on average compared to the flow prior to the coarctation. Near the end of the coarctation, there is a region with a significant pressure drop (see Figure 5.11) that is far greater than any drops observed in either normal and abnormal models. This area corresponds to the region of high velocity that was discussed earlier, and it is also magnified in Figure 5.9. After the end of the coarctation, pressure

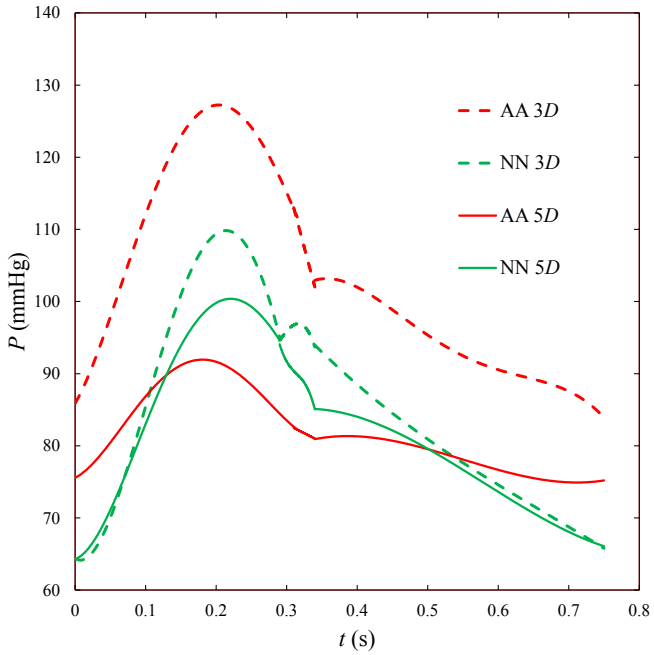

Figure 5.11: Pressure measured over a cardiac cycle at $d^* = 3D$ (midpoint of aortic arch) and $d^* = 5D$ ($0.5D$ after end of coarctation).

begins to recover towards its pre-coarctation values. After a distance of $0.3D$ from the end of the coarctation, the pressure drop is no longer visually noticeable. However, there was a pressure drop of 28 mmHg between the middle of the aortic arch at $d^* = 3D$ and $0.5D$ past the coarctation at $d^* = 5.3D$. The pressure drop through the same length along the normal descending aorta region was only 7 mmHg. This implies that as predicted, the narrowing of the aorta and the blood delivery interruption, impacts the blood pressure as well, which can be more easily monitored in patients.

5.4 Wall Shear Stress

The wall shear stress distribution is similar for the normal and abnormal aorta models in the ascending aorta in Figure 5.12. Away from the aorta indentation and coarctation, the wall shear stress remains fairly low throughout the cardiac cycle with small regions of high wall shear stress at the branching splits between *Outlet 1*, *Outlet 2* and *Outlet 3* during the systole. In both models, the areas with moderate wall shear stress occur at the top of the ascending aorta, the bottom of the aortic arch, and at the branches of *Outlet 1*, *Outlet 2* and *Outlet 3*. These areas are identified in Figure 5.12. The maximum wall shear stress at each of these corresponding areas for each simulation is listed in Table 5.1, which

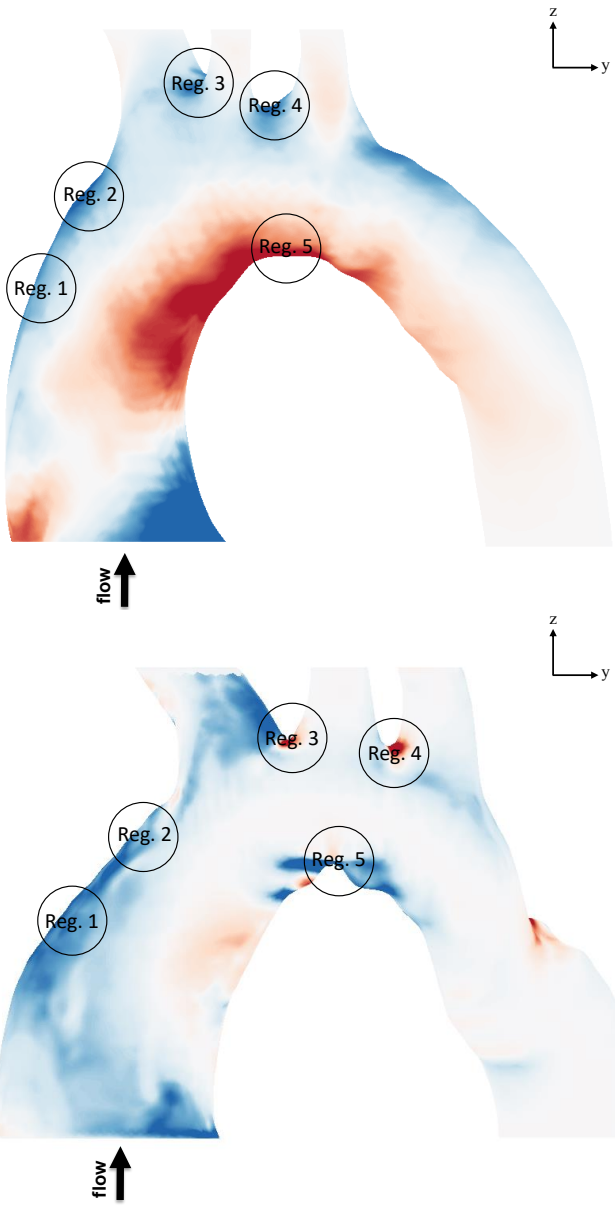

Figure 5.12: Regions of high wall shear stress in both H and UH aorta. Peak wall shear stress for regions labeled are shown in Table 5.1

Table 5.1: The maximum wall shear stress during peak systole at 5 locations as labeled in Figure 5.12.

Simulation	**Reg. 1**	**Reg. 2**	**Reg. 3**	**Reg. 4**	**Reg. 5**
NN	1.3 Pa	1.7 Pa	1.9 Pa	2.0 Pa	2.2 Pa
AA	2.2 Pa	2.7 Pa	3.2 Pa	3.1 Pa	2.9 Pa
NNeu	1.4 Pa	1.9 Pa	1.8 Pa	1.8 Pa	2.0 Pa
AN	3.1 Pa	3.8 Pa	4.4 Pa	4.2 Pa	3.4 Pa
ANeu	2.3 Pa	2.9 Pa	2.9 Pa	2.7 Pa	2.6 Pa

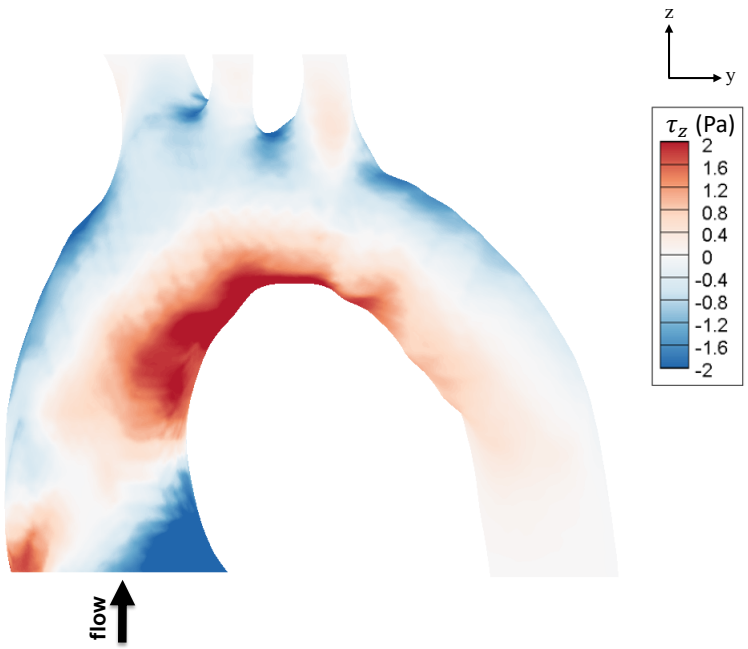

Figure 5.13: WSS contour in NN simulation during peak systole.

occur during peak systole. During diastole, the shear stresses remain fairly low, generally exhibiting maximum magnitudes of less than 1 Pa. In the abnormal aorta, however, wall shear stresses reach peaks of approximately 2 Pa in the regions of interest during diastole. In general, despite showing similar trends for wall shear stress distribution, NNeu and ANeu simulations predicted lower wall shear stresses near the bottom of the aortic arch and in the descending aorta, and higher shear stressed at the first three outlets. These small discrepancies between Dirichlet-base (NN and AA) and Neumann-base (NNeu nad ANeu) simulations can be attributed to the slight discrepancies in relative flow rates through each of the outlets. However, these variations are too small to change our physical interpretation of blood flow in both normal and abnormal aorta models.

The bottom of the aortic arch is a region of high shear stress in both the normal and abnormal models. However, the distribution of stress is greatly affected by the presence of the indentation. In the normal aorta (Figure 5.13), the location of the largest wall shear stress at the bottom of the aortic arch coincides with the peak velocity region near the centre of the aortic arch. The wall shear stress then decreases approximately proportionally with the velocity on either side of this peak region. On the ascending section of the abnormal aortic arch, the wall shear stress is generally in the positive $z-$direction (see Figure 5.14), while the wall shear stress is generally in the negative z-direction in the descending section of the aortic arch. The z-component of wall shear stress dominate the stress field, which is

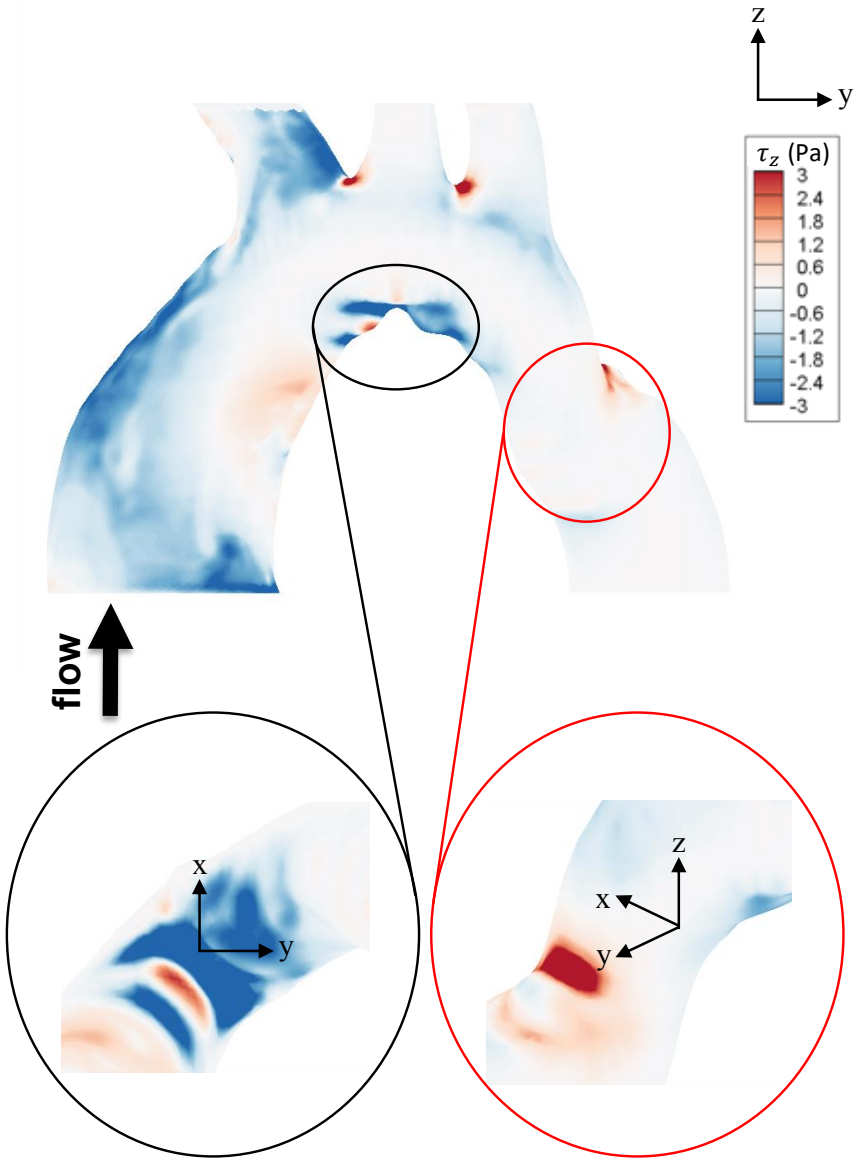

Figure 5.14: WSS contour in AA simulation during peak systole with detailed view of regions of interest.

expected since they correspond to the direction of the primary flow through the main aorta pathway. In the abnormal aorta, the region near the indentation at the bottom of the aortic arch is also a region of high wall shear stress. However, the magnitude of stresses (Figure 5.14) do not decrease as quickly as in the normal aorta (Figure 5.13). The direction of wall shear stresses implies that there exists a recirculatory flow in this region. On the leading edge of the indentation, there is an area of high wall shear stress opposing the direction of the flow, surrounded by two areas of high wall shear stress aligned with the primary flow

direction. The high wall shear stress here is expected, but the wall shear stress opposing the primary flow is another indicator of a recirculation zone on the leading edge of the indentation. Above the center of the indentation, there is a small streak of slightly elevated wall shear stress. This is likely due to the redirecting of blood flow in this region. At the trailing edge of the indentation, there is another region of high wall shear stress that opposes the general direction of the flow. This shear stress further indicates that there is likely a recirculation zone on the trailing edge of the indentation.

The wall shear stress in the descending aorta is generally lower in the abnormal aorta (Figure 5.14) compared to the normal aorta (Figure 5.13) due to a lower velocity. However, the abnormal aorta depicts a region of elevated wall shear stress towards the trailing end of the aorta coarctation in Figure 5.14. In the normal aorta, the wall shear stress in the descending aorta is fairly small since there is no complex geometry impeding the flow. Also, the velocity is lower in this region compared to the ascending aorta (see Figure 5.13). The majority of the abnormal descending aorta experiences very low wall shear stresses (see Figure 5.14), even during systole. This is because the flow is redirected away from the aorta walls, and thus, from the geometrical anomalies, such as the coarctation and aortic arch indentation. However, near the trailing end of the aorta coarctation, at the most narrowed segment of the main aorta pathway, there is a region of highly elevated wall shear stress. The stresses in this region, which is highlighted in Figure 5.14, are far larger than elsewhere in either simulations. This high wall shear stress occurs due to a combination of factors. First, this region has the largest velocity during peak systole in the abnormal model. Second, the faster flow occurs in close proximity to the aorta wall, which inherently increases stress. Third, the complex geometry in this region leads to the flow redirection towards the aorta walls due to the sudden expansion of the aorta directly after the coarctation. The wall shear stress in this region is more than double the average wall shear stress in a normal aorta during peak systole, which increases the risk of rupture. The wall shear stress at this region is even larger in the AN simulation, which is based on the normal aorta boundary conditions from Subject 1. This result suggests that one of the contributing factors for the decreased flow rate through the abnormal aorta may be the alleviation of wall shear stress in this area. By decreasing the velocity of blood through the aorta, the velocity at this region of high wall shear stress will also drop, and it will thereby reduce the maximum wall shear stress experienced in the abnormal aorta. It is also significant to recognize that this peak wall shear stress opposes the direction of the flow in the main aorta pathway, which further hints at a region of flow recirculation.

5.5 Key Flow Disturbances

One of the main purposes of this study was to characterize the key blood flow features in an abnormal aorta model with two major geometrical anomalies. This is followed by addressing potential variations in blood flow characteristics using efficient geometrical resolution techniques, such as using flow manipulators. To this end, a systematic comparison is carried out between blood flow in a normal aorta (NN) and that of an abnormal aorta (AA) using patient-specific boundary conditions to identify blood flow anomalies and interpret their physical implications. Detailed analysis of the velocity field and stress fields revealed that the application of Dirichlet or Neumann boundary conditions at *Outlet 1*, *Outlet 2* and *Outlet 3* did not have any significant effect on the main blood flow pattern in the main aorta pathway or at the regions of interest. The pressure distribution was consistent along the main aorta pathway for both types of boundary conditions with some differences at the beginning of the aortic arch. This discrepancy in pressure is expected to be resolved when using aorta models that are cropped further up along the brachiocephalic, left common carotid, and left subclavian arteries. Using six simulation cases, two key regions of interest are identified in the models. The region around the aortic coarctation was expected to be a region of interest, as it was one of the primary anomalies of the abnormal aorta model. Additionally, the small indentation at the inferior aspect of the aortic arch also produced significantly different flow characteristics compared to the normal aorta.

The results in the aortic coarctation were as expected, resulting in an increase in velocity, a decrease in pressure, and an increased wall shear stress. Although the pressure did recover after the coarctation, there was a pressure drop along the main aorta pathway compared to the normal aorta, which intuitively leads to a lower blood pressure at *Outlet 4*, and thus the lower half of the body. There is also a region of high vorticity shortly after the end of the coarctation, which has the characteristics for an elevated risk of blood clot formation. The presence of wall shear stresses that are generally opposed to the direction of primary flow also suggests that there is recirculation occuring in this region. By comparing the wall shear stresses between the AN and AA simulations, it is probable that one of the primary factors for the decreased blood flow rate through the abnormal aorta was to alleviate some of the stress imposed on the aorta walls at the coarctation. This decreased flow rate could lead to health complications for the patient in conjunction with the lower blood pressure through the descending aorta since it will decrease the blood circulation to the lower body. The constantly elevated stress imposed on the coarctation walls may also lead to an increased

rigidity in the nearby region, which increases the risk of medical complications during traditional treatments.

The deformity found at the bottom of the abnormal aortic arch also had significant effects on local flow characteristics, and exhibited a higher pressure and wall shear stress. This anomaly also impedes flow traveling through the main aorta pathway, and likely contributes to the increased flow rate through the first three outlets in the abnormal aorta. There is a significant increase in vorticity in the surrounding area, particularly towards the latter half of the aortic arch. These regions of lower velocity and higher vorticity increases the possibility of stagnation flow, which is the ingredient for the formation of blood clots. This would further impede the flow through the aorta. The wall shear stress opposing the direction of primary flow on the trailing edge of the indentation suggests that the flow has recirculatory characteristics. This part of the aorta wall also represents a region that is difficult to alter using current surgical interventions, as the aortic arch is a region with complex geometry due to the presence of the first three outlets. If the abnormal flow characteristics in this region are manipulated without the need for geometrical modifications by lowering the relative flow through the first three outlets, it can help alleviate the elevated blood pressure in the upper body and correct the low blood pressure in the lower body. Implementation of small vortex generators at the leading and trailing edge of the indentation provides a possible method in redirecting the flow towards the beginning of the descending aorta.

5.6 Summary

Two patient-specific models representing a normal and an abnormal aorta were used with varying patient-specific boundary conditions to characterize the blood flow in the presence of the indentation anomaly and the arota coarctation. Six simulations were carried out for the two cases under different conditions, which identified the significant flow interruptions due to the aortic coarctation and the indentation at the bottom of the aortic arch. Both regions showed a local decrease in velocity, and a local increase in wall shear stress, vorticity, and pressure. The lower velocity combined with higher vorticity formed regions with a higher risk of blood clot formation, which can also lead to further drop in blood flow rate and interruption of blood delivery to the lower body. The wall shear stresses opposing the primary flow direction in these regions also hints at the presence of flow recirculation. The abnormal aorta also exhibited a higher relative flow rate through the first three outlets of the aortic arch, resulting in a lower flow rate through the fourth outlet. This result would

indicate a decreased blood pressure in the lower body, and an increased blood pressure in the upper body.

The blood flow rate was lower in the abnormal aorta, which is believed to help alleviate the elevated wall shear stresses found in the coarctation and aortic arch indentation. This is based on the comparison of the blood flow in the abnormal aorta using the normal patient-specific boundary conditions. The lower flow rate further exasperates the low blood pressure that is expected in the lower body of the abnormal patient.

—

Chapter 6

Flow Manipulation [3]

6.1 Introduction

The region near the aortic arch and coaractation of the abnormal aorta show undesirable flow characteristics, with recirculation regions, areas with pressure drop and high velocity and large wall shear stresses. One possible method to counteract these abnormal flow characteristics is to implement flow manipulators, which are known to alter the flow significantly with no damage to the walls or alternations to the geometrical shape of the aorta.

6.2 Flow Manipulator

Two manipulators are suggested to redirect the flow, one prior to each region of interest. The flow manipulators divert the flow of high velocity away from where it is undesirable. By diverting the flow upwards and to the sides, the high velocity stream is separated, and it reduces the probability of a recirculation zone or the generation of regions of high wall shear stress downstream. The addition of flow manipulators should also be a simple process similar in nature to the current treatment methods of balloon angioplasty. The flow manipulators, made of non-reactive material, can be inserted through the rectum, and wired throughout the arteries to the corresponding location in the aorta using different imaging techniques. The details on how such implementations are performed is outside the scope of the current study. Here, the focus is only on understanding the effects of flow manipulators on improving the quality of blood flow. In general, the small size of flow manipulators greatly limit any potential damage to the aorta wall in the form of reduced elasticity. These effects are confined to a very small region compared to the current treatment methods, such as

[3]The results in this chapter are part of a publication currently under review in the Journal of Applied Mechanics: Jia, Y., Punithakumar, K., Noga, M., Hemmati, A. (2020) Blood flow manipulation in the aorta with coarctation and arch narrowing for pediatric subjects. *J. of Applied Mechanics.*

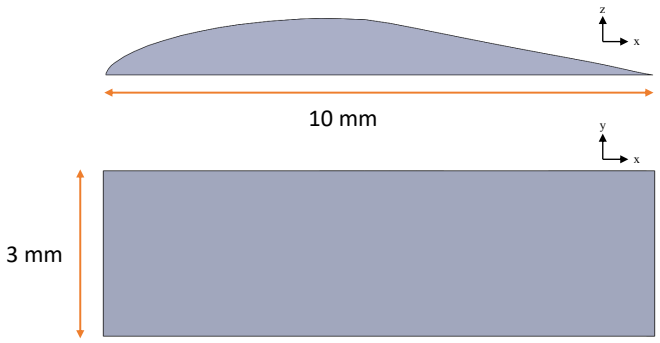

Figure 6.1: Chord length and width of flow manipulators. Fin geometry identical to top half of NREL S809 airfoil.

implementation of stents. This study constitutes a proof-of-concept for the implementation of flow manipulators to correct abnormal blood flow through a geometrically imperfect aorta in pediatric subjects.

Flow manipulator geometry was selected following the work of Somers, 2003, since the selected device generates desirable flow characteristics needed for countering the abnormal flow characteristics observed here. The schematics of the manipulator is shown in Figure 6.1. The placement of flow manipulators followed closely the results of AA and AN simulations to best redirect blood flow in regions of interest at the aortic arch and coarctation. This followed several test trials to identify a potentially desirable location. Simulation AFM in Table 3.1 represents the case of normal blood flow through an abnormal aorta model with flow manipulators. The exact geometrical scale of the flow manipulator is identical to the top half of the NREL S809 airfoil, and the full geometry can be determined by using the displayed chord length. Micro-vortex generators can be found along the leading edge of the flow manipulators in order to reduce flow sepearation and vortex generation along the trailing edge. The mesh used on and around the flow manipulators is particularly fine in order to properly resolve wall shear stressed along the edges.

The flow manipulators were placed at $l_{FM} = 0.1D$, $0.2D$ and $0.5D$ prior to the aortic arch and $0.5D$ prior to the coarctation, shown in Figure 6.2. Several flow manipulator geometries were tested in various locations in the aorta, but their implementation showed less desirable results than the flow manipulators implemented in the current set-up. Here, only the physically and medically relevant results are presented that correspond to the most influential placement of the manipulators. This simulation corresponds to AFM in Table 3.1.

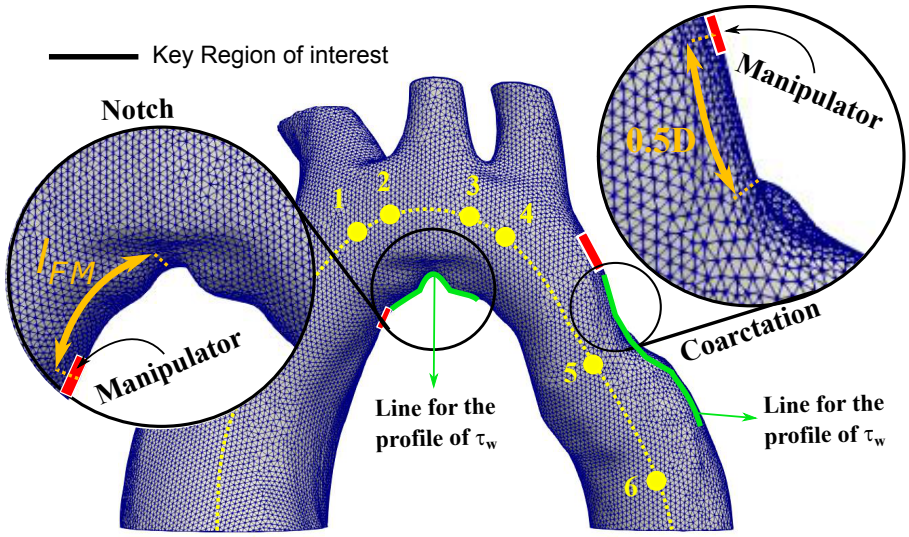

Figure 6.2: Locations of flow manipulator placements relative to key regions of interest. Here, l_{FM} is the distance of flow manipulator from the region of interest, which varies between $0.1D$ to $0.5D$. Locations 1−6 refers to $d^* = 2.5, 2.8, 3.2, 4.0, 4.2$, and 5.5.

6.3 Flow Recovery

The addition of the flow manipulator at $l_{FM} = 0.5D$ prior to the indentation and another one at $0.5D$ prior to the coarctation led to predominantly desirable flow characteristics, such as smaller regions of high velocity near the aorta walls (Figure 6.3), lower pressure drop through the coarctation (Figure 6.5), and smaller peak wall shear stresses in the regions of interest (Figure 6.6). The recirculation areas have also been largely reduced in size both at the aortic arch and the aorta coarctation (Figure 6.4). Moreover, velocity and wall shear stresses in the descending aorta show great recovery towards normal flow conditions. However, the wall shear stress on the flow manipulators themselves are relatively high, by virtue of their design that involves using geometrical obstacles to separate high velocity flow. This elevated wall shear stress is not expected to cause medical difficulties, especially since the flow manipulators can be manufactured using material with high fatigue strength that eliminate the risk of failure. At the aorta walls, where the medical implications are more critical, the peak wall shear stress has dropped significantly in the regions of interest in both the aortic arch (by 20%) and the coarctation (by 70%). The wall shear stress in the descending aorta is also consistent with the wall shear stress in the normal aorta, showing the recovery of recirculation zones in the coarctation. As the elevated wall shear stress acting on the aorta walls is believed to be the primary explanation for the decreased flow

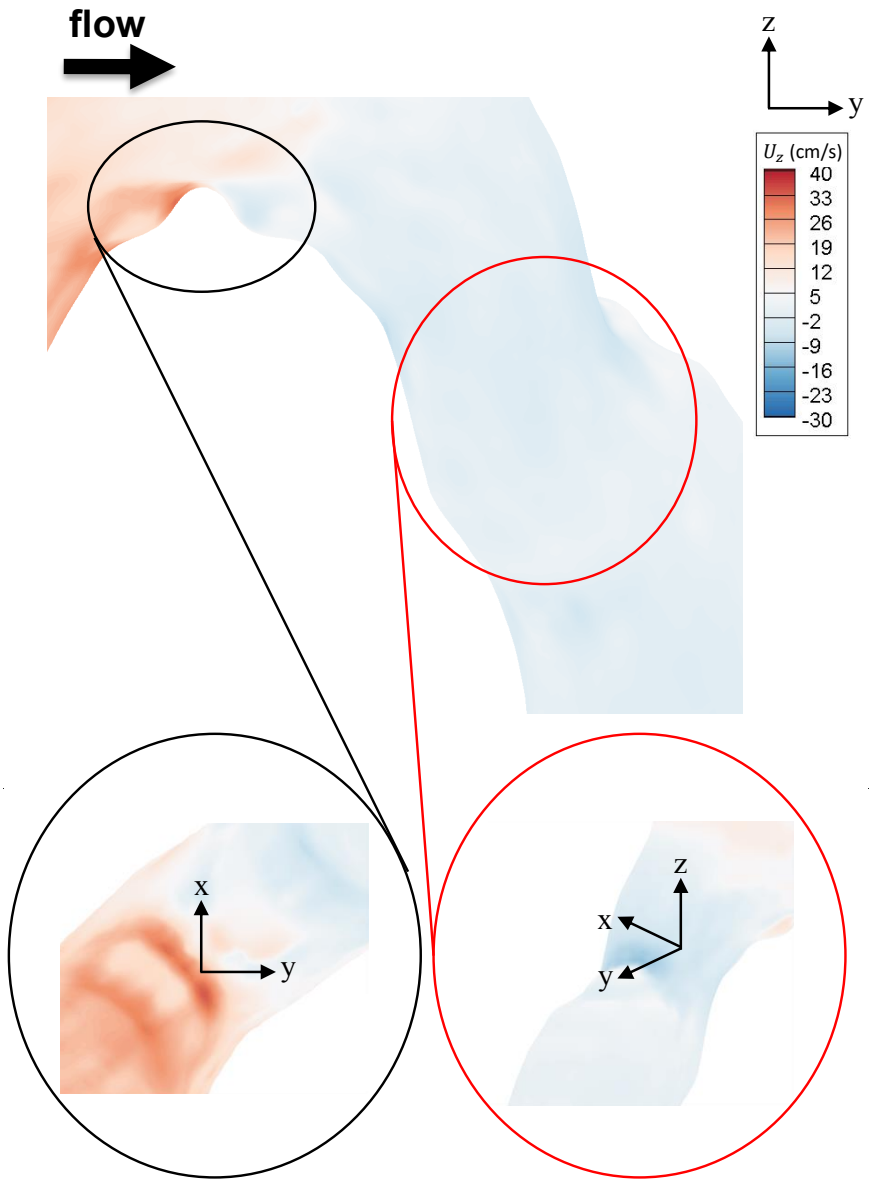

Figure 6.3: Contour of velocity at regions of interest after flow manipulator installation at $l_{FM} = 0.5D$.

rate through the abnormal aorta, the alleviation of this stress is expected to reduce the risk that may have been associated with an increase in flow rate in abnormal patients, such as rupture due to large stresses at higher flow rates. A return towards normal flow rates will help mitigate the decreased blood pressure in the lower body of the patient, and represents the resolution of one of the primary complications of these diseases.

Using the flow manipulator positioned $l_{FM} = 0.5D$ from the regions of interest shows flow correction towards normal blood flow characteristics that is much more predominant

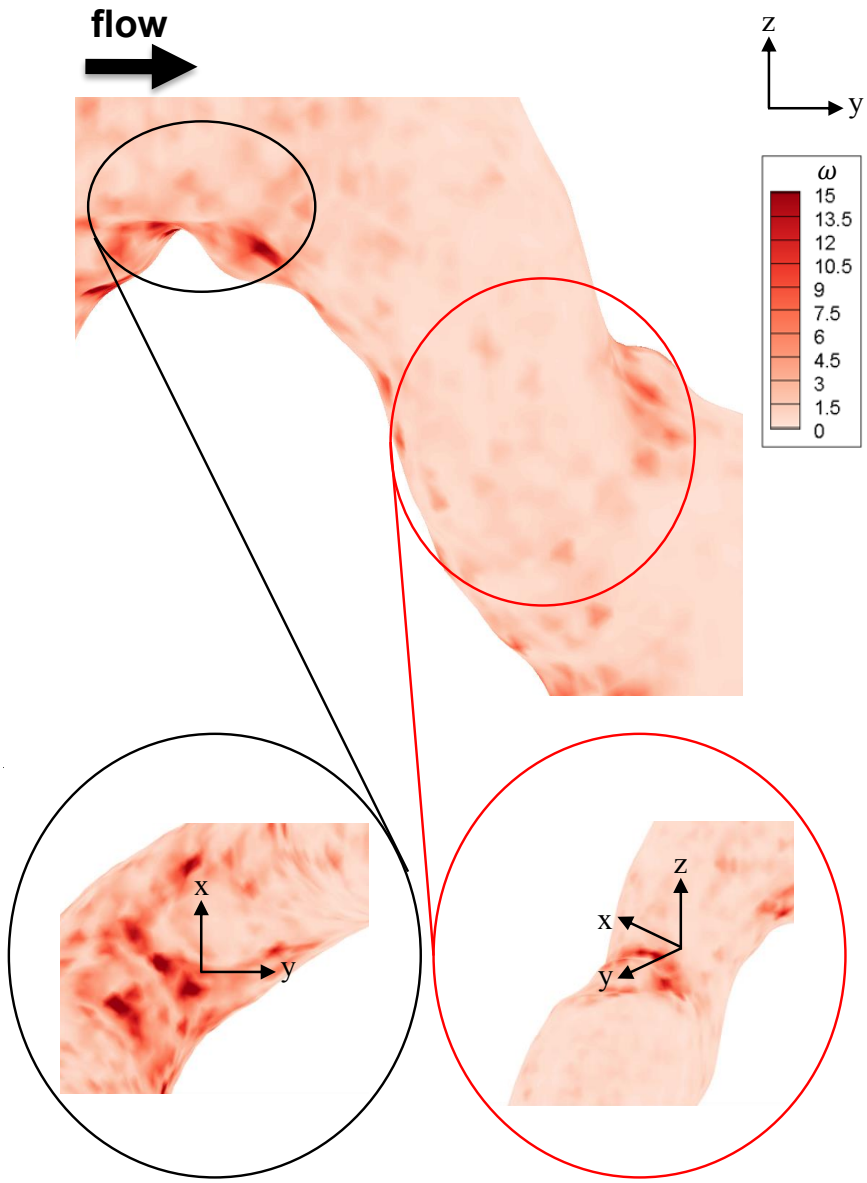

Figure 6.4: Contour of vorticity at regions of interest after flow manipulator installation at $l_{FM} = 0.5D$.

in the coarctation than the aortic arch. By moving the flow manipulator in the aortic arch closer to the indentation ($l_{FM} \approx 0.2D$), the abnormal flow characteristics in the aortic arch are much better alleviated. The velocity in Figures 6.7, 6.11 and 6.12 has decreased in the regions of peak magnitude, while the regions of high vorticity (see Figure 6.8) have decreased in size, particularly near the inferior aspect of the mid aortic arch. The most significant effect is observed with pressure in Figures 6.9, 6.14 and 6.14 and wall shear stresses in Figure 6.10, 6.16 and 6.17. Due to the lowered velocity in key areas in the aorta, the pressure drop

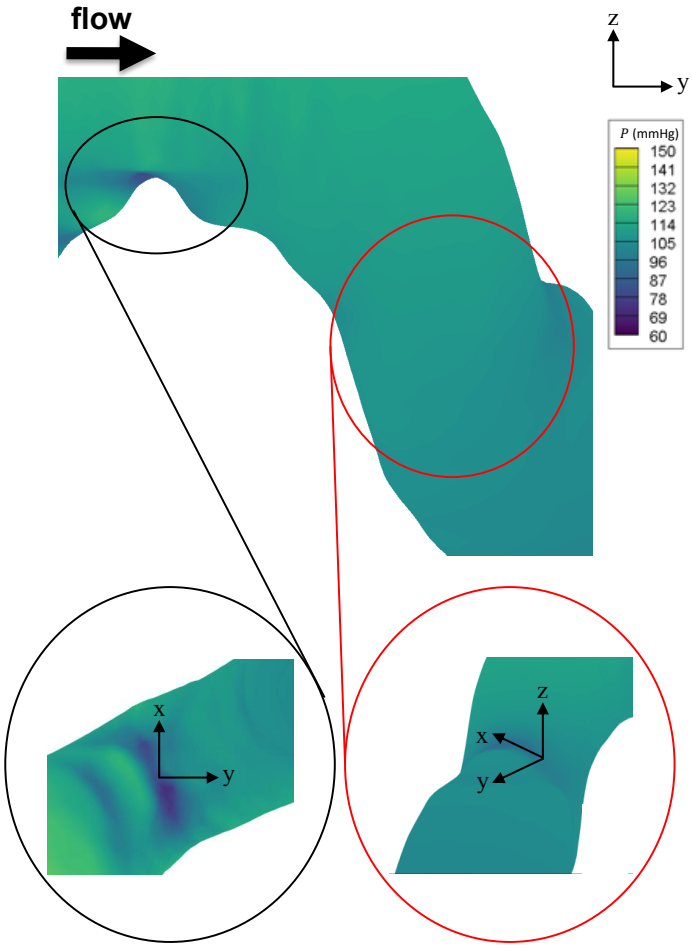

Figure 6.5: Contour of pressure at regions of interest after flow manipulator installation at $l_{FM} = 0.5D$.

has been alleviated significantly, such that the pressure drop on the trailing edge of the aortic arch is negligible. The wall shear stress continues to exhibit a region of relatively high stress coinciding with the regions of high velocity. However, the region of wall shear stress opposing the primary flow direction appears to be suppressed, which signifies the correction of the recirculation zone on the leading edge of the aortic arch. The regions past the aortic arch are not effected significantly by the movement of the flow manipulator, and the coarctation still shows considerable improvement with a flow manipulator installed father away at $l_{FM} = 0.5D$. The positive effect of the flow manipulation diminishes as the manipulation devices are moved closer to the anomalies, i.e., $l_{FM} = 0.1D$. The profile of wall shear stress for the flow manipulator setups are shown in Figure 6.16. All three setups greatly change the abnormal wall shear stress characteristics near the indentation, but the contour results (see Figures 6.6 and 6.10) show that moving the manipulator to

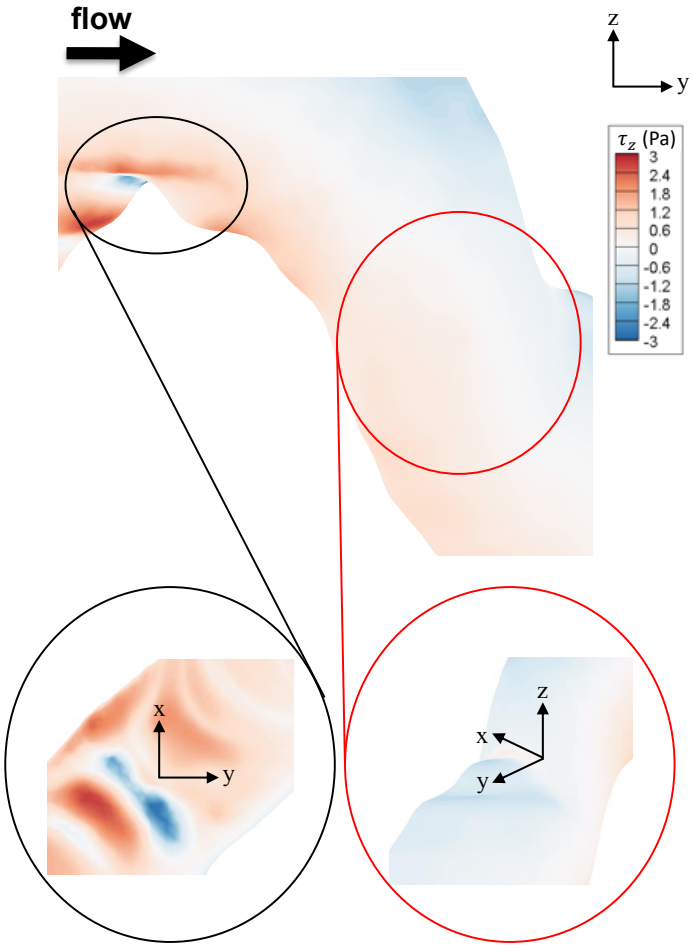

Figure 6.6: Contour of wall shear stress at regions of interest after flow manipulator installation at $l_{FM} = 0.5D$.

$l_{FM} = 0.2D$ can alleviate the reverse flow that is experienced at the leading edge of the indentation. However, moving the flow manipulator to $l_{FM} = 0.1D$ and $0.5D$, reduces the effectiveness of desirable effects. This is consistent for pressure (Figure 6.14) and shear stresses (Figure 6.16). In case of the coarctation, the pressure profiles (Figure 6.14) show great recovery towards the normal aorta values with the installation of flow manipulators. The velocity of blood, however, has not returned to the trends expected for a normal aorta (Figure 6.12). Nevertheless, the recovery of wall shear stress and pressure has the potential to accommodate normal blood flow rates. The pressure and wall shear stress results in Figures 6.14–6.17 suggest that the flow manipulator at $l_{FM} = 0.2D$ has succeeded in resolving the recirculation zones near the aortic arch indentation.

The favorable results obtained using these preliminary cases of implementing flow manipulators show that the proposed technique is, in general, medically viable in correcting

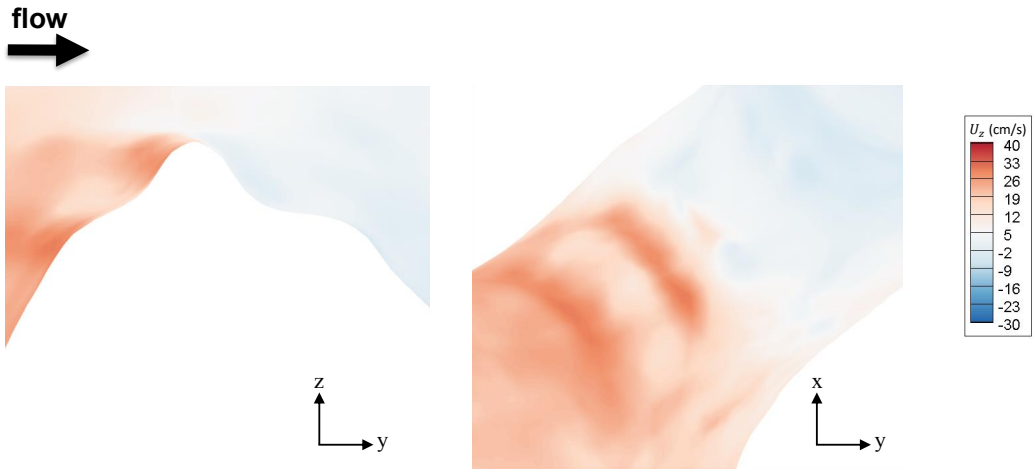

Figure 6.7: Contour of velocity at regions of interest after flow manipulator installation at $l_{FM} = 0.2D$.

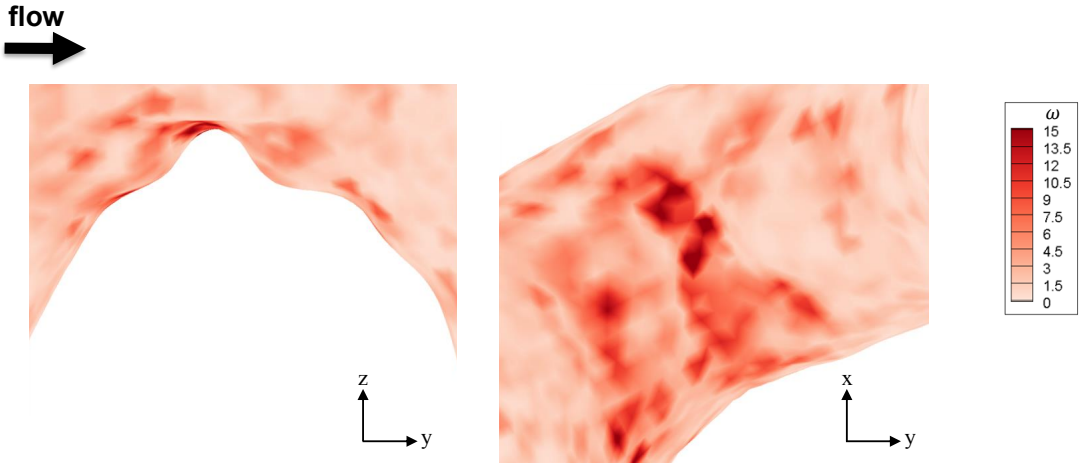

Figure 6.8: Contour of vorticity at regions of interest after flow manipulator installation at $l_{FM} = 0.2D$.

the undesirable blood flow characteristics. Our results act as a proof-of-concept on a new potential treatment strategy. A more detailed analysis into the orientation, geometry and location of the flow manipulator implementation will further improve the results obtained in this manuscript. These factors are expected to be dependent on the patient-specific flow characteristics, and optimal treatment templates are expected to vary amongst patients. Using patient-specific flow manipulator installations should be particularly viable in cases of aortic arch narrowing since they are currently considered a variant anomaly, and comprehensive treatment solutions are not well established. The proposed treatment is potentially

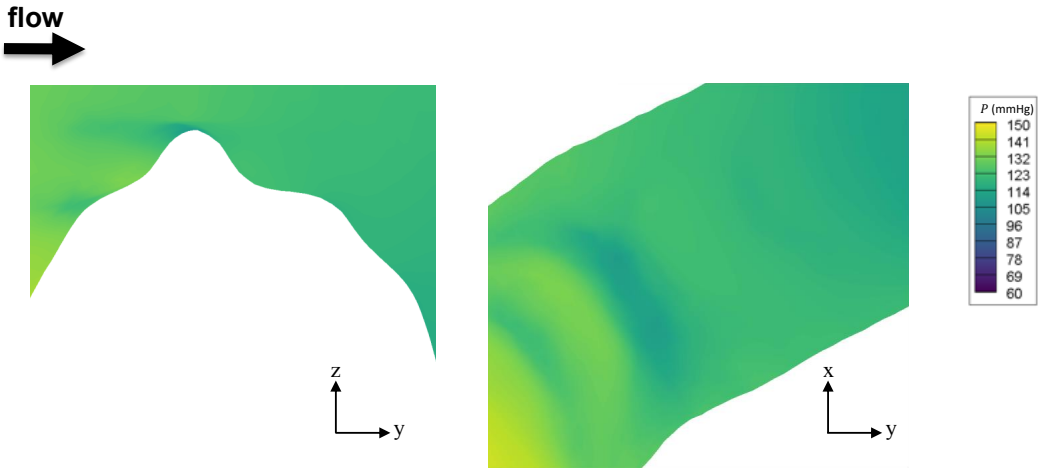

Figure 6.9: Contour of pressure at regions of interest after flow manipulator installation at $l_{FM} = 0.2D$.

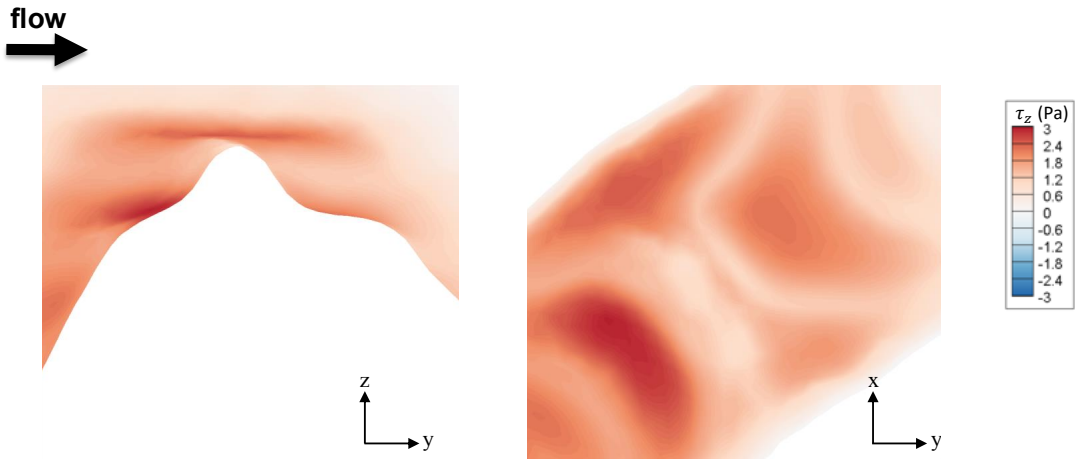

Figure 6.10: Contour of wall shear stress at regions of interest after flow manipulator installation at $l_{FM} = 0.2D$.

more affordable and it results in less complications compared to existing treatments. Non-reactive material with an adequate fatigue strength greater than 4 Pa, based on the current range of shear stresses, is relatively affordable (Bowen *et al.*, 2016). Thus, the majority of the costs is expected to be focused on manufacturing patient-specific flow manipulators, and the procedure for their implementation, i.e., balloon angioplasty. Furthermore, future complications associated with conventional treatment methods may be diverted by using patient-specific flow manipulator implementation based on simulations similar to the ones performed here.

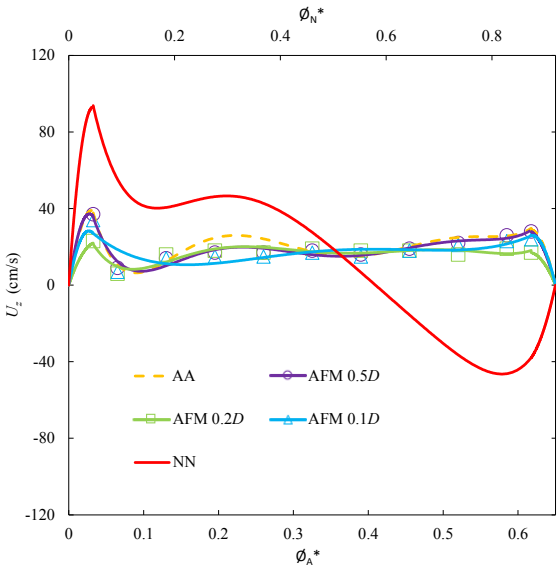

Figure 6.11: Velocity profile at location 2 with three ($l_{FM} = 0.1D, 0.2D, 0.5D$) flow manipulator setups. Diameter $\varnothing^*$ is measured radially from the edge proximal to the aortic arch outwards along a constant d^*, and normalized by D. $\varnothing_A{}^*$ corresponds to the abnormal aorta and $\varnothing_N{}^*$ corresponds to the normal aorta.

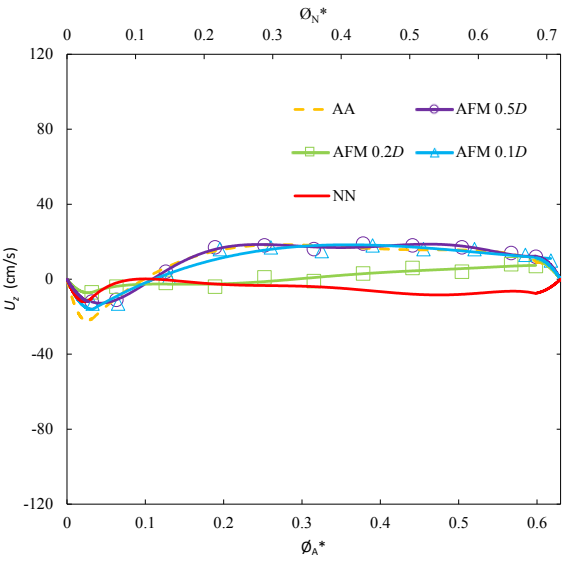

Figure 6.12: Velocity profile at location 3 with three ($l_{FM} = 0.1D, 0.2D, 0.5D$) flow manipulator setups.

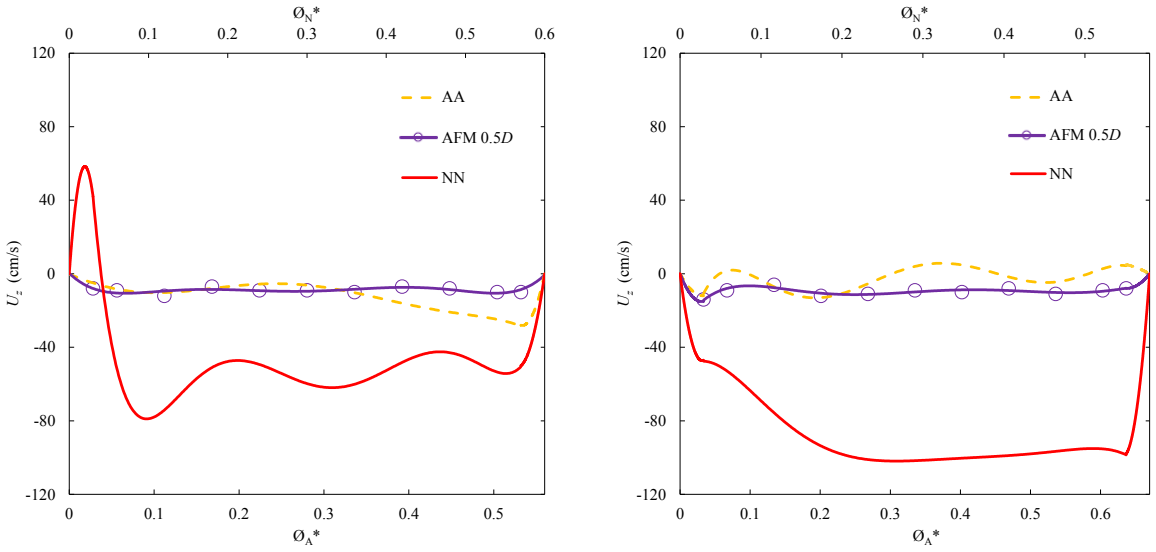

Figure 6.13: Velocity profile at locations 5 (a) and 6 (b) after flow manipulator installation at distance $0.5D$.

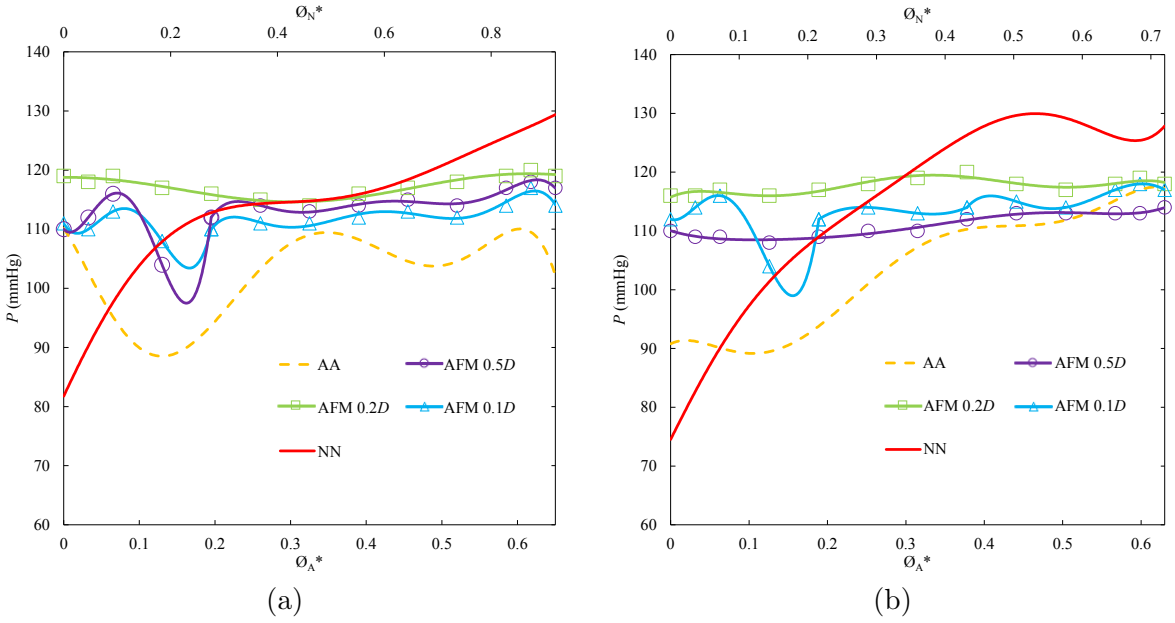

Figure 6.14: Pressure profile at location 2 (a) and 3(b) with three ($l_{FM} = 0.1D, 0.2D, 0.5D$) flow manipulator setups.

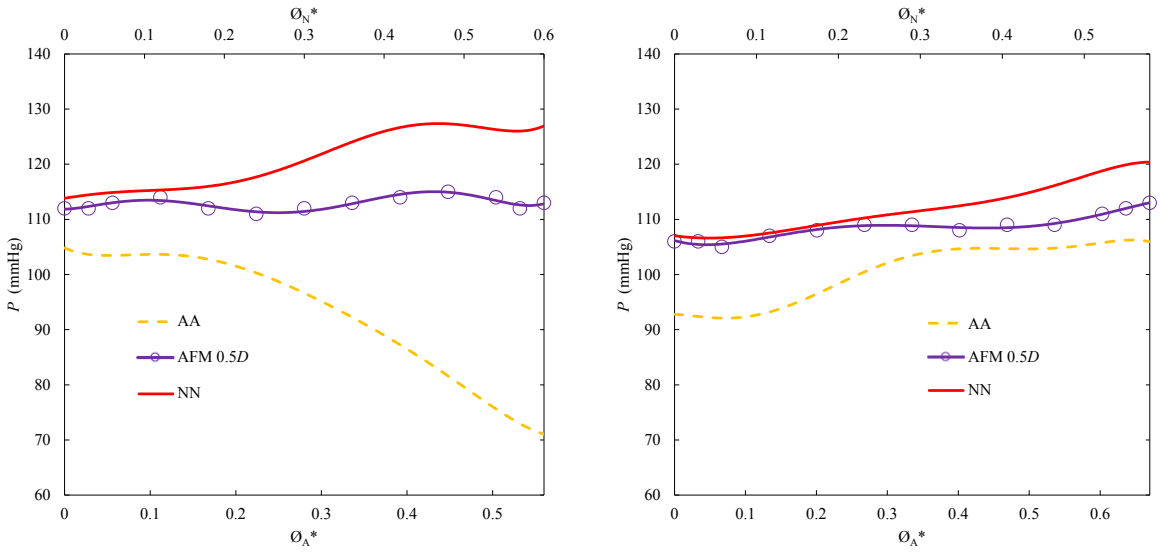

Figure 6.15: Pressure profile at location 5 (a) and 6 (b) after flow manipulator installation at distance $0.5D$.

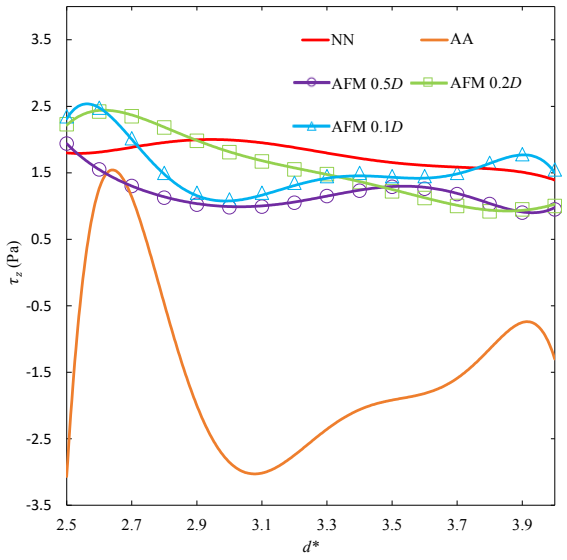

Figure 6.16: Wall shear stress near aortic arch indentation with three ($l_{FM} = 0.1D, 0.2D, 0.5D$) flow manipulator setups.

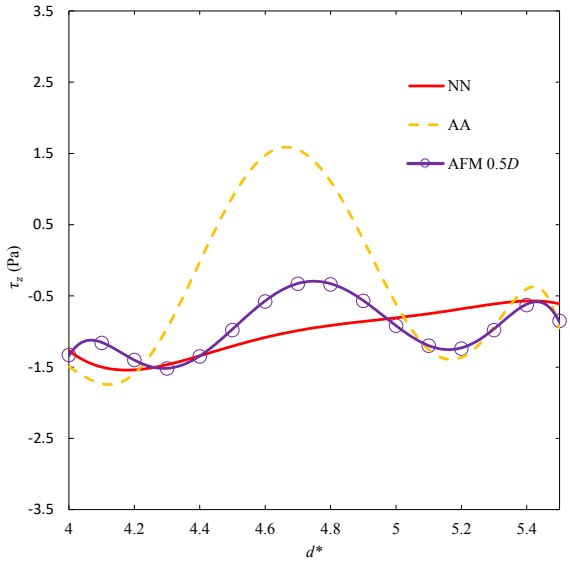

Figure 6.17: Wall shear stress near aortic coarctation after flow manipulator installation at distance $0.5D$.

6.4 Summary

The flow disturbances identified in Chapter 5 hint at the need to restore normal blood flow in the presence of the indentation and aorta coarctation. The aortic coarctation is expected to be the easier deformity to correct since it is not an uncommon disease in the aorta. Many surgical and non-surgical solutions already exist to treat this medical disorder, despite their shortcomings and potential complications. The indentation at the bottom of the aortic arch is a more difficult abnormality to address since the aortic arch is a region with a complex geometry. Here, a new guide is proposed for an efficient resolution technique to change the flow using flow manipulators at the bottom of the aortic arch and prior to the aorta coarctation. With the implementation of two flow manipulators prior to the regions of interest, the peak wall shear stress in the abnormal aorta is decreased considerably (up to 70%) and the recirculation zones are reduced in size. Although further optimization analysis is necessary to obtain a more effective patient-specific flow correction approach, initial simulations show a promising resolution towards normal flow characteristics using this new technique. Thus, this study provides evidence showing the feasibility and proof-of-concept of using flow manipulators to improve blood flow in the presence of geometrical anomalies.

Chapter 7

Conclusion

The results presented in this thesis outlined key flow disturbances in terms of velocity, pressure, vorticity, and wall shear stress due to coarctation of the aorta and narrowing of the aortic arch in pediatric subjects. These results enabled a feasibility study on an initial procedure for the resolution of abnormal flow characteristics in key regions of the flow.

Using the normal aorta model with NN and NFR boundary conditions, key flow discrepancies were identified between using velocity boundary conditions in combination with either pressure or flow rate outlet boundary conditions. Ultimately, both simulations showed similar key trends in velocity and pressure, and discrepancy was largely negligible ($< 5\%$) in the main aorta pathway. The numerical results were then compared with patient-specific experimental measurements, and showed great accuracy with an error less than 5%. These results signified the ability to proceed to the abnormal aorta model using a combination of patient-specific velocity and pressure boundary conditions.

Six simulation setups with varying boundary conditions were used to compare between normal and abnormal aorta flow characteristics. The abnormal aorta showed large discrepancies in velocity, vorticity, pressure and wall shear stress in the coarctation and in the area proximal to the inferior aspect of the mid aortic arch. These regions showed abnormal velocity distribution, high vorticity, large pressure drops, and wall shear stress opposing the primary direction of flow that suggested the presence of recirculation zones. A large pressure drop through the coarctation and decrease in blood flow rate also indicate the potential for low blood pressure in the lower body of the patient. Both of these characteristics are undesirable. Thus, two flow manipulators were implemented into the model geometry to help alleviate some abnormal flow characteristics.

After testing numerous flow manipulator implementations, flow manipulator installation locations at $0.2D$ away from the aortic arch indentation and $0.5D$ away from the start of the

coarctation were selected. The incorporation of the flow manipulator showed great recovery of the abnormal flow characteristics towards normal blood flow observed in the normal aorta model, particularly for pressure and wall shear stress distributions. The combination of velocity, vorticity, pressure, and wall shear stress contours suggest that there is a recovery of recirculation zones near the indentation and coarctation. Wall shear stress is also greatly alleviated in regions of high intensity originally found near the indentation and coarctation. This decrease in wall shear stress may allow for a greater flow rate through the aorta, which would likely help resolve other undesirable and abnormal flow characteristics. The results provide a proof-of-concept for the implementation of flow manipulators to alleviate undesirable flow patterns instead of surgical reconstruction of the aorta geometry.

7.1 Contribution to the Field

The comparison between pressure and flow rate boundary conditions showed very low discrepancy, and suggests that the two boundary conditions are interchangeable for studies focused on the main aorta pathway. This contribution ensures accurate simulation results may be obtained regardless of the capacity to measure pressure or flow rate data. This is a major contribution to the field of cardiovascular flow modeling since it provides a benchmark data on importance and implications of different boundary conditions.

The utilization of flow manipulators to correct abnormal flow in the aorta showed desirable results, and it suggest that this treatment option is valid as an alternative to aorta reconstruction surgery. This possibility is an asset to the medical field, as surgical procedures currently used for aorta reconstruction are complex, expensive, and have high risk of complication. By creating patient-specific templates for flow manipulator installations, surgical complexity is expected to decrease, while risk of complication should decrease significantly. This proof-of-concept facilitates further study of this method in diverting and controlling blood flow in arteries.

7.2 Directions for Future Work

The results obtained from this work are not yet suitable for use in industry on human or animal patients. The most logical next steps include: (1) optimizing the geometry of the manipulators towards more effective diversion of the blood flow, (2) optimizing the placement of manipulator devices for best possible outcome, (3) extended case studies based on various designs and patient data in preparation for pre-clinical trials, and (4) pre-clinical

trials on animals.

The work that has currently been done shows promising results. However, the preliminary results must be first optimized, and potential complications or side effects should be identified. Ultimately, the goal of the overarching project scope aims to produce clinically and industrial relevant alternative treatment techniques, but there remains significant work to be conducted both numerically and clinically.

First, flow manipulator setups can likely be modified to improve the recovery seen in abnormal flow characteristics. As the two anomalies seen in the coarctation and near the indentation are not identical, it is likely that an optimal flow manipulator setup for the two anomalies would be of different geometry. After exploring desirable flow manipulator geometries in greater detail, there remains to be benefit in testing different setup locations for the flow manipulators to understand how different installation setups will affect flow recovery. Knowledge of desirable material for flow manipulator usage would also be required if clinical trials were to be conducted at a future date.

Second, using patient-specific boundary conditions would be important in improving the accuracy of simulations. In these simulations, velocity data was captured both spatially and periodically. However, pressure measurements only consisted of a systolic and diastolic magnitude. Having both the spatial and temporal measurements for the patient-specific pressure boundary conditions is expected to increase the accuracy of numerical results to better reflect physical conditions. Additionally, fluid and solid simulation parameters are obtained from previous literature, and there exists the possibility of large discrepancies from the norm in abnormal patients.

If using Neumann boundary conditions at *Outlet 1*, *Outlet 2*, and *Outlet 3* are desired, the fluid and solid domain should be cropped further along the branchiocephaic, left common carotid, and left subclavian arteries. This will allow the flow more time to develop at each outlet, and Neumann boundary condition results should align more consistently with Dirichlet boundary condition results.

Prior to clinical animal studies, there needs to be far greater consideration of the installation process for the flow manipulators. In order to use flow manipulators to become practical, they need to be both less complex and result in fewer complications than traditional surgical interventions. This requires a detailed parametric study involving engineering and clinical aspect of such implementation of the proposed flow manipulation.

Bibliography

[1] Al-Manthari and S. Maimouna. *Numerical simulation of selected two-dimensional and three-dimensional fluid-structure interaction problems using OpenFOAM technology.* PhD Thesis, Swansea University, Swansea, Wales, July 2018.

[2] J. Alastruey, N. Xiao, H. Fok, T. Schaeffter, and C. Figueroa. On the impact of modelling assumptions in multi-scale, subject-specific models of aortic hemodynamics. *Journal of the Royal Society Interface*, 13(119):1–17, June 2016.

[3] M. Armstrong, J. Horner, M. Clark, M. Deegan, T. Hill, C. Keith, and L. Mooradian. Evaluating rheological models for human blood using steady state, transient, and oscillatory shear predictions. *Rheologica Acta*, 57(3):705–728, September 2018.

[4] A. Benim, A. Nahavandi, A. Assmann, D. Schubert, P. Feindt, and S. Suh. Simulation of blood flow in human aorta with emphasis on outlet boundary conditions. *Applied Mathematical Modeling*, 35(7):3175–3188, July 2011.

[5] E. Benjamin, P. Muntner, and et al A. Alonso. Heart disease and stroke statistics-2019 update: A report from the american heart association. *Circulation*, 139(1):e56–e528, January 2019.

[6] P. Boutouyrie, S. Boumaza, P. Challande, P. Lacolley, and S. Laurent. Smooth muscle tone and arterial wall viscosity. *Hypertension*, 32(2):360–364, August 1998.

[7] P. Bowen, E. Shearier, S. Zhao, R. Guillory, F. Zhao, J. Goldman, and J. Drelich. Biodegradeable metals for cardiovascular stents: from clinical concerns to recent zn-alloys. *Advanced Healthcare Materials*, 5(10):1121–1140, April 2016.

[8] J. Cheatham. Stenting of coarctation of the aorta. *Catheterization & Cardiovascular Interventions*, 54(1):112–125, September 2001.

[9] M. Cohen, V. Fuster, P. Steele, D. Driscoll, and D. McGoon. Coarctation of the aorta. long-term follow-up after surgical correction. *Circulation*, 80(4):840–845, October 2019.

[10] R. Courant, K. Friedrichs, and H. Lewy. On the partial difference equations of mathematical physics. *IBM Journal of Research and Development*, 11(2):215–234, March 1967.

[11] P. Crosetto, P. Reyond, S. Deparis, D. Kontaxakis, N. Stergiopulos, and A. Quarteroni. Fluid-structure interaction simulation of aortic blood flow. *Computers & Fluids*, 43(1):46–57, April 2011.

[12] D. Somers. *Design and Experimental Results for the S809 Airfoil.* National Renewable Energy Laboratory, Golden, latest edition, 2003. See also URL `https://www.nrel.gov/docs/legosti/old/6918.pdf`.

[13] A. Danpinid, J. Luo, J. Vappou, P. Terdtoon, and E. Konofagou. In vivo characterization of the aortic wall stress-strain relationship. *Ultrasonics*, 50(7):654–665, June 2010.

[14] S. Doost, L. Zhong, B. Su, and Y. Morsi. The numerical analysis of non-newtonian blood flow in human-specific left ventricle. *Computer Methods and Programs in Biomedicine*, 127(1):232–247, April 2016.

[15] S. Ershkov. On existence of general solution of the navier-stokes equtaions for 3d non-stationary incompressible flow. *International Journal of Fluid Mechanics Research*, 42(3):206–213, May 2015.

[16] S. Fleming, M. Thompson, and R. Stevens et al. Normal ranges of heart rate and respiratory rate in children from birth to 18 years of age: a systematic review of observational studies. *The Lancet*, 377(9970):19–25, March 2011.

[17] D. Fyler, L. Buckley, and W. Hellenbrand et al. Report of the new england regional infant cardiac program. *Pediatrics*, 65(2):432–436, February 1980.

[18] D. Gallo, G. Santis, and D. Tresolid et al. On the use of in vivo measured flow rates as boundary conditions for image-based hemodynamic models of the human aorta: Implications for indicators of abnormal flow. *Annals of Biomedical Engineering*, 4(3):729–741, March 2012.

[19] F. Gao, Z. Guo, and M. Sakamoto. Fluid-structure interaction within a layered aortic arch model. *Journal of Biological Physics*, 32(1):435–454, December 2006.

[20] R. Gross. Coarctation of the aorta. *Circulation*, 7(1):757–768, May 1953.

[21] H. Ha, M. Ziegler, and M. Welander et al. Age-related vascular changes affect turbulence in aortic blood flow. *Frontiersr in Physiology*, 9(36):N/A, January 2018.

[22] T. Holzmann. *Mathematics, Numerics, Derivations and openFOAM*. Holzmann CFD, Augsburg, Germany, 2020.

[23] R. Isnard, B. Pannier, S. Laurent, G. London, B. Diebold, and M. Safar. Pulsatile diameter and elastic modulus of the aortic arch in essential hypertension: a noninvasive study. *Journal of the American College of Cardiology*, 13(2):399–405, February 1989.

[24] B. Johnston, P. Johnston, S. Corney, and D. Kilpatrick. Non-newtonian blood flow in human right coronary arteries: transient simulations. *Journal of Biomechanics*, 39(11):1116–1128, November 2006.

[25] B. Johnston, P. Johnston, and D. Kilpatrick. Non-newtonian blood flow in human coronary arteries: steady state simulations. *Journal of Biomechanics*, 37(5):709–720, May 2004.

[26] I. Karsaj and J. Humphrey. A multilayered wall model of arterial growth and remodeling. *Mechanics of Materials*, 44(1):110–119, January 2012.

[27] S. Kelly and M. O'Rourke. Fluid, solid and fluid-structure interaction simulations on patient-based abdominal aortic anuerysm models. *PubMed*, 226(4):288–304, February 2012.

[28] Z. Keshavarz-Motamed, J. Garcia, and E. Gaillard et al. Effet of coarctation of the aorta and bicuspid aortic valve on flow dynamics and turbulence in the aorta using particle image velocimetry. *Experiments in Fluids*, 55(3):1–16, March 2014.

[29] T. Khamdaeng, J. Luo, J. Vappou, P. Terdtoon, and E. Konofagou. Arterial stiffness indentification of the human carotid artery using the stress-strain relationship in vivo. *Ultrasonics*, 52(3):402–411, March 2012.

[30] M. Khan, D. Steinman, and K. Valen-Sendstad. Non-newtonian versus numerical rheology: Practical impact of shear-thinning on the prediction of stable and unstable flows in intracranial anuerysms. *International Journal for Numerical Methods in Biomedical Engineering*, 33(7):e2836, July 2017.

[31] H. Kim, I. Vignon-Clementel, C. Figueroa, J. LaDisa, K. Jansen, J. Feinstein, and C. Taylor. On coupling a lumped parameter heart model and a three-dimensional finite element aorta model. *Annals of Biomedical Engineering*, 37(11):2153–2169, November 2009.

[32] R. Klein, E. Ametepe, Y. Yam, G. Dwivdei, and B. Chow. Cardiac ct assessment of left ventricular mass in mid-diastasis and its prognostic value. *European Heart Journal - Cardiovascular Imaging*, 18(1):95–102, January 2017.

[33] J. Lantz, J. Renner, and M. Karlsson. Wall shear stress in a subject specific human aorta - influence of fluid-structure interaction. *International Journal of Applied Mechanics*, 4(4):759–778, July 2011.

[34] M. Li. Implement interFoam as a fluid solver in the FSI package. Technical tutorial 1, Chalmers University of Technology, Chalmersplatsen, Sweden, October 2017.

[35] C. Liu, D. Chen, and D. Bluemike et al. Evolution of aortic wall thickness and stiffness with atherosclerosis: Long-term follow up from the multi-ethnic study of atherosclerosis (mesa). *Hypertension*, 65(5):1015–1019, May 2016.

[36] X. Liu, Y. Fan, X. Deng, and F. Zhan. Effects of non-newtonian and pulsatile blood flow on mass transport in the human aorta. *Journal of Biomechanics*, 44(6):1123–1131, April 2011.

[37] K. Lizuka, T. Nishinaka, and D. Akiyama et al. The angle of the outflow graft to the aorta can affect recirculation due to aortic insufficiency under left ventricular assist device support. *Journal of Artificial Organs*, 21(1):399–404, July 2018.

[38] J. Long, A. Undar, KB. Manning, and S. Deutsch. Viscoelasticity of pediatric blood and its implications for the testing of a pulsatile pediatric blood pump. *American Society for Artificial Internal Organs*, 51(5):563–566, October 2005.

[39] M. Lui, S. Martino, M. Salerno, and M. Quadrio. On the turbulence modeling of blood flow in a stenotic vessel. *Journal of Biomedical Engineering*, 39(6):745–751, July 2012.

[40] M. Maivè, A. Garcia, J. Ohayon, and M. Martinez. Unsteady blood flow and mass transfer of a human left coronary artery bifurcation: Fsi vs. cfd. *International Communications in Heat and Mass Transfer*, pages –, June 2019.

[41] P. Marques, M. Oliveria, A. Franca, and M. Pinotti. Modeling and simulation of pulsatile blood flow with a physiologic wave pattern. *Artificial Organs*, 27(5):478–485, May 2003.

[42] P. Moin and K. Mahesh. Direct numerical simulation: A tool in turbulence research. *Annual Review of Fluid Mechanics*, 30(1):539–578, January 1998.

[43] M. Nicosia, J. Kasalko, R. Cochran, D. Einsteina, and K. Kunzelman. Biaxial mechanical properties of porcine ascending aortic wall tissue. *The Journal of Heart Valve Disease*, 11(5):686–687, August 2002.

[44] M. Olufsen, S. Peskin, W. Kim, E. Pedersen, A. Nadim, and J. Larsen. Numerical simulation and experimental validation of blood flow in arteries with structured-tree outflow conditions. *Annals of Biomedical Engineering*, 28(11):1281–1299, November 2000.

[45] J. Pedlosky. *Geophysical fluid dynamics*. Springer, New York, NY, 1987.

[46] S. Priya, R. Thomas, P. Nagpal, A. Sharma, and M. Steigner. Cogenital anomalies of the aortic arch. *Cardiovascular Diagnostics and Therapy*, 8(1):S26–S44, April 2018.

[47] P. Rao. Coarctation of the aorta. *Current Cardiology Reports*, 7(1):425–434, November 2005.

[48] A. Razavi, E. Shirani, and M.R. Sadeghi. Numerical simulation of blood pulsatile flow in a stenosed carotid artery using different rheological models. *Journal of Biomechanics*, 44(11):2021–2030, July 2011.

[49] W. Riley, R. Barnes, G. Evans, and G. Burke. Ultrasound measurements of the elastic modulus of the common carotid artery: the aterosclerosis risk in communities (aric) study. *Stroke*, 23(1):952–956, July 1992.

[50] S. Rison, T. Locke, E. Rosenthal, and S.Gandhi. A man with hypertension and two murmurs. *BMJ*, 344(7845):e956, February 2012.

[51] K. Robinson, R. Scott, A. Hesek, E. Woodford, W. Amir, T. Planchon, K. Klick, and R. Akins. Reduced arterial elasticity due to surgical skeletonization is ameliorated by abluminal peg hydrogel. *Bioengineering & translational medicine*, 30(2):222–232, May 2017.

[52] S. Roux, H. Kuhn, H. Lengsfeld, and O. Morand. Effects of chronic aortic coarctation on atherosclerosis and arterial lipid accumulation in the watanabe hereditary hyperlipidemic (whhl) rabbit. *Atherosclerosis*, 93(1):123–132, March 1992.

[53] O. Salazar, J. Steinberger, W. Thomas, A. Rocchini, B. Carpenter, and J. Holler. Long-term follow-up of patients after coarctation of the aorta repair. *The American Journal of Cardiology*, 89(5):541–547, March 2002.

[54] S. Sherifova and G. Holzapfel. Biomechanics of aortic wall failure with a focus on dissection and anuerysm: A review. *Acta Biomaterialia*, 99(1):1–17, November 2019.

[55] X. Song, H. Wood, S. Day, and D. Olsen. Studies of turbulence models in a computational fluid dynamics model of a blood pump. *Artificial Organs*, 27(10):935–937, October 2003.

[56] E. Soudah, E. Onate, and M. Cervera. Computational fluid dynamics indicators to improve cardiovascular pathologies diagnosis. *Monograph CIMNE*, 2016.

[57] PD. Stein and Hn. Sabbah. Turbulent blood flow in the ascending aorta of humans with normal and diseased aortic valves. *Circulation Research*, 39(1):58–65, July 1976.

[58] A. Tran, B. Burkhardt, and A. Tandon et al. Pediatric heterozygous familial hypercholesterolemia patients have locally increased aortic pulse wave velocity and wall thickness at the aortic root. *International Journal of Cardiovascular Imaging*, 35(10):1903–1911, October 2019.

[59] S. Verma and S. Siu. Aortic dilatation in patients with bisucspid aortic valve. *The New England journal of medicine*, 370(1):1920–1929, August 2014.

[60] H. Versteed and W. Malalasekera. *An Introduction to Computational Fluid Dynamics, the Finite Volume Method*. Prentice Hall, Upper Saddle River, NJ, 2007.

[61] I. Vignon-Clementel, C. Figueroa, K. Jansen, and C. Taylor. Outflow boundary conditions for three-dimensional finite element modelling of blood flow and pressure in arteries. *Computer Methods in Applied Mechanics and Engineering*, 195(29-32):3776–3796, June 2006.

[62] I. Vignon-Clementel, C. Figueroa, K. Jansen, and C. Taylor. Outflow boundary conditions for 3d simulations of non-periodic blood flow and pressure fields in deformable arteries. *Computer Methods in Biomechanics and Biomedical Engineering*, 13(5):625–640, February 2010.

[63] F. Vita, M. Tullio, and R. Verzicco. Numerical simulation of the non-newtonian blood flow through a mechanical aortic valve. *Theoretical and Computational Fluid Dynamics*, 30(1-2):129–138, November 2015.

[64] K. Vitanova, J. Cleuziou, J. Pabst, M. Burri, A. Eicken, and R. Lange. Recoarctation after norwood 1 procedure for hypoplastic left heart syndrome: Impact of patch material. *Ann Thorac Surg*, 103(2):617–621, February 2017.

[65] W. Wu, N. Aubry, M. Massoudi, J. Kim, and J. Antaki. A numerical study of blood flow using mixture theory. *International Journal of Engineering Science*, 76(1):56–72, March 2014.

[66] K. Yokawa, T. Tsukube, N. Yagi, M. Hoshino, Y. Nakashima, K. Nakagawa, and Y. Okita. Quantitative and dynamic measurements of aortic wall of acute type-a aortic dissection with x-ray phase-contrast tomography. *Arterioscelerosis, Thrombosis, and Vascular Biology*, 37(1):A490, August 2017.

[67] V. Zanardo, S. Visentin, and D. Trevisanuto et al. Fetal aortic wall thicness: a marker of hypertension in iugr children. *Hypertension Research*, 103(2):617–621, February 2017.

[68] J. Zhang, P. Zhang, K. Fraser, B. Griffith, and Z. Wu. Comparison of fluid dynamic numerical models for a clinical verntricular assisst device and experimental validation. *Artificial Organ*, 37(119):380–389, August 2013.